

THE UNIVERSITY OF CHICAGO

DEVELOPING RAPID MIXING TECHNOLOGIES FOR TIME-RESOLVED INFRARED  
SPECTROSCOPY

A DISSERTATION SUBMITTED TO  
THE FACULTY OF THE DIVISION OF THE PHYSICAL SCIENCES  
IN CANDIDACY FOR THE DEGREE OF  
DOCTOR OF PHILOSOPHY

DEPARTMENT OF CHEMISTRY

BY

RAM CHANDRA ITANI

CHICAGO, ILLINOIS

DECEMBER 2023

Copyright © 2023 by Ram Chandra Itani

All Rights Reserved



# TABLE OF CONTENTS

LIST OF FIGURES . . . . .	5
LIST OF TABLES . . . . .	14
ACKNOWLEDGMENTS . . . . .	15
ABSTRACT . . . . .	19
1 INTRODUCTION . . . . .	1
1.1 Advancements in understanding chemical kinetics: From mathematical models to spectroscopy and beyond . . . . .	1
1.2 Rapid mixing for studying bimolecular reactions and biophysical processes . . . . .	2
1.2.1 Continuous-Flow method . . . . .	3
1.2.2 Stopped-Flow method . . . . .	4
1.3 Microfluidics: Revolutionizing rapid mixing technologies . . . . .	5
1.3.1 Combining microfluidics with IR spectroscopy . . . . .	9
1.4 Thesis Outline . . . . .	12
2 MICROFLUIDIC THEORY . . . . .	14
2.1 Overview . . . . .	14
2.2 Viscosity and its role in fluid flow in the microchannel . . . . .	15
2.2.1 Momentum Transport . . . . .	17
2.2.2 Reynolds and Peclet Number . . . . .	18
2.2.3 Pressure and fluid resistance in microchannel . . . . .	20
2.3 Governing equations in fluid dynamics . . . . .	22
2.3.1 Continuity Equation . . . . .	23
2.3.2 The Navier-Stokes equation - Momentum conservation . . . . .	24
2.4 Analytical solution to pressure driven flow . . . . .	25
2.4.1 Hagen-Poiseuille flow . . . . .	25
2.4.2 Flow in a rectangular micro channel . . . . .	28
2.5 Physics of mixing . . . . .	31
2.5.1 Flow from a narrow to wide flared channel . . . . .	35
2.6 Conclusion and Outlook . . . . .	37
2.7 Appendix . . . . .	38
2.7.1 Ohm's and Kirchhoff's law analogs in pressure driven flow . . . . .	38
2.7.2 Terminology used to describe flow patterns in microfluidics literature . . . . .	39
3 FABRICATION AND CHARACTERIZATION OF IR COMPATIBLE MICROFLUIDIC MIXER . . . . .	41
3.1 Overview . . . . .	41
3.2 Microfluidic mixer . . . . .	41
3.3 Fabrication of IR compatible microfluidic mixer . . . . .	42

3.3.1	Mixer design . . . . .	43
3.3.2	Observation channel design . . . . .	47
3.4	Photo-Lithography . . . . .	54
3.5	Detailed fabrication steps for AZ40XT photoresist . . . . .	55
3.6	Bonding . . . . .	59
3.6.1	Anatomy of the hydraulic heat press . . . . .	59
3.6.2	Example I: Excellent bonding . . . . .	64
3.6.3	Example II: Bonding failures . . . . .	64
3.7	Micro channel geometry characterization . . . . .	67
3.7.1	Before bonding . . . . .	67
3.7.2	After bonding . . . . .	68
3.7.3	Lithography for alternative photo resists with enhanced chemical compatibility . . . . .	70
3.8	Reusing calcium fluoride windows after lithography . . . . .	71
3.8.1	Removing AZ40-XT and AZ 1518 photo resist . . . . .	71
3.8.2	Removing SU8 3050 . . . . .	72
4	FLOW SETUP AND CHARACTERIZATION OF MIXING . . . . .	74
4.1	Overview . . . . .	74
4.2	Flow cell for spectroscopy . . . . .	74
4.2.1	Anatomy of flow cell . . . . .	75
4.3	Characterization of mixing . . . . .	82
4.3.1	Mixing of colored solution . . . . .	82
4.3.2	Mixing of rhodamine 6G with water . . . . .	84
4.3.3	Quenching of fluorescein fluorescence . . . . .	86
4.3.4	Mixing in 3-Turn mixer . . . . .	87
4.3.5	IR spectroscopy to demonstrate mixing . . . . .	88
4.4	Improving flowcell assembly . . . . .	89
5	TIME-RESOLVED IR SPECTROSCOPY IN AQUEOUS SOLUTION . . . . .	94
5.1	Overview . . . . .	94
5.2	Data acquisition . . . . .	94
5.3	Optimization of instrument parameters . . . . .	97
5.4	Data processing . . . . .	98
5.4.1	Background subtraction . . . . .	98
5.4.2	Baseline correction . . . . .	99
5.4.3	Comparison of baseline correction methods . . . . .	102
5.5	Appendix . . . . .	103
5.5.1	Data reproducibility . . . . .	103
6	DEMONSTRATING ABILITY TO PROBE MILLISECOND AND MICROSECOND KINETICS . . . . .	105
6.1	Overview . . . . .	105
6.2	Ferricyanide reduction by ascorbic acid . . . . .	106

6.2.1	Reaction mechanism . . . . .	108
6.3	Rate law and kinetic model . . . . .	110
6.3.1	pH dependence of the reduction rate . . . . .	113
6.4	Time-Resolved FTIR kinetics of the reduction reaction . . . . .	114
6.4.1	Fitting and normalization scheme . . . . .	117
6.4.2	Validation of the relaxation rates . . . . .	120
6.5	Demonstration of microsecond kinetic process using a laser based IR source .	121
6.5.1	Raw kinetic data with laser IR source . . . . .	123
6.5.2	Fitting and normalizing the kinetic data . . . . .	123
6.5.3	Reaction mechanism at high pH . . . . .	126
6.6	Discussion and Outlook . . . . .	129
6.7	Appendix . . . . .	132
6.7.1	Sample preparation . . . . .	132
	REFERENCES . . . . .	133

## LIST OF FIGURES

1.1	Rapid mixing strategies for time-resolved spectroscopy. (a) Continuous flow: This configuration employs syringes A and B connected to a drive motor, controlling fluid flow through a mixer. The resulting mixture is then observed at a distance from the mixer using optical probe. A continuous flow method allows for time delays to be mapped onto distance along an observation channel, with the time resolution and observable time window defined by the flow rate, the size of the IR observation beam and the dimensions of the channel. (b) Stopped-flow: Flow halts upon entering the observation cell through a stop syringe. The examination of the static point within the cell facilitates the tracking of reaction progress. The determination of time resolution and time delay hinges on several factors including mixing and transfer ('dead') times, as well as the scan rate of the spectroscopic probe. . . . .	3
2.1	Illustration of shear flow of fluid between two planes. The application of shear force causes the movement of one plane with respect to the other, and the internal friction force $F_x$ , between the fluid sets up a velocity gradient along $y$ . The relationship between this opposing force per unit surface area and viscosity is expressed by Equation 2.1. . . . .	16
2.2	Laminar and turbulent flow. In laminar flow, the velocity field remains constant and exhibits minimal fluctuations or irregularities. The magnitude and direction of the velocity vector at any given point in the flow do not change significantly over time. The streamline (blue lines) are imaginary lines that represent the instantaneous direction of fluid flow and provide visualizations of the flow pattern and are constructed in such a way that at any given point, the tangent to the streamline indicates the direction of the fluid velocity vector. In other words, streamlines provide a snapshot of the path that a tiny fluid particle would follow as it moves through the medium. For laminar flow, the streamline remain smooth and do not intersect, resulting in well-defined and predictable flow patterns. Turbulent flows imply that the laminar flow is unstable and not observed. Turbulent flows are defined by their unsteady and rotational nature, with fluid particles exhibiting circular or rotational patterns around a central axis. (Freely adapted from nuclear engineering [1]) . . . . .	19
2.3	(a) Circular channel with radius, $r = R$ and origin at the center, top view (b) The velocity distribution in the circular channel shown in a cutaway view. At the center of the channel, the velocity is maximum, and as we move towards the wall of the channel, the velocity decreases. This parabolic velocity profile is a characteristic feature of pressure-driven flow in circular channel. . . . .	25
2.4	Evaluation of axial velocity distribution in a rectangular microchannel. (a) Visualization of a rectangular microchannel in 3D and side view. (b) Plot of axial velocity distribution along the center-plane (colored for clarity). The velocity profile is parabolic, and it becomes increasingly flatter in the center as the width-to-height ratio, $w/h$ , exceeds 2. . . . .	29

2.5	(a)	Physics of fluid flowing through a turn. The fluid, flowing with a velocity of $U_0$ and passing through a channel of width $w$ , navigates a turn that takes a time $\tau_0 = \frac{w}{U_0}$ . The fluid element rounding the corner experiences a loss of momentum density denoted as $\rho U_0$ in the y direction giving rise to the centrifugal force density (red arrow), approximated as $f_i \sim \frac{\rho U_0}{\tau_0} = \frac{\rho U_0^2}{w}$ . A comparison can be made between this inertial force and the viscous force densities, denoted as $f_v \sim \frac{\mu U_0}{L_0^2}$ , which emerge within the flow as a result of the internal friction of the fluid. (b) Flow of a dye and quencher at low $Re$ and high $Re$ regimes: At low $Re$ , the flow is laminar, and mixing is purely diffusive, difficult to observe despite passing through turns. As $Re$ increases, fluid elements stretch and fold, leading to chaotic trajectories, enhancing mixing further along the turn. . . . .	32
2.6	(a)	Schematic of serpentine zigzag mixer design by Li <i>et al.</i> The channel geometry is designed such that the flow through zigzag stretch and fold the solution primary flow to generate narrow striations, which exponentially increase the interfacial area between the solutions and cause rapid mixing within its short channel length. Validation of the mixing efficiency: (b) Computational fluid dynamics simulation showcasing the mixing process. (c) Experimental mixing of sulforhodamine B (red) and fluorescein (green) within the zigzag mixer, achieved at a flow rate of 10 $\mu\text{L/s}$ . Adapted from Ref [2] (Copyright 2014, with permission from Analytical Chemistry) and Ref [3] (Copyright 2012, with permission from Talanta). . . . .	33
2.7	Staggered herringbone mixer (SHM).	Schematic diagram of one-and-a-half cycles of the SHM. A mixing cycle is composed of two sequential regions of ridges; the direction of asymmetry of the herringbones switches with respect to the centerline of the channel from one region to the next. The streamlines of the flow in the cross section are shown schematically above the channel. The angle, $\Delta\Phi_m$ , is the average angular displacement of a volume of fluid along an outer streamline over one half cycle in the flow generated by the wide arms of the herringbones. The fraction of the width of the channel occupied by the wide arms of the herringbones is $p$ . The horizontal positions of the centers of rotation, the upwellings, and the downwellings of the cellular flows are indicated by $c$ , $u$ , and $d$ , respectively. (A,B,C) Cross sections of the dye distribution in a microfluidic channel designed to create staggered, time-dependent whorls or twist maps. These whorls play a role in shortening the length scales over which diffusion must act. Adapted from Ref [4] (Copyright 2002, with permission from Science). . . . .	34
2.8	Flow through a flared channel wall.	The force experienced by the flaring wall is given by $F_{\text{wall}} = p_1(S_1 - S_2) + \frac{1}{2}\rho u_1^2 S_1 \left(2 - \frac{S_2}{S_1} - \frac{S_1}{S_2}\right)$ . . . . .	35

3.1	Design details on a 40 mm $\varnothing$ CaF <sub>2</sub> window. (a) A 25 mm $\varnothing$ photo resist film of uniform thickness ( 30 $\mu$ m) coats the window, as depicted by red circle, onto which the channels are etched. Fluid is introduced through two inlet ports located at the top of the device, flows through the mixing region, and exits via an outlet port at the bottom. (b) Design of mixing region. A 350 $\mu$ m diameter sampling region is incorporated in the inlet channels that transmits the entire focused IR beam and is used to acquire reference IR spectra of the inlet solutions and an air background. Within the mixer, the two inlets merge into a 20 $\mu$ m channel at the beginning of the mixing region and flare out after the mixing region into a 350 $\mu$ m wide observation channel to accommodate measurement with IR beam. . . . .	43
3.2	Comparison of traditional masked lithography (a) and modern maskless lithography (b), adapted from Ref [5] (Copyright 2016, with permission from SPIE digital library). In traditional photolithography, a UV lamp exposes the photoresist through a mask pattern, enabling pattern transfer onto the substrate. While traditional lithography offers well-established processes and large-scale production, it is limited by the reliance on physical masks. These masks require separate fabrication and precise alignment during the lithographic process, lowering resolution, adding complexity and increasing costs. In contrast, maskless photolithography utilizes digital light projection (DLP) with suitable laser systems to directly expose the photoresist, eliminating the need for physical masks. This approach improves resolution by two orders of magnitude compared to conventional method. Other advantage is its flexibility, as design modifications can be quickly implemented by updating the CAD layout. This enables efficient prototyping and rapid iteration of designs, making it ideal for research and development purposes. . . . .	45
3.3	Illustration of the inchworm, serpentine and 3-turn mixer designs. . . . .	46
3.4	Visualization of the observation channel design aimed at assessing and enhancing time resolution. The time resolution ( $\Delta\tau_0$ ) of the measurement encompasses the mixing time ( $\tau_{\text{mix}}$ ), the time to reach the initial observation point ( $\tau_{\text{obs}}$ ), and the temporal variation of the IR probe ( $\tau_{\text{beam}}$ ). The time delay ( $\Delta\tau$ ) corresponds to the interval between consecutive measurements. . . . .	49
3.5	Microscope Point Spread Function (PSF) of a glow bar source from FTIR in transmission mode, captured at the focus plane. Contour plots were generated by scanning a 5 $\mu$ m pinhole across the focus plane's raw data (a) and subsequently fitted with a Gaussian fit (b) to determine the FWHM. The observed asymmetry in the beam emphasizes that the beam collimation of the glow bar source is not optimally aligned. . . . .	50
3.6	Illustration of observation channel designs within the measurement aperture, represented by a green dashed circle. The designs include a linear channel (7 mm long path) with a corresponding time window of 6 ms, an alternating channel (50 mm long path) with a time window of 45 ms, and a spiral channel (40 mm long path) with a time window of 36 ms at a flow rate of 0.7 mL/min. . . . .	53

3.7	Fabrication steps for AZ40XT photoresist. (a) The CaF <sub>2</sub> substrates are placed inside a flat-bottom glass container containing organic solvents and cleaned using ultrasonic bath. (b) The residual solvent is removed by baking in a vacuum at 110 ° C. (c) Spin coating to achieve a uniform photoresist layer on the substrate. (d) The residual solvent in the resist is removed by heating on a hot plate in a process known as soft bake. (e) The photoresist is exposed to a 375 nm laser to pattern the micro channel design. (f) Post exposure baked is performed to complete the photoreaction and make the resist developable by heating in a hot plate. (g) The exposed resist is etched by dipping in a MIF 300 developer solution. (h) Microchannel is closed by bonding with drilled CaF <sub>2</sub> window. . . . .	56
3.8	Modified dolytek press with enhancements for bonding reproducibility. . . . .	61
3.9	Illustration of excellent bonding process. (a) Pair of 1 mm thick CaF <sub>2</sub> assembly after the first sealing step, demonstrating complete bonding at the lower end. The presence of interference fringes (red circle) on the top side, caused by the reflection of light between the surface of the photoresist film and the drilled CaF <sub>2</sub> window, confirms that the surfaces are not fully bonded. (b) Image after the second sealing step, showcasing complete bonding with no trapped air bubbles. (c) Microscope image showcasing the serpentine mixer before the bonding process. (d) The microscope image taken after bonding reveals the intact and undamaged state of the mixer, providing positive confirmation that the bonding process did not result in any damage to the mixer. . . . .	64
3.10	Illustration of bonding failures. In (a), two CaF <sub>2</sub> sandwiches are shown, and the presence of interference fringes on both, as indicated by the red circle, suggests incomplete bonding between the surfaces. One CaF <sub>2</sub> sandwich had cracks on the drilled window, as indicated by red square, suggesting excessive stress during the bonding. (b) Microscope image revealing complete bonding on one inlet (top right) and incomplete bonding elsewhere, with more prominent fringes visible. (c) Microscope image demonstrating complete bonding, but with mixer deformation.	65
3.11	Illustrating the height characterization process using 3D optical profilometry.(a) Map image of CaF <sub>2</sub> window after photolithography with AZ 40XT photoresist, individual pixel captured at 5X magnification and stitched together. The pixelation is a result of artifacts incorporated in the stitching algorithm, stemming from auto-focusing. Noteworthy features include a microchannel, a bubble within the photoresist film (highlighted by the red circle), and areas of underdeveloped photoresist (highlighted by the red square). (b) The 3D height map of the serpentine mixer, captured at 20X magnification. The width of the channel walls in the mixer is 20.0 ± 0.2 μm, which is within 1% of the CAD design. The channel depth is 34 ± 0.5 μm and the film surface variation is 100 nm, indicating highly uniform deposition of the photoresist film. The almost 90 deg steep channel walls showcase exceptional photolithography. . . . .	68

3.12	(a) Comparison of depth profile before and after bonding using laser confocal profilometry on the same microwell, with corresponding images shown at the bottom. The compression due to bonding is less than 5%. (b) FTIR spectra of water bend libration mode at known spacer thicknesses. The blue, red, and black lines represent spacer thicknesses of 100 $\mu\text{m}$ , 50 $\mu\text{m}$ , and 25 $\mu\text{m}$ , respectively, and the dashed lines represent spectra collected in microchannel devices. (c) The dashed black line represents the calibration curve constructed from taking absorption at $1920\text{ cm}^{-1}$ from known spacer thicknesses, which was used to derive the microchannel depth, depicted by colored circles. . . . .	69
4.1	Design of the 3D printed compression cell. (a) Top compression flange, (b) 1 mm thick, 40 mm $\varnothing$ CaF <sub>2</sub> window onto which the mixer is fabricated, (c) 33 $\mu\text{m}$ thick AZ 40XT photoresist film (d) 1 mm thick, 35 mm $\varnothing$ CaF <sub>2</sub> window with drilled inlet and outlet ports, (e) Bottom flange containing internal tubing connections, and 10 mm $\varnothing$ aperture for transmission measurement. . . . .	75
4.2	Fully assembled flow cell with detailed view of the PEEK connection in the inset	77
4.3	Optimized procedure for sample loading. (Left) Transfer of filtered samples into the stainless steel syringe. (Center) Correct application of Teflon tape and hand-tight attachment of the Swagelok fitting to the syringe. (Right) Secure connection of the loaded syringe to the syringe pump. . . . .	79
4.4	Experimental setup involving integration of flowcell into Bruker Hyperion IR microscope. . . . .	82
4.5	Qualitative assessment of food color mixing in the microchannel. The images demonstrate the mixing process at different flow rates, highlighting the transition from laminar to turbulent increased flow with increased mixing homogeneity with increasing flow rates. . . . .	84
4.6	Fluorescence images of the observation channel following mixing of 50 $\mu\text{M}$ rhodamine 6G solution and water in (a) serpentine and (c) inchworm mixer at a flowrate 100, 300, 500/600 and 700 $\mu\text{L}/\text{min}$ . Fluorescence distribution across the channel 150 $\mu\text{m}$ from the exit of the mixer, dashed magenta line, is shown on (b) and (d) suggest homogeneous mixing at flowrate $>600\text{ }\mu\text{L}/\text{min}$ . (e) Fluorescence images of the observation channel following the quenching reaction of 1 $\mu\text{M}$ fluorescein by 0.5 M potassium iodide in an “inchworm” mixer. (f) Fluorescence distribution suggests 70 % drop in fluorescein fluorescence upon complete mixing.	85
4.7	(a)Fluorescence images of the observation channel in 3-turn mixer following quenching reaction 1, 100, 300 and 600 $\mu\text{L}/\text{min}$ . (b) Fluorescence distribution across the channel 30 $\mu\text{m}$ from the exit of the mixer, dashed magenta line, suggest homogeneous mixing at flowrate $>300\text{ }\mu\text{L}/\text{min}$ . . . . .	87



4.8	Peak normalized FTIR spectra at a flowrate 100, 300, 600 $\mu\text{L}/\text{min}$ of AMP pH jump experiment monitored at the exit of the “serpentine” mixer. The blue and green dot in the inset shows the measurement location and the relative size of the IR beam and the steady state spectra and initial and final pH is shown in dashed magenta and red lines, respectively. The rise in $1624\text{ cm}^{-1}$ and drop in $1666\text{ cm}^{-1}$ mode with increasing flowrate, which become uniform across both measurements at $300\text{ }\mu\text{L}/\text{min}$ suggests homogeneous mixing, consistent with fluorescence imaging.	89
4.9	Illustration of common failures observed during mixing experiments. (a) Microscope image depicting dust particles lodged in a serpentine mixer, leading to blockage. The clogged mixer can cause a buildup of high pressure, potentially damaging the mixer wall. Additionally, this can result in catastrophic failure of the flow cell, as demonstrated by cracks in the $\text{CaF}_2$ sandwich assembly shown in (b).	90
4.10	Design of the machined brass flow cell. (a) Nanoport assemblies for internal tubing connection (N-333, IDEX, USA), (b) Brass flange with opening for nanoport, and through holes for 8-32 screws (c) 1 mm thick, 25 mm $\varnothing$ drilled $\text{CaF}_2$ window with 1.5 mm $\varnothing$ two holes 19 mm apart, (d) Mixer - either photoresist film or 3M 30 $\mu\text{m}$ double sided sticky tape, (e) 1 mm thick, 25 mm $\varnothing$ $\text{CaF}_2$ window (f) Bottom brass flange with tapped holes for 8-32 screws.	93
5.1	Beam path of the Hyperion 2000 infrared microscope in transmission mode. The IR beam enters the microscope from the bottom left, traverses several gold and parabolic mirrors for alignment, and aligns in parallel with visible LED illumination. It then proceeds through the 15X Cassegrain condenser, focusing onto the sample plane. The objective collects the light, which can be visualized using a binocular or the colored camera. The light is subsequently detected by either of the IR detectors. Motor 1 and 2 facilitate switching between three measurement modes: visible, IR, or IR/visible mode, achieved by selectively configuring appropriate optics. For instance, when using the IR/visible measurement mode, the gold mirror is replaced with a dichroic mirror that reflects IR light while allowing visible light to pass through. This enables simultaneous mapping and measurement of the sample.	96
5.2	Example of solvent background correction. (a) FTIR spectra collected at various time delays in a typical mixing experiment (colored line), and solvent solution collected at one of the reference channels (black dashed). The smoothly sloping baseline in the spectra is dominated by the bend-libration combination band of $\text{H}_2\text{O}$ and the CN vibration of ferri-ferrocyanide sits on top of the solvent at $2115\text{ cm}^{-1}$ and $2037\text{ cm}^{-1}$ , respectively. (b) Spectra after subtracting the spectra of the background solvent solution.	99

5.3	Illustration of a simple baseline correction using a linear offset. (a) The background subtracted transient FTIR absorption spectra between 2000-2150 $\text{cm}^{-1}$ as a function of mixing time delays from 0.1 ms (blue) to 35 ms (red). Residual baseline offsets, which we attribute to clipping of the beam by the flowcell bottom flange is evident at long delays. (b) Transient spectra after correcting for baseline shifts by subtracting/adding a linear offsets (black arrows) to match the change in absorbance at a frequency where there is no molecular absorption (2085 $\text{cm}^{-1}$ for this case). . . . .	101
5.4	Illustration of baseline correction using DWT. (a) FTIR spectra collected at three different time points in a reduction of ferricyanide by ascorbic acid. The DWT method was used to construct an offset background (dashed black). (b) Spectra after DWT baseline correction, showing both the sloping and offset corrected effectively. . . . .	102
5.5	Comparison of baseline correction methods for the ferrocyanide reduction reaction. (a) Raw transient spectra showing incremental time delays (color gradient from blue to red). (b) Linear offset correction, which aligns the data at 2075 $\text{cm}^{-1}$ but does not correct the sloping baseline. (c) Discrete Wavelet Transform (DWT) correction, effectively correcting the sloping baseline with minimal change in absorbance. (d) Rubberband correction, resulting in over correction and reduction in $\Delta OD$ . . . . .	103
5.6	Illustration of data reproducibility. (a) Solvent-background subtracted and baseline-corrected spectra for the mixing of 0.1 M ascorbic acid with 25 mM potassium ferricyanide prepared in 0.1 M, pH 8 sodium phosphate buffer. The three data sets were obtained using the same micromixer and measurement parameters. In addition to the ferro and ferricyanide peaks, data 2 and 3 exhibit a peak at 2075 $\text{cm}^{-1}$ , which can be attributed to Prussian blue formation from residual ferrocyanide reacting with the fresh ferricyanide solution. (b) The corresponding kinetics show consistent growth of the ferrocyanide mode at 2037 $\text{cm}^{-1}$ , confirming the reproducibility of the kinetic data. . . . .	104
6.1	Equilibrium FTIR absorption spectra of 25 mM ferricyanide (red) and ferrocyanide (blue). The ferricyanide mode is centered at 2115 $\text{cm}^{-1}$ with a full width at half maximum (FWHM) bandwidth of 9 $\text{cm}^{-1}$ . The ferrocyanide mode is centered at 2037 $\text{cm}^{-1}$ , with a FWHM bandwidth of 17 $\text{cm}^{-1}$ . . . . .	107
6.2	Potassium ferricyanide reduction kinetics. (a) Raw transient FTIR absorption spectra in the CN stretching region at time delays from 0.2 ms (blue) to 20 ms (red) for pH 6.6 with reference spectra at the inlets of ferricyanide (dashed) and ascorbic acids (dash-dotted). (b) The same spectra following background subtraction and baseline correction. The colorbar indicates the temporal progression of the reaction. . . . .	114

6.3	Time-dependent peak absorbance for the ferrocyanide (a) and ferricyanide (b) vibrations for pH 5.5, 7.9, 8.3, 9.4. The variations in the measured absorbance can be attributed to sample preparation, and path length variations of the microchannel. The ferricyanide mode for pH 5.5 is excluded from the plot due to high noise level in the data. . . . .	116
6.4	Example of fitting and normalization schemes used to extract kinetic parameters. (a) Time-dependent peak absorbance for ferricyanide (red) and ferrocyanide (blue) vibrations at pH 7.7, fitted with exponential functions to extract baselines ( $A_\infty$ , $a_\infty$ ) and time zero absorbance values ( $A_0$ , $a_0$ ). (b) Normalized time-dependent peak absorbance using time zero and baseline values. . . . .	118
6.5	Time-dependent peak absorbance for the ferrocyanide (a) and ferricyanide (b) vibrations for pH 5.5, 7.9, 8.3, 9.4. The kinetic traces of ferrocyanide mode at pH 9.4 have already grown within the first ten measurement points indicating that the reaction rate is too fast and at the limit of the current time resolution of the device. . . . .	119
6.6	(a) Experimentally determined relaxation rate constants (green circle) plotted against pH and fitted to the Equation 6.17 (blue line) for validation of the experimental results. The dashed red lines represent the upper and lower bounds of the measurable rate constant. (b) Transient FTIR spectra captured during the reduction reaction at pH 4. The experiment was halted due to the formation of a precipitate, the prussian blue complex, marked by an absorption peak at $2072\text{ cm}^{-1}$ . (c) Transient FTIR spectra captured during the reduction reaction at pH 9. The reduction reaction is complete within the first few measurement points, illustrating the measurement's $\log(k)$ limitation above 4.5. . . . .	120
6.7	IR probe beam characterization. (a) Grayscale image of the IR intensity from a pinhole scan in the focal plane ( $Z = 0$ ). (b-c) The IR intensities (black circles) from a $5\text{ }\mu\text{m}$ pinhole scan at the focal plane with Gaussian fit (red). The FWHM along the X and Y directions are $13\text{ }\mu\text{m}$ and $12\text{ }\mu\text{m}$ , respectively. . . . .	122
6.8	Potassium ferricyanide reduction kinetics probed with laser-based IR spectroscopy employing a 3-turn mixer. (a) IR intensities following the mixing of 0.1 M ascorbic acid with 25 mM ferricyanide within a 0.5 M potassium phosphate buffer at pH 8.5. The color transition from blue ( $50\text{ }\mu\text{s}$ ) to red ( $4\text{ ms}$ ) on the colormap corresponds to early to late time points. The IR source, centered at $2038\text{ cm}^{-1}$ , with FWHM of $150\text{ cm}^{-1}$ , facilitates simultaneous probing of both ferricyanide at $2115\text{ cm}^{-1}$ and the ferrocyanide mode at $2037\text{ cm}^{-1}$ . (b) IR intensities of the solvent (0.5 M buffer) collected at the corresponding sample measurement points. (c) Linear IR absorption spectra from direct difference of the sample and solvent intensities. The growth of the ferrocyanide mode is evident, while the decay of the ferricyanide exhibits relatively more noise in comparison. (d) IR absorption spectra post baseline correction using a discrete wavelet method. . . . .	124

6.9	Fitting and normalization schemes.(a) Time dependent peak absorbance for ferricyanide mode (red squares) and ferrocyanide (blue circles), fitted with exponential functions to extract the baselines ( $A_\infty$ , $a_\infty$ ) and time zero absorbance values ( $A_0$ , $a_0$ ). (b) Application of normalization procedures using baseline and initial values, following the methodologies outlined in equations 6.21 and 6.20, along with corresponding fitting outcomes. The fitting performance for ferricyanide is somewhat compromised due to the presence of measurement noise. . . . .	125
6.10	(a) Normalized time-dependent peak absorbance for ferrocyanide vibrations for pH 8.5, 11.7 and 12.3 , accompanied by fitted exponential curves. The fitting and normalization methodologies are detailed in section 6.4.1.(b) pH-dependent rate constants measured experimentally using both glowbar source (green circles) and laser (red square), juxtaposed with the kinetic model derived from Equation 6.17. The dashed lines represent the limit on the fastest rate constants measurable with each method. . . . .	126
6.11	Normalized time-dependent peak absorbance for ferrocyanide vibrations for pH 12.3 fitted to a fast (red) and slow (blue) bi-exponential curves. The goodness of the fit is better compared to the single exponential. . . . .	127
6.12	(a) Fluorescence images capturing the observation channel after the quenching reaction of 1 $\mu\text{m}$ fluorescein by 0.5M potassium iodide within an inchworm mixer. (b) A fluorescence intensity plot as a function of distance from the mixer exit, recorded at three distinct flow rates. The gradual incline is a result of non-uniform excitation caused by a halogen lamp. The data indicates that, at a flow rate of 500 $\mu\text{L}/\text{min}$ , a minimum distance of 0.7 mm from the mixer's exit is required for complete quenching. . . . .	130

## LIST OF TABLES

2.1	Comparison of terminologies used in electrical system and their fluid analogs. . .	39
2.2	Flow patterns in microchannel . . . . .	40
3.1	Summary of time resolution and related parameters for different mixer designs at a flow rate of $Q = 0.7$ mL/min and a channel height of $h = 30$ $\mu$ m. . . . .	51
3.2	Summary of lithography process for SU8 3050 and AZ1518 photoresist on 1 mm thick $\text{CaF}_2$ substrate. . . . .	70
5.1	Measurement parameters used for two instrument setups. . . . .	97
6.1	Summary of pH-dependent reduction kinetics. Measured pH of the initial input AA and ferricyanide solutions and the equilibrated final mixed solution are shown together with the pH dependent observed relaxation rate constants and relaxation times, ( $k_{obs}$ ) and relaxation times ( $\tau_{obs} = k_{obs}^{-1}$ ). . . . .	119

## ACKNOWLEDGMENTS

My journey through graduate school was challenging, and completing this thesis wouldn't have been possible without the support of remarkable individuals. Firstly, I express my deepest gratitude to my advisor, Andrei Tokmakoff, whose steadfast mentorship has shaped the past six years of my academic pursuit. Andrei played a pivotal role in steering a groundbreaking project in microfluidic mixing, going above and beyond to facilitate my understanding of the technology by allowing me opportunities for travel, training, and workshops. Amidst the challenges of fabricating the first prototype of the rapid mixer over three years, Andrei's calm demeanor and incredible patience were a constant antidote to frustrating days. His commitment to pushing boundaries, overcoming challenges, and nurturing the success of every group member has been commendable. I am sincerely thankful for his guidance not only in research but also in my transition to a career outside of academia.

Although my direct involvement was not in the existing group project, I benefited from the exceptional mentorship of several group members. Paul Sanstead, during my early days in the group, shared profound insights into T-jump experiments and instilled a deep commitment to scientific integrity. His compassionate mentoring became evident during my challenges in crafting a compelling research proposal for my candidacy exam. Sam Penwell played a crucial role in enhancing my technical skills, spanning from CAD design to microscopy. His approachability created a comfortable space for me to ask questions, significantly enriching my learning experience. Nick Lewis and Bogdan Dereka introduced me to 2D IR spectroscopy, offering valuable feedback to broaden the application of my project beyond rapid mixing. Yumin Lee significantly boosted my confidence in data analysis, providing a MATLAB script that I often use as a backbone for most of my data analysis. Special recognition goes to senior graduate members Chijui Feng, Memo Carpenter, and Ryan Menssen, who exemplified excellence and set a high standard for research within the group.

I had the pleasure of joining the group alongside Brennan Ashwood and John Hack. Brennan's work ethic and dedication to science were truly admirable, and he generously dedicated countless hours to help me understand nucleic acids and design mixing experiments. Outside the lab, our shared interests in sports, including playing squash and learning about tennis and baseball, added a dimension of camaraderie to our journey. John has been an outstanding colleague, providing invaluable assistance in grasping concepts in quantum mechanics and developing models in MATLAB. Their brilliance has been a tremendous asset to the group, and I am grateful to work alongside such talented individuals.

Collaborating with members of the FEIR lab, including Lukas Whaley-Mayda, Abhirup Guha, and Seung Yeon Lee, has been a privilege. I extend my heartfelt thanks to them for their pivotal roles in our collaborative efforts. Lukas warmly welcomed me into the lab, allowing me to conduct preliminary flow experiments using their custom microscope and providing access to LabVIEW, enhancing our capabilities with the Hyperion microscope. Abhirup and Seung demonstrated unwavering commitment by spending countless hours aligning the laser IR source into the Hyperion microscope and actively contributing to data collection. Abhirup's insightful questions and in-depth discussions were instrumental in developing an understanding of ferricyanide reduction by ascorbic acid. His special Indian chai and humorous anecdotes about cricket consistently brightened our collaborative journey.

I am also fortunate to have collaborated with two exceptional undergraduates, Max Moncada Cohen and Joshua Edwards. I extend my sincere gratitude to them for their invaluable contributions. Max's brilliance and work ethic significantly advanced the microfluidic project. His dedication and countless hours in the cleanroom were crucial in perfecting our microfabrication techniques. Additionally, his coding skills brought innovative ideas to data collection, enhancing the depth and quality of the research. Beyond the lab, Max played a crucial role in enhancing my personal life, introducing me to new hobbies like rock climbing

and bonfires. His generosity reached new heights when he invited me to spend Thanksgiving with his family, exemplifying his kindness and the depth of our friendship beyond the confines of the lab. As he embarks on his graduate school journey, I'm genuinely excited for his future pursuits, confident that he will continue to excel and positively impact those around him. Joshua diligently followed in Max's footsteps, broadening the microfluidic project's horizons through the integration of computational fluid dynamics simulations. His pivotal contributions were evident in the optimization of the mixer design. I express my gratitude to him for introducing valuable expertise to the project and for sharing a mutual passion for soccer. Other group members have also played a significant role in enriching my graduate school experience. I thank Melissa Bodine for introducing me to ice skating, making the bitterly cold Chicago winter enjoyable. I appreciate Sam Knight for inspiring the group to have lunch together and getting us out of the basement. I extend my thanks to Jakob Schauss, Liv Mumma, and Rowan Simonet for adding liveliness to the group by sharing chocolates and baking cookies.

In the broader context, my graduate school journey was made possible by the support and guidance of mentors at Earlham College. My acknowledgment begins with my undergraduate advisor, Corrine Deibel, whose exceptional mentorship opened doors to diverse research opportunities. In my freshman year, I had the privilege of working alongside Jeff West at Belden, whose mentorship not only instilled in me a profound curiosity but also imparted a structured approach to problem-solving. Outside of work, Jeff went the extra mile by introducing me to various aspects of American culture from football drafts to home brewing and the art of smoking the finest meat. I am truly grateful to him and his wife, Stella West, for their warmth and hospitality, welcoming me to share in the joy of Thanksgiving and Christmas celebrations. My gratitude extends to Greg Smith, who broadened my research horizons during my summer internship at the Indianapolis Museum of Art. Under his guidance, I delved into air quality monitoring and explored the intricate world of



identifying forgery using various analytical tools. During my tenure at Oak Ridge National Laboratory, I found an inspiring mentor in Carter Abney. His pivotal role in paving the way for my journey toward a PhD in chemistry cannot be overstated. Under Carter's guidance, I not only honed my research skills but also expanded my knowledge through hands-on experiments at unique facilities such as the Spallation Neutron Source and the Advanced Photon Source. His support extended beyond the laboratory as he assisted with my graduate school application process and played a pivotal role in steering me toward the University of Chicago.

Beyond the realm of professional endeavors, my gratitude extends to my family for their unconditional love, especially my parents and sister. In my time in graduate school, my friends added joy and I extend my deepest thanks to each of them. A special note of appreciation to Ananth Kamath, whose heartwarming gesture of a home-cooked meal became a source of solace during my toughest times. I express my gratitude to Shi En Kim for her kindness in caring for my feline companions and introducing me to new and enriching hobbies, such as cross-country skiing.

## **Funding**

I extend my sincere gratitude to the Department of Energy (DOE) and the National Science Foundation (NSF) for their generous support under DOE Grant No. DE-SC0014305 and Grant No. CHE-1856684, respectively.

## ABSTRACT

Fast microfluidic mixers are a valuable tool for studying non-equilibrium processes in solution at the microsecond time scale. But microfluidic mixers that are compatible with infrared (IR) spectroscopy have seen only limited development due to poor IR transparency of the conventional microfabrication material. This thesis describes the design, fabrication, and characterization of IR transparent  $\text{CaF}_2$ -based continuous flow mixers capable of measuring kinetics with micro-millisecond time resolution with IR spectroscopy, when integrated into an IR microscope. Our fabrication methodology leverages advancements in the nanofabrication and 3D-printing technologies. Microfluidic channels are directly fabricated on  $\text{CaF}_2$  substrates through photolithography and bonded to another drilled window via a heated press, effectively sealing the channel. This sandwiched  $\text{CaF}_2$  assembly is then enclosed within a 3D-printed flow cell, providing tubing connections for continuous flow applications. This continuous flow cell allows the mapping of time delays onto distances within an observation channel, with time resolution and the observable time window determined by factors such as flow rate, the size of the IR observation beam, and channel dimensions. Incorporating various "zig-zag" serpentine-based mixer design, we achieved homogeneous mixing at a flow rate of ranging from 0.4 to 0.7 mL/min. Kinetic measurements involving a model reduction reaction of ferricyanide by ascorbic acid demonstrate the capability to resolve relaxation processes occurring within one millisecond using a glowbar IR source and hundreds of microseconds using a laser IR source. This work opens doors for the investigation of various intriguing biomolecular systems, including DNA hybridization and protein folding, among others.

# CHAPTER 1

## INTRODUCTION

### 1.1 Advancements in understanding chemical kinetics: From mathematical models to spectroscopy and beyond

The study of chemical kinetics, encompassing the rates and mechanisms of chemical reactions, has been a foundational pursuit in chemistry research for over 150 years. Through the formulation of mathematical models, advancements in experimental techniques, and the utilization of computational methods, our understanding of reaction kinetics has greatly expanded. This knowledge has paved the way for remarkable progress in various fields, including pharmaceuticals, materials science, and many others.

In the late 19th century, significant advancements were made in the field of reaction kinetics. Swedish chemist Svante Arrhenius introduced the Arrhenius equation, a mathematical model that relates the temperature dependence of the reaction rate constant to the activation energy [6]. Simultaneously, German chemist Jacobus Henricus Van't Hoff made pioneering contributions to the field of chemical dynamics. His work focused on experimentally determining reaction rates, deriving rate laws and rate constants from these measurements [7].

During the early 20th century, English chemist Frederick Soddy and Hungarian chemist George de Hevesy revolutionized the field by introducing the use of radioactive tracers, enabling the tracking of radioactive atom movement and transforming the study of chemical reactions [8]. In the mid-20th century, English chemist Sir Cyril Norman Hinshelwood and Russian chemist Nikolay Semenov made notable contributions to our understanding of reaction mechanisms, which encompass the sequential steps occurring from reactants to products in a chemical reaction [9]. Hinshelwood focused on elucidating the intricacies of reaction kinetics, while Semenov's research centered around the concept of chain reactions,

where a small number of reactive intermediates generate a multitude of product molecules.

Advances in spectroscopy during the late 20th century enabled molecular-level investigations of reaction kinetics. Infrared spectroscopy, for example, facilitated the monitoring of molecular vibrations during chemical reactions, leading to a better understanding of reaction mechanisms and the identification of reactive intermediates. More recently, the advent of femtosecond laser technology has revolutionized the study of reaction kinetics by providing ultrafast time resolution in the order of picoseconds [10, 11]. This breakthrough has offered valuable insights into the initial steps of chemical reactions that occur within incredibly short time frames. Furthermore, the latter half of the 20th century witnessed the development of computer simulations and computational methods, empowering chemists to investigate reaction kinetics using virtual models and contributing to further advancements in the field.

## 1.2 Rapid mixing for studying bimolecular reactions and biophysical processes

Most solution-phase chemical reactions and biophysical processes are diffusion-controlled bimolecular reactions, occurring when reactants are mixed under non-equilibrium conditions [12, 13, 14, 15, 16]. Rapid mixing of two or more reactants is therefore the most versatile and common method of initiating chemical reactions and biophysical processes such as protein folding and binding [17, 18, 19]. By mixing reactants faster than the reaction rate, the equilibration of the system toward a new equilibrium can be investigated using spectroscopic probes. For reactions in water at room temperature, the diffusion-limited rate constants  $k$  are in the range  $10^8 - 10^9 \text{ M}^{-1}\text{s}^{-1}$  for small molecules, as expected from the Smoluchowski expression,  $k = 4\pi RD$ , where  $R$  is the encounter radius, which is typically sum of hydrodynamic radii ( $R_1 + R_2$ ) and  $D$  is the sum of diffusion coefficients for the reactants ( $10^{-5} - 10^{-6} \text{ cm}^2/\text{s}$ ). For biomolecular processes, such as those involving DNA oligos and proteins, this corresponds to the relaxation times,  $\tau \sim 10 - 100 \text{ }\mu\text{s}$  in 1 mM solution. Therefore, to study

such reactions via rapid mixing methods, devices are needed that can mix solutions into a homogeneous state within tens of microseconds. In response to this need, various rapid mixing technologies have been developed, broadly classified as continuous flow and stopped-flow methods. The basic setup for these methods is depicted in Figure 1.1.

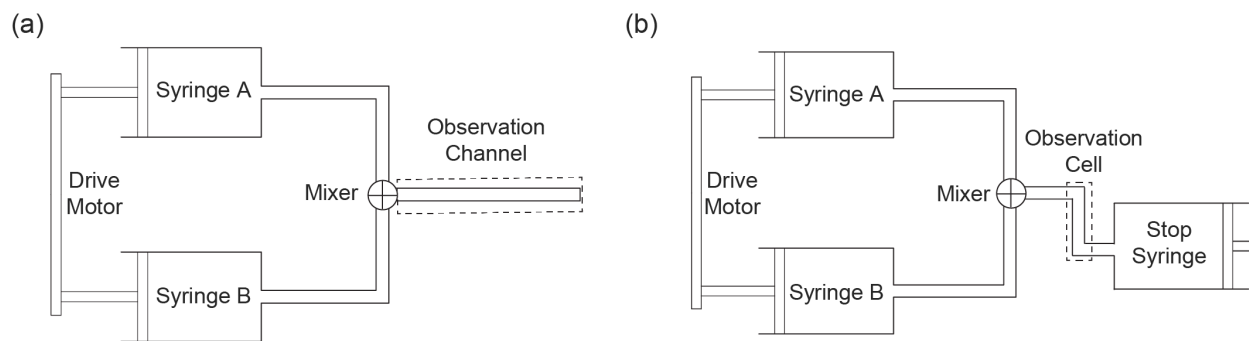


Figure 1.1: Rapid mixing strategies for time-resolved spectroscopy. (a) Continuous flow: This configuration employs syringes A and B connected to a drive motor, controlling fluid flow through a mixer. The resulting mixture is then observed at a distance from the mixer using optical probe. A continuous flow method allows for time delays to be mapped onto distance along an observation channel, with the time resolution and observable time window defined by the flow rate, the size of the IR observation beam and the dimensions of the channel. (b) Stopped-flow: Flow halts upon entering the observation cell through a stop syringe. The examination of the static point within the cell facilitates the tracking of reaction progress. The determination of time resolution and time delay hinges on several factors including mixing and transfer (‘dead’) times, as well as the scan rate of the spectroscopic probe.

### 1.2.1 Continuous-Flow method

The continuous-flow rapid mixer was first reported in 1923 by Hartridge and Roughton, to investigate molecular interactions and reactions under non-equilibrium conditions [20, 21]. This method involved mixing fluids by forcing them through high-pressure jets, resulting in their rapid and complete mixing within a confined space. The high-velocity flow ensured efficient mixing within several milliseconds. The mixed fluids passed through an observation tube, where the tube diameter and flow rate were carefully optimized so that uniform flow allowed accurate measurement of reaction progress at specific distance from the mixer using optical spectrometer. Despite this early breakthrough, the time resolution of approximately

1 millisecond, saw minimal improvement for the following 60 years due to limited engineering capabilities [22, 23, 24]. Moreover, the requirement of large quantities of solution, typically in liters, made it impractical for studying complex biological systems where obtaining such amounts of reagents was challenging. As a result, the stopped-flow method emerged, allowing experiments to be conducted with smaller volumes of solution.

### *1.2.2 Stopped-Flow method*

The roots of stopped-flow can be traced back to the early 20th century when researchers manually mixed reactants by quickly opening a valve or stopcock to initiate the reaction. However, this approach had limitations in repeatability and precision. The development of the stopped-flow apparatus by Chance revolutionized the field by enabling the study of rapid enzymatic reactions. The apparatus utilized syringes to quickly inject reactants into the mixing chamber, and a stopping syringe to halt the flow in the observation cell. Reaction progress was monitored at a fixed point using a quartz spectrophotometer [25, 26]. This controlled, rapid, and precise mixing allowed for accurate and reproducible study of fast reactions. Stopped-flow devices have undergone continuous refinement, notably the integration of independent stepping motors enhanced fluidic control, modularity and performance. Additionally, the integration of stopped-flow with other spectroscopic techniques, such as fluorescence, circular dichroism, infrared, NMR, and X-rays, has facilitated comprehensive studies of diverse processes including protein folding, ligand binding, enzyme catalysis, and polymerization [27, 28, 29, 30, 31, 32, 33, 34, 35, 36, 37]. Today, commercial stopped-flow instruments are widely utilized in research laboratories despite their high cost, often reaching thousands of dollars. The integration of a stopped-flow instrument with sophisticated detection methods, such as neutron scattering, further enhances its versatility and expands the range of applications for this technique [38].

However, achieving microsecond time resolution in kinetic measurement is challenging

for stop flow method due to the limitations imposed by the size of the mixer and observation cell. Mixing is ultimately rate-limited by molecular diffusion across boundary layers. To set the scale, the diffusion length scale for mixing in water,  $l = (4Dt)^{\frac{1}{2}}$ , is  $\sim 30 \mu\text{m}$  for a 50  $\mu\text{s}$  period. Therefore, designing a kinetic instrument capable of mixing in tens of microseconds necessitates miniaturization, typically mixing interfaces to the micron scale. Many attempts has been made to miniaturize stopped-flow apparatus by engineering a micro cuvette accessory. The best time resolution achieved with such advanced cells, compatible with fluorescence spectroscopy, is around 500  $\mu\text{s}$ . For techniques like IR spectroscopy that often require larger cells, the time resolution is typically reduced to tens of milliseconds. However, the full potential of the stopped-flow method is limited when using conventional Fourier transform (FT)-IR rapid scan spectrometers due to longer scan rate which pushes the effective time resolution to hundreds of milliseconds [34, 39, 40, 41, 42, 43]. Alternative IR techniques, such as step scan and dual comb spectroscopy which utilizes dispersion-based detection, provide excellent time resolution but come with their own challenges [44, 45, 46]. Step scan measurements require complex instrumentation, making integration with stopped-flow instruments difficult. Dual comb spectrometers, on the other hand, have limited bandwidth coverage in the mid-IR region due to their use of quantum cascade lasers as the IR source.

### **1.3 Microfluidics: Revolutionizing rapid mixing technologies**

Microfluidics, a technology that manipulates fluids through channels with dimensions ranging from tens to hundreds of micrometers, emerged in the late 1980s. It revolutionized rapid mixing by capitalizing on the unique physical properties of fluids at the micrometer scale, such as reducing diffusion distances, enhancing mass transfer, and enabling precise control over fluid flow and mixing parameters. Traditionally, silicon micromachining methods have been used to fabricate microfluidic channels from silicon and glass. The advancement in mi-

crofabrication techniques, such as photolithography and soft lithography, has expanded the range of materials used in microfluidics. Materials such as polydimethylsiloxane (PDMS), cyclic olefin copolymers (COCs) and polymethyl methacrylate (PMMA) have been successfully employed for generating microfluidic structures [47, 48, 49, 50, 51]. These materials offer advantages such as optical transparency, biocompatibility, chemical and thermal stability, low cost, the ability to seamlessly incorporate nanoscale features, and the flexibility to obtain deformable shapes.

Photolithography is a high-resolution patterning technique that uses light-sensitive materials (photoresists) and photomasks to transfer precise patterns onto a substrate. It is commonly employed for creating intricate features on microchips and serving as a master template for soft lithography. Soft lithography, on the other hand, utilizes elastomeric materials such as PDMS to replicate patterns from a master template onto a target substrate. Its elastomeric nature and excellent bonding with glass using plasma, which generates Si–OH silanol groups that undergo condensation reactions to yield a strong Si–O–Si bond allows for easy sealing of microchannels, and preventing leakage. PDMS can also bond well with itself and other materials such as silicon, PMMA, COCs to name a few making it a versatile fabrication material [52, 53, 54, 55]. When choosing between photolithography and soft lithography, several factors come into play, including resolution requirements, material compatibility, cost, and complexity. Photolithography is well-suited for high-resolution fabrication and large-scale production. In contrast, soft lithography excels in rapid prototyping and accommodating flexible design iterations, making it accessible to researchers and smaller-scale manufacturing processes.

When it comes to rapid mixer design, flow focusing, introduced by James Knight et al. in 1998, is a prominent mixer geometry. In this approach, hydraulic pressure from side channels is applied to a center inlet fluid, forming a thin stream with width in tens of nanometers. This configuration minimizes the diffusion distance, resulting in faster mixing. Flow focusing



devices have demonstrated mixing times below 10  $\mu\text{s}$  and stream widths as small as 50 nm, making them suitable for rapid kinetics measurements of biological processes such as protein folding [56, 57, 58].

To facilitate sensitive detection, fluorescence microscopy has become highly attractive analytical system for microfluidics, particularly for flow focusing mixer design, where the high sensitivity is required for the thin mixed stream. Fluorescence microscopy involves illuminating the specimen with a narrow band of wavelengths, typically ultraviolet, blue, green, or red, through an excitation filter to excite the desired fluorescent molecule. The fluorescent molecule, such as fluorescein, rhodamine, or green fluorescent protein (GFP), emits light of a longer wavelength due to Stokes shift [59, 60]. Subsequently, an emission filter is employed to selectively capture the emitted wavelengths, and the resulting images are recorded using a camera or imaging system.

Fluorescence microscopy enables the implementation of advanced techniques such as Förster resonance energy transfer (FRET) to evaluate mixer performance and investigate rapid protein folding kinetics [61, 62, 63, 64, 65]. FRET exploits the phenomenon of resonance energy transfer between compatible fluorophores through intermolecular dipole-dipole interactions. It is utilized for studying ligand-receptor binding and characterizing reaction kinetics at the molecular level. In a typical FRET assay, the donor fluorophore is excited, leading to the transfer of energy to an acceptor fluorophore, and the emission characteristics of the acceptor fluorophore are measured [66, 67, 68]. Since dipole-dipole interactions are effective only within a short distance of a few nanometers, energy transfer occurs when molecules are in close proximity, often during binding events or reactions [61, 62].

Although the fluorescence microscope has enabled high resolution optical imaging, it is generally limited by gradual reduction in fluorescence intensity on exposure to excited light, a phenomenon called photo bleaching. Furthermore, the use of labeled biomolecules presents certain drawbacks as it requires ligation and purification of the labeled product, which can be

particularly challenging for oligonucleotides extracted from biological samples. Additionally, labels can influence the energetics and kinetics of the intermolecular interactions themselves. Previous studies have reported on the impact of protein binding behaviors and DNA orientational dynamics, particularly in relation to association processes and sensitivity to the charge of the labels. [69, 70, 71].

Another approach that is commonly integrated with microfluidic mixers is UV-visible and circular dichroism (CD) spectroscopies, which offers valuable information about electronic transitions. These optical detection techniques are often considered the workhorses of stopped-flow instrumentation. However, UV-visible spectroscopy lacks the molecular information necessary to understand biological processes in depth. CD spectroscopy provides valuable information about the secondary structures and conformational changes of biomolecules. CD spectroscopy measures the differential absorption of left and right circularly polarized light, revealing structural details such as alpha-helices, beta-sheets, and protein folding/unfolding dynamics [72, 73]. CD spectroscopy complements UV-visible spectroscopy by offering specific molecular information that is crucial for understanding biological processes at a deeper level. Furthermore, it has enabled the observation of sub-millisecond timeframes in protein folding, such as characterization of secondary structure formation [74]. While CD spectroscopy holds significant promise in elucidating protein secondary structures, its drawback lies in limited chemical specificity concerning most biomolecules. This constraint arises from its inability to provide intricate details about specific functional groups and chemical bonds that constitute the molecular framework.

In contrast, IR spectroscopy offers greater chemical specificity, and direct insights into hydrogen bonding enabling the detailed analysis of specific functional groups and chemical bonds within biomolecules. One of the principal advantages of IR spectroscopy as a tool for structure-specific investigations is its ability to generate a comprehensive spectrum for each measurement time point. Consequently, multiple spectral windows can be simultaneously

examined. For instance, in the context of protein folding, this enables the observation of folding/unfolding processes, the formation of various secondary structure elements, as well as events associated with alterations in tertiary structure. Another significant advantage of IR spectroscopy is its capacity to characterize biomolecular structures under physiological conditions without the need for labeling agents. These attributes significantly enhance its applicability, particularly in situations involving rapid mixing.

### 1.3.1 Combining microfluidics with IR spectroscopy

The field of IR spectroscopy has seen limited development in rapid mixing technique despite its key advantages in studying the dynamics and kinetics of biomolecules. IR spectroscopy is highly sensitive to intermolecular interactions and changes in chemical structure without the need for exogenous labels, making it an ideal tool for investigating molecular processes. It also offers high time resolution with techniques like 2D IR spectroscopy, allowing direct monitoring of sub-picosecond dynamics. The major challenge in integrating rapid mixers with IR spectroscopy is the poor infrared transparency of current microfabrication materials, such as PDMS, PMMA, COCs, and glass. This challenge can be addressed by fabricating the microchannels in substrates that transmit in the mid-infrared vibrational fingerprint region ( $\omega = 4000 - 400 \text{ cm}^{-1}$ ,  $\lambda = 2.5 - 25 \text{ }\mu\text{m}$ ).

CaF<sub>2</sub> is an attractive material choice as it is transparent in the visible and up to 10  $\mu\text{m}$  in the mid-IR, allowing for simultaneous measurements in both ranges, and offers mechanical durability, chemical compatibility, and relative affordability. However, photolithography processes are not optimized for CaF<sub>2</sub> as a substrate, making reproducible fabrication challenging. Dyer *et al.* devised an innovative method to incorporate mixer designs by cutting microfluidic channels through a polymer spacer using a laser and sandwiching them between two IR transparent windows [75, 76]. These devices have limited applications due to the poor resolution of the laser cutter, which restricts the microchannel dimensions to hundreds

of microns. Other attempts to fabricate microchannels in  $\text{CaF}_2$  involved wet etching with strong acids [77, 78]. The resistance of  $\text{CaF}_2$  to acids limits the microchannel design to a simple linear geometry, and the slow etching process hampers its utility for fabricating microchannels, resulting in reduced effectiveness and practicality.

Silicon (Si) is widely used in lithography and exhibits transparency in the infrared region, making it the material of choice for numerous researchers [79, 80, 81, 82]. Early work by Lendl *et al.* focused on developing IR-compatible micromixers using silicon, leveraging advancements in photolithography. They fabricated diffusion-based mixers on Si and bonded them to  $\text{CaF}_2$ , enabling IR spectroscopy and microscopy measurements spanning the mid-IR regions. They performed IR measurement of the hydrogen-deuterium exchange process demonstrating the devices ability to make time-resolved kinetic measurements [83, 84, 85, 86, 87]. However, Si has huge reflective losses and gives rise to formation of interference fringes commonly known as etaloning effect that make measurements difficult [88, 89]. Additionally, incorporating brittle Si required sophisticated micromachined flow cells, making the device fabrication specialized, time consuming, and expensive.

Microfluidic devices constructed from PDMS are readily fabricated with soft lithography and suitable for rapid prototyping, but PDMS strongly absorbs mid-IR. Krummel *et al.* developed a PDMS-based microfluidic device that could be used for IR spectroscopy by reducing the polymer thickness to hundreds of microns [90, 91]. These devices were used with transmission IR microscopy to study enzyme kinetics of glucose oxidase [92]. However, reducing the thickness of polymer compromises the durability and mechanical strength of the device, which becomes crucial for mixers that require high flow rates for sufficient mixing. While numerous improvements have been made to enhance durability, most of them involve using materials that are not completely transparent to IR wavelengths [93, 94, 95].

Another approach to address the poor IR transparency challenge in conventional microfluidic materials is utilization of the attenuated total reflectance (ATR) measurement mode.

Kazarian et al. developed a device for ATR-FTIR spectroscopic imaging of continuous-flow reactions, incorporating a PDMS top layer with microchannels and an ATR crystal [96, 97]. In ATR spectroscopy, an infrared beam is directed at an angle onto the surface of the ATR crystal, resulting in total internal reflection. This setup eliminates the issue of polymer absorption as the IR light never reaches the polymer. They successfully monitored the mixing of a D<sub>2</sub>O flow with H<sub>2</sub>O in a Y-shaped mixer to demonstrate IR imaging with the device.

Despite the progress made in developing IR-compatible microfluidic devices to address the challenge of poor IR transparency, there is still a notable gap in their application for measuring kinetics in the micro to millisecond range. The emphasis thus far has been primarily on demonstrating the compatibility of these devices with IR spectroscopy, rather than focusing on their ability to capture rapid molecular processes that IR spectroscopy excels at. Additionally, the reproducibility of these devices in a general lab setting remains a significant challenge. The limited versatility of these devices is often attributed to the specialized fabrication techniques required, making it challenging to adapt them to different experimental setups.

In this thesis, we present the design, microfabrication, and characterization of a versatile and robust CaF<sub>2</sub>-based continuous-flow device. Our approach overcomes the challenges associated with material IR transparency and device integrity, allowing for reproducible fabrication in any research institution equipped with a clean room and 3D-printing facility. The primary objective of this technology is to enable high structural and kinetic resolution, thereby facilitating investigations into chemical reaction kinetics and biomolecular processes occurring within the timescale of hundreds of microseconds. We performed a pH-dependent kinetic study of the reduction reaction of ferricyanide to ferrocyanide by L-ascorbic acid, showcasing the device's ability to accurately measure kinetics in hundreds of microseconds to millisecond timescale. Furthermore, we expanded the scope of our technology to achieve even higher time resolution in the tens of microseconds range by incorporating measurements

with a tightly focused IR beam from a laser.

By combining our device’s robust design, reproducible fabrication process, and its ability to capture rapid molecular processes with exceptional time resolution, the research presented in this thesis makes a substantial contribution to the field of time-resolved vibrational spectroscopy. This work extends the horizons for investigating non-equilibrium biomolecular processes, such as DNA hybridization and protein folding, with a level of detail previously unattainable. By doing so, it offers invaluable insights into the reaction mechanisms, kinetics and dynamics.

## 1.4 Thesis Outline

This thesis is structured as follows.

Chapter 2 provides necessary theoretical background on fluid dynamics to describe the behavior of fluids in confined geometries within the microchannels. The fundamental fluid properties such as viscosity and density is crucial in developing physical intuition of flow pattern in the channel, these are explored through dimensionless Reynolds and Peclet numbers. A detail analysis of pressure-driven Poiseuille flow in the circular and rectangular channels is provided starting from governing equations followed by discussing the complexity of mixing in the microchannels.

In Chapter 3 we discuss the details of IR compatible rapid mixing instrumentation, including the mixer and observation channel design principles, characterization of the IR beam profile, time resolution and time delay for kinetic measurement. The subsequent sections of the chapter offer a more in-depth exploration of the fabrication process for a rapid mixer on a  $\text{CaF}_2$  substrate, incorporating photolithography techniques. Additionally, we elucidate the challenges associated with bonding, and to aid in comprehension, we provide visual examples to illustrate these complexities.

Chapter 4 centers around the integration of a  $\text{CaF}_2$ -based micromixer into a flow cell and

characterizing its performance. Mixing efficiency is assessed both qualitatively and quantitatively using optical and fluorescence microscopies. Furthermore, the IR compatibility of the mixer is validated by performing pH jump experiment of adenosine mono phosphate.

Chapter 5 outlines the procedure for obtaining time-resolved IR spectra to study reaction kinetics within the mixer. It offers in-depth information regarding the instrument parameters employed for data acquisition and explains the data processing method used to rectify background and baseline variations in the IR spectra.

Chapter 6 demonstrates the mixer's ability to resolve relaxation processes occurring within 1 millisecond by investigating the pH dependence of the reduction reaction of ferricyanide by ascorbic acid. The strategies used for extracting the relaxation rates from kinetic data employing exponential fitting and normalization techniques are discussed in detail. Furthermore, the chapter provides preliminary results on reduction reaction at high pH demonstrating the mixer's ability to measure relaxation process occurring as fast as 250  $\mu s$ .

# CHAPTER 2

## MICROFLUIDIC THEORY

### 2.1 Overview

Microfluidic devices are primarily designed for handling fluids, which are substances that flow, deform, and change shape when subjected to external forces or stresses. Unlike solids, fluids do not have a fixed shape but instead adjust their surface to fit the contours of their container. Fluid dynamics and hydrodynamics are continuum approaches that allow us to describe the behavior of fluids in non-equilibrium conditions. Hydrodynamics specifically deals with the flow and transport of objects through a fluid while taking into account resistance or friction. The continuum hypothesis assumes that a fluid's macroscopic properties remain unchanged when treating it as a perfectly continuous medium, disregarding its actual composition composed of individual molecules. Even in very small devices and geometries, fluids, especially liquids, can be considered to be continuous.

The primary objective of this chapter is to offer fundamental understanding of fluid behavior in confined geometries within microfluidic devices. To achieve this goal, we will cover various topics. We start by introducing fundamental fluid properties and the governing equations in fluid dynamics, laying the groundwork for the subsequent discussions. Next, we delve into the exploration of pressure-driven Poiseuille flow, where we solve the governing equations for circular and rectangular microchannels. By doing so, we aim to develop a physical intuition for this type of flow, which is commonly encountered in microfluidic systems. During this investigation, we emphasize the significance of dimensionless Reynolds and Peclet numbers as valuable tools for characterizing flow behavior and mixing phenomena within microfluidic devices. These dimensionless numbers play a crucial role in understanding the relative importance of inertial forces, viscous forces, and convective and diffusive transport in the microscale flow regimes. A particular focus is placed on mixing in microchannels, a



complex topic with limited theory and experimental development. Due to the laminar flow conditions, achieving efficient mixing within short timescales is challenging in microchannels. Therefore, strategies involving convective stirring are discussed to overcome this limitation.

## 2.2 Viscosity and its role in fluid flow in the microchannel

The unique characteristic of microfluidic systems lies in their small dimensions (typically in tens of micron), which suppress non-linear inertial effects and bring to the forefront physical phenomena that are less pronounced in macro-scale systems. To understand this, we start by developing the notion of viscosity. Consider a scenario of fluid flow between two infinite parallel planes, perpendicular to the  $y$ -direction and separated by a distance  $H$ , as shown in Figure 2.1.

Plane 2 is stationary, while plane 1 with surface area  $S$ , moves parallel to itself due to a tangential force (often referred to as shear force). The fluid is dragged along by the moving plane. Under steady state conditions (i.e. after a sufficiently long time has elapsed since the plane 1 was set in motion), the fluid velocity varies linearly within the region between the plates:  $u_x(y) = \frac{Vy}{H}$ , where  $Vy$  is the velocity in the  $y$ -direction and  $y$  is the distance from the stationary plane. The maximum velocity,  $U$ , occurs at plane 1, and for simplicity, we assume that the fluid velocity relative to the stationary plane is zero; this condition is called the no-slip boundary condition. Therefore,  $u_x = 0$  when  $H = 0$ . The deceleration of the velocity field is a result of the opposing frictional force,  $F_x$ , acting tangentially to the moving plane. There is a proportional relationship between this force (per unit surface area  $S$ ), which opposes the relative motion of the fluid, and the velocity gradient from one plane to the next, as given by Equation 2.1.

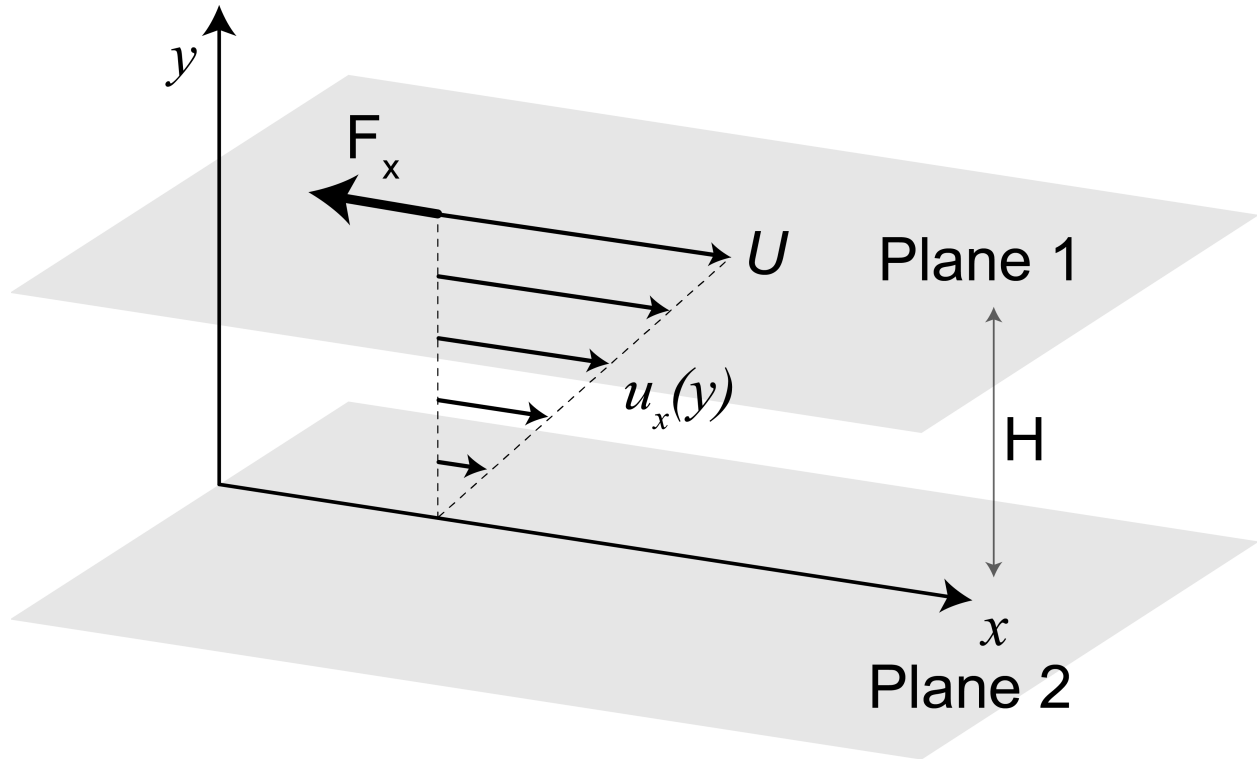


Figure 2.1: Illustration of shear flow of fluid between two planes. The application of shear force causes the movement of one plane with respect to the other, and the internal friction force  $F_x$ , between the fluid sets up a velocity gradient along  $y$ . The relationship between this opposing force per unit surface area and viscosity is expressed by Equation 2.1.

$$\frac{F_x}{S} = -\mu \frac{du_x}{dy} \quad (2.1)$$

The proportionality factor,  $\mu$ , in Equation 2.1 represents the dynamic viscosity of the fluid. Dynamic viscosity is a measure of a fluid's resistance to flow or deformation under an applied shear stress. Shear stress refers to the force per unit area that acts parallel to the surface of the fluid, while shear rate is the rate at which adjacent layers of the fluid move relative to each other. Moreover, the dynamic viscosity quantifies the internal friction within the fluid

as it flows and determines how easily the fluid can be sheared or moved. For the context of this thesis, we focus on flow of incompressible Newtonian fluids. These fluids maintain a constant density and follow Newton's law of viscosity, which describes a linear relationship between shear stress and shear rate.

### 2.2.1 Momentum Transport

With an understanding of dynamic viscosity, we can now explore the two main mechanisms involved in momentum transport in fluid dynamics: diffusion and convection. Diffusion involves the transfer of momentum through random molecular motion. In the case of uniform parallel flow, the (transverse) momentum flux is influenced by viscosity, typically represented by  $\mu \frac{du_x}{dy}$  derived from Equation 2.1. For most systems, the magnitude of this flux is on the order of  $\frac{\mu U}{L}$ , where  $U$  is the characteristic velocity, and  $L$  is a characteristic length of the flow. Since viscosity plays the major role, the forces associated with momentum changes in diffusive transport are referred to as viscous forces.

Convection, on the other hand, refers to the bulk movement of fluid particles driven by pressure or temperature gradients. In the case of uniform parallel flow with a constant vector velocity, the momentum flux is  $\rho \mathbf{U}$ , where  $\rho$  is the fluid density. The energy associated with convection can be described by dynamic pressure or velocity pressure, given by  $\frac{1}{2} \rho U^2$ . Since this transport is influenced by the fluid density  $\rho$ , the forces involved are referred to as the inertial forces. In microfluidics, diffusion is the prevailing mechanism for momentum transport. As the size of the system decreases, the surface area to volume ratio increases significantly, leading to the dominance of surface effects while volumetric effects, such as inertial forces, become negligible compared to viscous forces.

### 2.2.2 Reynolds and Peclet Number

The importance of different forces and interactions can be assessed using dimensionless numbers, with the Reynolds number ( $Re$ ) being one of the most widely used.  $Re$  compares the ratio of inertial forces (convective flux of momentum,  $\rho U^2$ ) to viscous forces (diffusive flux of momentum,  $\frac{\mu U}{L}$ ) and given by the following equation:  $Re$  plays a crucial role in determining the flow pattern and given by the following equation:

$$Re = \frac{f_i}{f_v} = \frac{\rho \cdot U \cdot L}{\mu} \quad (2.2)$$

$Re$  plays a crucial role in determining the flow pattern. In microfluidic channels, the typical fluid velocities are on the order of centimeters per second, and the channel widths are in the range of tens of micrometers. Consequently,  $Re$  is typically less than 1, indicating a low Reynolds number flow regime. In this regime, the fluid flow is laminar, characterized by smooth parallel lines of flow. As a result, laminar flow is stable and predictable. On the other hand, when  $Re$  is large ( $Re > 10,000$ ), the flow velocity field becomes unstable, resulting in vortices and eddies (spinning and swirling motions within a fluid) that dissipate the kinetic energy of the fluid, as shown in Figure 2.2. This flow pattern is characteristic of turbulent flow. In turbulent flow, the fluid exhibits irregular fluctuations and chaotic behavior.

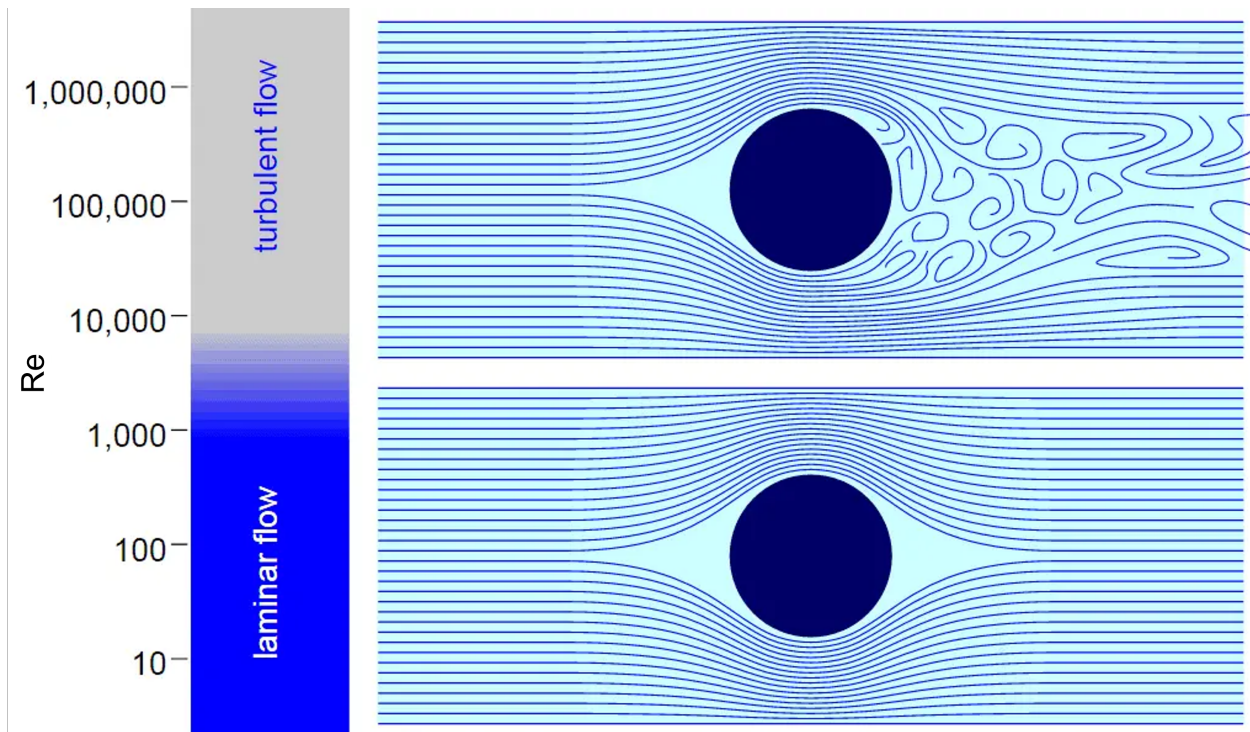


Figure 2.2: Laminar and turbulent flow. In laminar flow, the velocity field remains constant and exhibits minimal fluctuations or irregularities. The magnitude and direction of the velocity vector at any given point in the flow do not change significantly over time. The streamline (blue lines) are imaginary lines that represent the instantaneous direction of fluid flow and provide visualizations of the flow pattern and are constructed in such a way that at any given point, the tangent to the streamline indicates the direction of the fluid velocity vector. In other words, streamlines provide a snapshot of the path that a tiny fluid particle would follow as it moves through the medium. For laminar flow, the streamline remain smooth and do not intersect, resulting in well-defined and predictable flow patterns. Turbulent flows imply that the laminar flow is unstable and not observed. Turbulent flows are defined by their unsteady and rotational nature, with fluid particles exhibiting circular or rotational patterns around a central axis. (Freely adapted from nuclear engineering [1])

Laminar flow is not ideal for mixing in the micro channel. Typical microfluidic systems encounter Reynolds numbers much lower than the turbulent transition range (2000-3000). To increase  $Re$ , one can either raise fluid velocity or characteristic length. Achieving extremely high velocities (up to 100 m/s) is possible in theory, but practical constraints limit velocities to 1-10 m/s in microfluidic systems. This results in maximum Reynolds numbers in the hundreds, remaining well below the threshold for turbulent flow. Therefore, strategies such

as twisted turn are often employed in mixing applications and will be discussed in detail in section 2.5.

Another essential dimensionless number in fluid dynamics is the Peclet number ( $Pe$ ), which characterizes the ratio of convective transport to diffusive transport of a quantity within a fluid flow. This dimensionless parameter becomes particularly relevant in continuous flow applications where both convection and diffusion processes are involved. Mathematically, the Peclet number is defined as:

$$Pe = \frac{U \cdot L}{D} \quad (2.3)$$

In Equation 2.3,  $U$  is the characteristic velocity of the flow,  $L$  is a characteristic length scale, and  $D$  is the diffusion coefficient of the quantity being transported. The Peclet number accesses whether convection is faster than molecular diffusion in mixing applications. For example, for a solution of protein ( $D = 1 \times 10^{-9} \text{ m}^2\text{s}^{-1}$ ) flowing at  $U = 100 \text{ }\mu\text{m/s}$  through a channel of width  $100 \text{ }\mu\text{m}$ , the Peclet number  $Pe = 100$ , which means that the fluid remains largely unmixed until the flow has traveled a distance 100 times the width of the channel or mixing time of 100 seconds. This time is large and we will discuss strategies such as inducing *chaotic advection* for reducing the mixing time in section 2.5.

### 2.2.3 Pressure and fluid resistance in microchannel

Pressure and fluid resistance are crucial topics in fluid mechanics due to their significant impact on various aspects of fluid behavior and the design of fluidic systems. Pressure gradients drive fluid flow from regions of high pressure to low pressure. Fluid resistance, often characterized by terms like viscosity affects the flow rate and energy losses in a system.

The flows of incompressible Newtonian fluids along a channel due to characterized by a characteristic scale length  $L$ , the velocity of the fluid  $U$ , can be estimated using the relation:

$$U \sim \frac{\Delta PL}{\mu} \quad (2.4)$$

Here,  $\Delta P$  represents the pressure difference required to initiate fluid motion. In practice, flow in microfluidic systems is often generated by applying a pressure difference at the inlet, such as by pushing the piston of a syringe. Typical values for  $\Delta P$  are on the order of one bar when corresponding  $Re$  is less than 1. This poses challenges for efficient mixing because the exploitation of turbulence becomes difficult at reduced length scales. Turbulent flow is characterized by enhanced mixing and increased hydrodynamic resistance compared to laminar flow. Hydrodynamic resistance is explained by *Poiseuille's Law* in fluid dynamics. In general, the resistance is directly proportional to viscosity and channel length, and inversely proportional to the some power of the channel's characteristic dimension. For circular and rectangular microchannels, the resistance is given by following equations:

$$R = \frac{8\mu L}{\pi r^4} (\text{circular}) \quad (2.5)$$

$$R = \frac{12\mu L}{w \times h^3} (\text{rectangular}) \quad (2.6)$$

In theses equation,  $R$  is the fluid resistance,  $\mu$  is the fluid viscosity,  $L$  is the length of the channel, and  $r$  is the radius of the circular channel, and for rectangular channels,  $w$  and  $h$  represent the width and height, respectively. The hydrodynamic resistance can also be expressed in terms of the pressure difference ( $\Delta P$ ) across the channel and the flow rate ( $Q$ ) as  $R = \frac{\Delta P}{Q}$ .

These equations hold vital implications, both in the context of the human body and microfluidic channels. Let's first consider the impact on blood flow dynamics within the human body. For instance, when examining the flow through circular capillaries, if the radius of a capillary decreases by a factor of 2, the fluid resistance increases significantly

by a factor of 16. Consequently, this heightened resistance leads to a corresponding rise in blood pressure. Thus, changes in capillary dimensions can have a considerable impact on blood flow dynamics and pressure regulation within the human circulatory system.

Similarly, in microfluidic channels, where most fabrication methods yield rectangular microchannels, the fluid resistance is notably sensitive to the height of the microchannel. If the height is reduced by a factor of 2, the fluid resistance increases by a factor of 8. As a result, this increase in resistance manifests as a heightened pressure drop required to drive the flow through the channel. For example, consider a 100  $\mu\text{m}$  wide, 10mm long microchannel. Reducing the height from 30  $\mu\text{m}$  to 15  $\mu\text{m}$ , the fluid resistance increases three fold, and at a typical flow rate of 10  $\mu\text{L/s}$  used for mixing application, the pressure drop escalates from 7 bars to 57 bars. Such an increase in pressure drop necessitates syringe pumps with high linear force driving motors and syringes capable of withstanding high pressure, such as stainless steel syringes. Generally, common plastic syringes have pressure ratings less than one bar and glass syringes have ratings around ten bars.

## 2.3 Governing equations in fluid dynamics

In this thesis, our primary focus is on exploring the physics of incompressible Newtonian fluid flow within microchannels. By considering incompressibility, we can significantly simplify the fluid flow equations, assuming uniform density and neglecting the transfer of energy from kinetic energy (velocity) to internal energy (temperature). The governing equations for incompressible laminar fluid flow consist of conservation of mass (continuity) and momentum, commonly known as the Navier–Stokes equations.

To describe the conservation laws, the concept of a ‘control volume’ (Eulerian approach) is widely used in most fluid mechanics textbooks. This approach proves to be more suitable than the traditional ‘control mass’ (Lagrangian approach), as fluid is inherently a continuously deformable medium.



Given the length constraints of this thesis, we will not delve into an in-depth derivation of these conservation equations. Instead, our focus will be on exploring the implications of these equations in microfluidic systems. For a more comprehensive understanding and detailed derivations, one can refer to the following reference textbooks: [98, 99, 100].

### 2.3.1 Continuity Equation

The continuity equation is a fundamental equation in fluid mechanics that embodies the principle of mass conservation. It states that for a fluid flowing through a control volume, the rate of mass entering the volume is equal to the rate of mass leaving the volume. In other words, the total mass within the control volume remains constant over time. The mathematical representation of the continuity equation is as follows:

$$\frac{\partial \rho}{\partial t} + \nabla \cdot (\rho \mathbf{u}) = 0 \quad (2.7)$$

In Equation 2.7,  $\mathbf{u}$  represents the velocity field and  $\nabla$  is the gradient operator given by  $\nabla = \left( \frac{\partial}{\partial x}, \frac{\partial}{\partial y}, \frac{\partial}{\partial z} \right)$ .

In the case of incompressible fluids, where the density remains constant throughout the flow field regardless of changes in pressure or velocity ( $\frac{\partial \rho}{\partial t} = 0$ ), the continuity equation simplifies to the following form:

$$\nabla \cdot \mathbf{u} = 0 \quad (2.8)$$

The divergence of a velocity field ( $\nabla \cdot \mathbf{u}$ ) can be thought of as the expansion or contraction of the flow at a specific point. When the divergence is zero, it signifies that the fluid flow is neither converging nor diverging at that point, implying incompressible behavior and adherence to the principle of mass conservation..

### 2.3.2 The Navier-Stokes equation - Momentum conservation

The Navier-Stokes equations are a set of partial differential equations that govern the motion of a fluid. The equations are extension of Newton's second law to control volumes and derived from the principles of continuity equation (Equation 2.7), conservation of momentum, and conservation of energy. The conservation form of the incompressible Navier-Stokes equation is as follows:

$$\rho \left( \frac{\partial \mathbf{u}}{\partial t} + \mathbf{u} \cdot \nabla \mathbf{u} \right) = -\nabla p + \mu \nabla^2 \mathbf{u} + \mathbf{f}_b \quad (2.9)$$

In Equation 2.9, the left-hand side contains the inertial acceleration terms, representing the rate of change of momentum of the fluid. The right side of the equation is summation of hydrostatic effects, expressed as external forces. The pressure force (represented as the pressure gradient  $\nabla p$ ) acts in the direction of decreasing pressure (hence the negative sign). The viscous force is given by  $\mu \nabla^2 \mathbf{u}$ , where the Laplacian of the velocity field describes the spatial variation of velocity within the fluid. The body forces ( $\mathbf{f}_b$ ) account for any other forces acting on the fluid, such as gravity or electromagnetic forces [101].

In microfluidic applications, the flow is typically laminar, and the inertial acceleration terms are negligible. Consequently, the non-linear convective term  $\mathbf{u} \cdot \nabla \mathbf{u}$  in the Navier-Stokes equation can be omitted. Additionally, in simple microfluidic flow scenarios, external body forces such as gravity or electromagnetic forces can be considered insignificant. When combined with the incompressibility condition, the simplified Navier-Stokes equation takes on a linear form:

$$-\nabla p + \mu \nabla^2 \mathbf{u} = 0 \quad (2.10)$$

This form is called the Stokes equation and provide a simplified description of fluid behavior in microchannels. By removing non-linear terms, it becomes easier to solve compared

to the full Navier-Stokes equation as we will see example in the following sections.

## 2.4 Analytical solution to pressure driven flow

Pressure-driven flow, commonly known as *Poiseuille flow*, serves as the prevailing flow type in microfluidic applications. This phenomenon relies on generating a pressure gradient within the microfluidic device to propel the fluid from the high-pressure inlet to the low-pressure outlet. Analytical solutions can be derived for pressure-driven flow in microchannels for specific cases.

### 2.4.1 Hagen-Poiseuille flow

*Hagen-Poiseuille* flow refers specifically to pressure-driven flow through a tube of circular cross section with fixed width. To solve for the *Hagen-Poiseuille* flow, we make the assume steady state flow, i.e, the velocity, pressure, and other flow properties remain constant with respect to time.

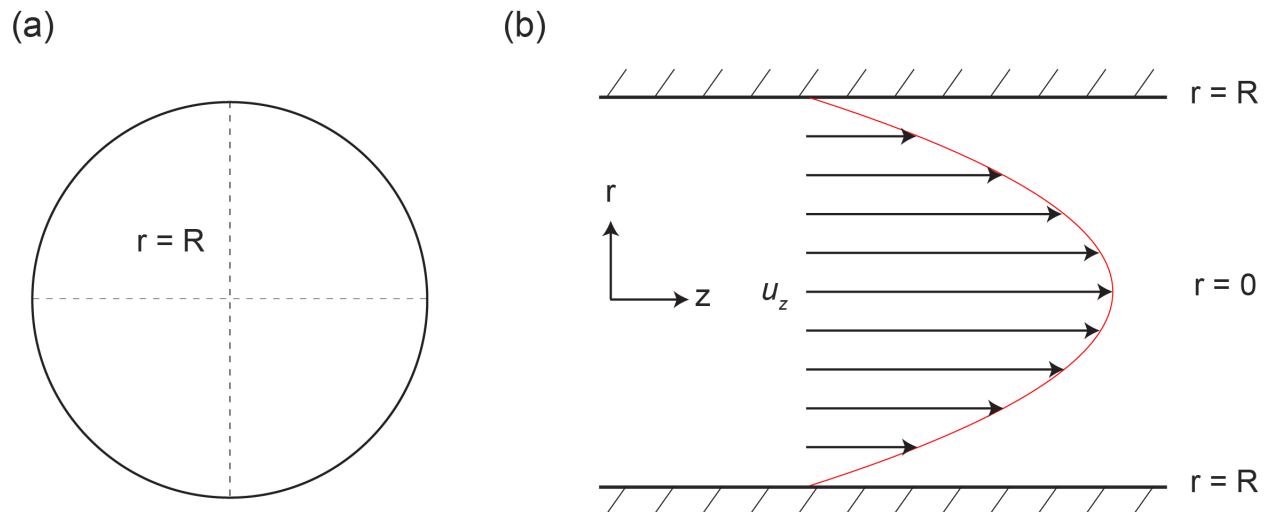


Figure 2.3: (a) Circular channel with radius,  $r = R$  and origin at the center, top view (b) The velocity distribution in the circular channel shown in a cutaway view. At the center of the channel, the velocity is maximum, and as we move towards the wall of the channel, the velocity decreases. This parabolic velocity profile is a characteristic feature of pressure-driven flow in circular channel.

For axisymmetric flow, the Stokes equation (Equation 2.10) can be written as:

$$\frac{\partial p}{\partial z} = \mu \frac{1}{r} \frac{\partial}{\partial r} r \frac{\partial u_z}{\partial r} \quad (2.11)$$

To solve, we assume that the pressure gradient,  $\frac{\partial p}{\partial z}$  is uniform, and integrate the  $r$  terms:

$$\frac{\partial p}{\partial z} \frac{1}{2} r^2 + C_1 = r \mu \frac{\partial u_z}{\partial r} \quad (2.12)$$

Rearrange:

$$\frac{\partial u_z}{\partial r} = \frac{\partial p}{\partial z} \frac{r}{2\mu} + \frac{C_1}{\mu r} \quad (2.13)$$

and integrate again with respect to  $r$  to get the velocity field:

$$u_z = \frac{\partial p}{\partial z} \frac{r^2}{4\mu} + \frac{C_1}{\mu} \ln r + C_2 \quad (2.14)$$

The integration constants  $C_1$  and  $C_2$  is determined by applying the following boundary conditions.

- **Bounded velocity at the center:** The velocity field should be bounded at the center of the tube (at  $r = 0$ ). This requires that there is no singularity in the velocity ( $u_z$  should remain finite and well-behaved), which means that the term  $\frac{C_1}{\mu} \ln r$  should not become infinitely large as  $r$  approaches 0. Therefore,  $C_1$  must be equal to zero to avoid the logarithmic term becoming undefined at  $r = 0$ .
- **No slip condition:** This means that the fluid velocity ( $u_z$ ) at the walls of the tube (at  $r = R$ , where  $R$  is the radius of the tube) is assumed to be zero. This condition leads to  $C_2 = -\frac{\partial p}{\partial z} \frac{R^2}{4\mu}$

Finally, we arrive at the *Hagen-Poiseuille* solution as:

$$u_z = -\frac{r^2}{4\mu} \frac{\partial p}{\partial z} (R^2 - r^2) \quad (2.15)$$

Equation 2.15 suggests that the velocity distribution of a *Poiseuille flow* is parabolic and shown in Figure 2.3 b.

In microfluidic application, flowrate is generally an independent parameter and therefore it makes sense to extend the solution to relate to the flow rate. The volumetric flow rate  $Q$  is the total volume of fluid passing through a given cross-section per unit time. To calculate  $Q$ , we integrate  $u_z$  across the cross-section from  $r = 0$  to  $r = R$ :

$$Q = \int_0^R u_z 2\pi r dr \quad (2.16)$$

By substituting the expression of  $u_z$  from Equation 2.15, and performing the integration, we end with the following expression for  $Q$ :

$$Q = -\frac{\pi R^4}{8\mu} \frac{\partial p}{\partial z} \quad (2.17)$$

As fluid viscosity decreases, pressure increases to maintain the same flow rate due to conservation of mass. The pressure gradient remains constant to sustain flow. The velocity profile in *Hagen-Poiseuille flow*, initially parabolic, changes with lower viscosity. Reduced viscosity reduces flow resistance near the walls, increasing velocity near the walls and making the profile more uniform across the tube's cross-section. For simplicity, equation 2.17 is often area normalized to get approximation for the average velocity,  $u_z(avg) = \left(-\frac{\partial p}{\partial z}\right) \frac{R^2}{8\mu}$ , which is used for calibrating time. In general, the *Hagen-Poiseuille equation* highlights the significant influence of the conduit radius on the flow rate. The flow rate is directly proportional to the fourth power of the radius. Therefore, even a small change in the conduit radius can lead to a substantial alteration in the flow rate.

### 2.4.2 Flow in a rectangular micro channel

It is intriguing that an analytical solution for flow in a rectangular cross-section remains elusive. Despite the considerable symmetry of the boundary, current analytical approaches only yield a Fourier series representation of the solution. Deriving a comprehensive general solution for this complex problem is beyond the scope of this thesis. Instead, our focus will be directed towards exploring the implications of this solution, particularly how variations in the width-to-height ratio influence the velocity and flow rate within the microchannel. This analysis will prove invaluable in gaining insights into fluid flow behavior and will serve as a guiding principle for optimizing the design of our microchannel.

Let's consider a rectangular microchannel with a width,  $w$ , and height,  $h$ , as depicted in Figure 2.4 a. The general form of the velocity distribution in a rectangular channel is given by the following equation [102]:

$$u_z = \frac{1}{2\mu} \frac{\partial p}{\partial z} \left[ \left( \frac{h^2}{4} - y^2 \right) - \sum_{n=1}^{\infty} a_n \cos \left( \frac{\lambda_n y}{h/2} \right) \cosh \left( \frac{\lambda_n x}{h/2} \right) \right] \quad (2.18)$$

where  $\lambda_n = \frac{(2n+1)\pi}{2}$  and  $a_n = \frac{h^2(-1)^n}{\lambda_n^3 \cosh(\lambda_n w/h)}$  satisfies the no-slip boundary conditions at  $x = \pm \frac{w}{2}$ .

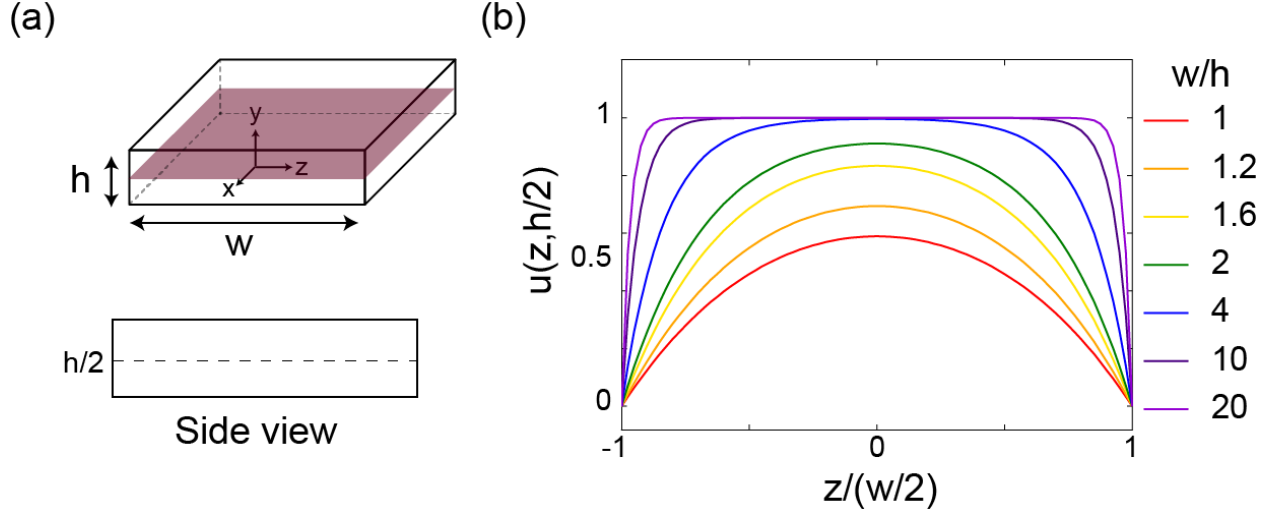


Figure 2.4: Evaluation of axial velocity distribution in a rectangular microchannel. (a) Visualization of a rectangular microchannel in 3D and side view. (b) Plot of axial velocity distribution along the center-plane (colored for clarity). The velocity profile is parabolic, and it becomes increasingly flatter in the center as the width-to-height ratio,  $w/h$ , exceeds 2.

Equation 2.18 suggests that for pressure-driven flow, the velocity distribution across the channel varies depending on various parameter. In simple case, one expect it to be parabolic. To gain a physical insight, lets consider the velocity distribution at the center of the channel, i.e.  $y = \frac{h}{2}$ , denoted by the dashed line in Figure 2.4(a) (side view). Equation 2.18 simplifies to the following equation:

$$u(z, h/2) = -\frac{1}{2\mu} \frac{\partial p}{\partial z} \left[ \sum_{n=1}^{\infty} \frac{h^2 (-1)^n}{\lambda_n^3 \cosh(\lambda_n w/h)} \cos(\lambda_n z) \cosh\left(\frac{\lambda_n x}{h/2}\right) \right] \quad (2.19)$$

The evolution of the velocity distribution from Equation 2.19 with varying  $\frac{w}{h}$  is depicted in Figure 2.4 b. A unique characteristic of the velocity distribution becomes evident when considering rectangular cross sections with  $\frac{h}{w} > 2$ . In such cases, the velocity remains relatively constant throughout the channel, except for regions near the walls where the fluid velocity is zero to satisfy the no-slip boundary condition. Consequently, in shallow microchannels, the average velocity provides a sufficiently accurate approximation of the

actual fluid velocity. This observation allows us to effectively calibrate time using the velocity and distance within the channel. This calibration is of utmost importance in time-resolved spectroscopy, particularly when performing kinetics measurements in aqueous systems. As we will explore in subsequent chapters, the width of the observation channel is designed with  $\frac{h}{w} \approx 3$  for use with an IR laser source and  $\frac{h}{w} \approx 10$  for use with a glowbar IR source, ensuring that this approximation can be reliably utilized.

The determination of the general form of the flow rate,  $Q$ , for the rectangular channel follows a similar approach to that of the circular channel. By integrating Equation 2.18 twice, we obtain the following expression for the flow rate:

$$Q = \frac{wh^3}{12\mu} \frac{\partial p}{\partial z} \left[ 1 - 6 \left( \frac{h}{w} \right) \sum_{n=1}^{\infty} \lambda_n^{-5} \tanh \left( \frac{\lambda_n w}{h} \right) \right] \quad (2.20)$$

In the limit  $\frac{h}{w} \rightarrow 0$ , which corresponds to a very shallow or wide channel, the sum term simplifies significantly due to the behavior of the hyperbolic tangent function. Specifically, as  $\tanh \left( \frac{\lambda_n w}{h} \right)$  approaches  $\tanh(\infty)$ , which is equal to 1, the term reduces to unity. Thus, the flow rate can be approximated as follows:

$$Q \approx \frac{wh^3}{12\mu} \frac{\partial p}{\partial z} \left[ 1 - 0.63 \frac{h}{w} \right] \quad (2.21)$$

Remarkably, this approximation provides an accurate estimation and can be effectively employed for most microfluidic channels. Even for the worst case scenario of a square channel with  $h = w$ , the error is only 13%. In contrast, at an aspect ratio of a half, with  $h = \frac{w}{2}$ , the error reduces to a mere 0.2%. This level of accuracy demonstrates the practical utility of the approximation.



## 2.5 Physics of mixing

The physics of mixing in microfluidics is inherently complex. In common microfluidic devices, the Reynolds numbers can be estimated based on water as the working fluid, with typical velocities ranging from 1 m/s to 1 cm/s and typical channel radii ranging from 1  $\mu\text{m}$  to 100  $\mu\text{m}$ . The resulting Reynolds numbers range between  $\mathcal{O}(10^{-6})$  and  $\mathcal{O}(10)$ . In such a low Reynolds number regime, mixing is challenging due to laminar flow. For a given reservoir size  $L$ , the time required for diffusion to mix two components in that reservoir is proportional to  $t_{mix} = \frac{L^2}{D}$ . In microscale systems, this time can be long – for example, the time required for a protein in water (where  $D \sim 10^{-10} \text{ m}^2/\text{s}$ ) to diffuse across a 100  $\mu\text{m}$  channel is about 10s. However, studies of homogeneous kinetics in solution require that a system become well-mixed on a timescale faster than the kinetics of the reaction. In the case of studying proteins, the important events leading to protein folding occur as fast as microseconds, requiring mixers capable of achieving an ultra-fast timescale, generally in the order of tens of microseconds [103, 104, 105]. However, achieving such rapid mixing times in microchannels, where flow is predominantly laminar, presents a considerable challenge. To overcome this challenge, strategies based on increasing the interfacial area to promote diffusive mixing have been employed, involving convective stirring of the fluid [106, 107, 108, 109, 110, 111]. In the cases of intermediate Reynolds number regime ( $10 < \text{Re} < 2000$ ), it is important to recognize the significant role of inertia [112, 113]. This leads to the emergence of diverse flow patterns within microchannels, which are summarized in the Appendix 2.7.2.

To further elucidate the mixing phenomenon, let's consider an example of the flow of a fluid element navigating a 90-degree turn, as depicted in Figure 2.5, might be helpful.

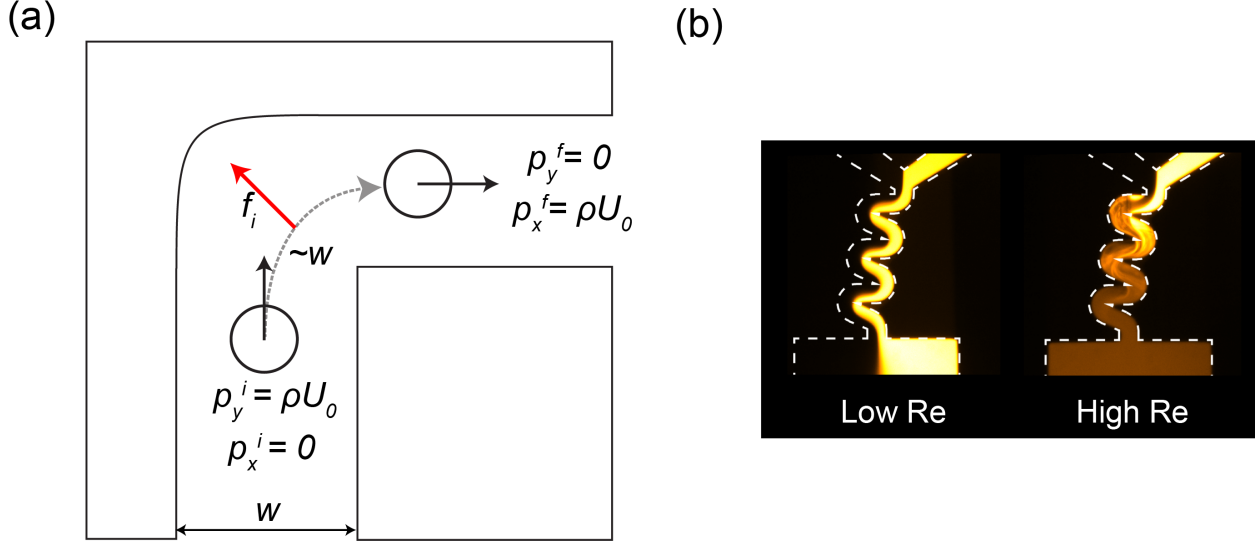


Figure 2.5: (a) Physics of fluid flowing through a turn. The fluid, flowing with a velocity of  $U_0$  and passing through a channel of width  $w$ , navigates a turn that takes a time  $\tau_0 = \frac{w}{U_0}$ . The fluid element rounding the corner experiences a loss of momentum density denoted as  $\rho U_0$  in the  $y$  direction giving rise to the centrifugal force density (red arrow), approximated as  $f_i \sim \frac{\rho U_0}{\tau_0} = \frac{\rho U_0^2}{w}$ . A comparison can be made between this inertial force and the viscous force densities, denoted as  $f_v \sim \frac{\mu U_0}{L_0^2}$ , which emerge within the flow as a result of the internal friction of the fluid. (b) Flow of a dye and quencher at low  $Re$  and high  $Re$  regimes: At low  $Re$ , the flow is laminar, and mixing is purely diffusive, difficult to observe despite passing through turns. As  $Re$  increases, fluid elements stretch and fold, leading to chaotic trajectories, enhancing mixing further along the turn.

As the fluid flows through curved channels, fluid elements near the centerline possess greater inertia than those near the channel walls. This is due to a mismatch of velocity in the downstream direction between the fluid in the channel's center and near-wall regions. This causes them to flow outward around a curve and create a pressure gradient in the radial direction of the channel. Since the channel is enclosed, relatively stagnant fluid near the walls recirculates inward due to this centrifugal pressure gradient. This flow pattern is called *secondary flow* (depicted in Figure 2.5b (High  $Re$ )) and mixing through this process is often referred to as *chaotic advection* in microfluidics literature. This process leads to an exponential decay of the characteristic length over which diffusion occurs. As a result, *chaotic advection* is a popular mixing method in microfluidic mixers.

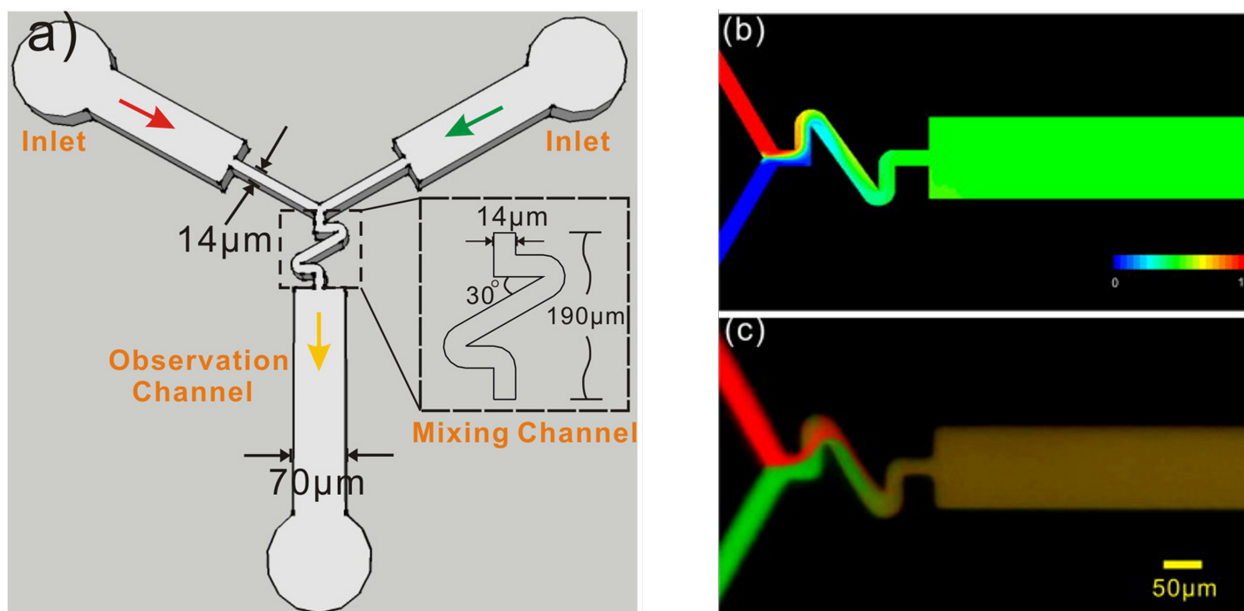


Figure 2.6: (a) Schematic of serpentine zigzag mixer design by Li *et al.* The channel geometry is designed such that the flow through zigzag stretch and fold the solution primary flow to generate narrow striations, which exponentially increase the interfacial area between the solutions and cause rapid mixing within its short channel length. Validation of the mixing efficiency: (b) Computational fluid dynamics simulation showcasing the mixing process. (c) Experimental mixing of sulfurohodamine B (red) and fluorescein (green) within the zigzag mixer, achieved at a flow rate of  $10\ \mu\text{L/s}$ . Adapted from Ref [2] (Copyright 2014, with permission from Analytical Chemistry) and Ref [3] (Copyright 2012, with permission from Talanta).

Jones *et al.* were first to demonstrated chaotic mixing through a sequence of pipe bends can lead to enhanced transverse and longitudinal stirring [114]. The twisting and turning of the fluid in the pipe bends maximize the interface between different fluid streams, promoting *chaotic advection*. Importantly, chaotic particle trajectories within this mixing scheme improved stirring quality without requiring additional energy input. Key external parameters to control mixing efficiency include the channel dimensions, radius of curvature, and flow rate. In this thesis, we implemented a modified version of a twisted pipe bends called "zigzag mixer", shown in Figure 2.6 where these parameters were optimized to enhance mixing. The details of these modifications will be discussed in Chapter 3.

Another strategy to induce *chaotic advection* involves using bas-relief structures on the

channel floor, such as a series of alternating herringbone-shaped grooves. An example of this approach is the Staggered Herringbone Mixer (SHM) by Stroock *et al.*, illustrated in Figure 2.7. This mixer is particularly significant as it can achieve effective mixing even at low  $Re$ . As the fluid traverses these grooves, it undergoes repeated stretching and folding of fluid layers. This intricate flow pattern generates time-dependent whorls, thereby reducing the length scale for diffusion to occur [4].

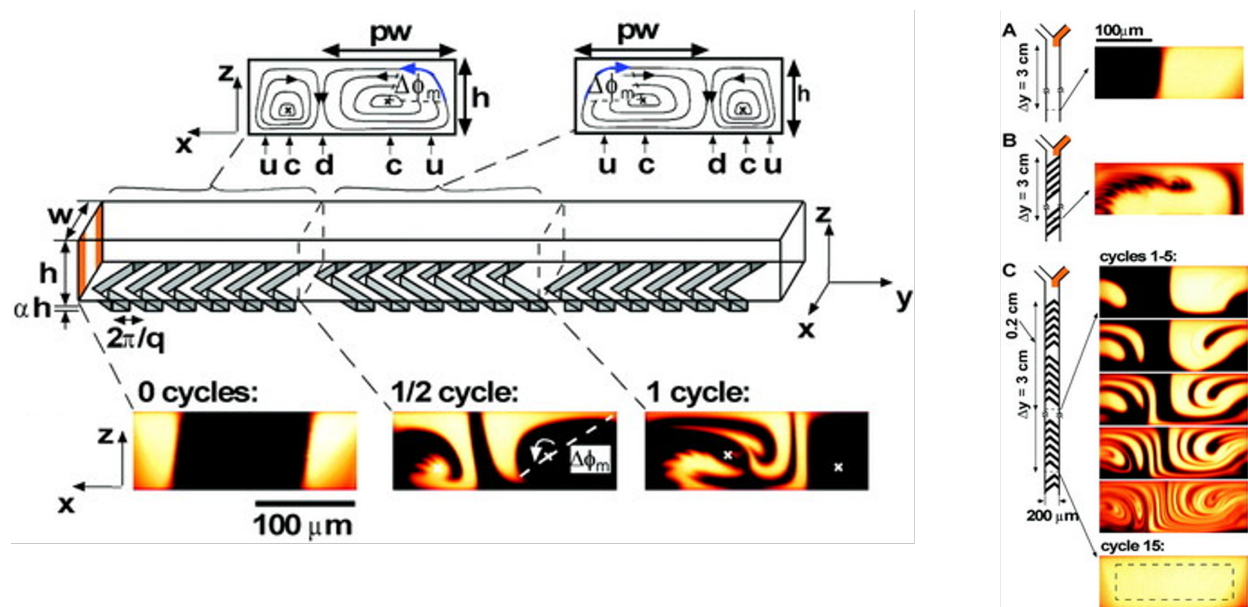


Figure 2.7: Staggered herringbone mixer (SHM). Schematic diagram of one-and-a-half cycles of the SHM. A mixing cycle is composed of two sequential regions of ridges; the direction of asymmetry of the herringbones switches with respect to the centerline of the channel from one region to the next. The streamlines of the flow in the cross section are shown schematically above the channel. The angle,  $\Delta\Phi_m$ , is the average angular displacement of a volume of fluid along an outer streamline over one half cycle in the flow generated by the wide arms of the herringbones. The fraction of the width of the channel occupied by the wide arms of the herringbones is  $p$ . The horizontal positions of the centers of rotation, the upwellings, and the downwellings of the cellular flows are indicated by  $c$ ,  $u$ , and  $d$ , respectively. (A,B,C) Cross sections of the dye distribution in a microfluidic channel designed to create staggered, time-dependent whorls or twist maps. These whorls play a role in shortening the length scales over which diffusion must act. Adapted from Ref [4] (Copyright 2002, with permission from Science).

In SHM, the characteristic mixing time or length is proportional to  $\ln(Pe)$  [4, 99]. In our previous example, we considered a protein solution with a diffusion coefficient of  $D =$

$1 \times 10^{-9} \text{ m}^2 \text{ s}^{-1}$  flowing at a velocity of  $U = 100 \text{ } \mu\text{m/s}$  through a channel with a width of  $100 \text{ } \mu\text{m}$ . Under these conditions,  $Pe = 100$  and it took 100 seconds (or 100 channel widths) for complete mixing to occur. However, when subjected to chaotic mixing conditions, this mixing time is drastically reduced to only 4.6 seconds. This is a huge improvement in shortening the mixing distance/time. The mixing time for SHM is typically in the range of milliseconds, which is an order of magnitude larger than that of "zigzag" mixers where mixing time is usually  $10 \text{ } \mu\text{s}$  or less [3, 2]. However, despite its advantages, the fabrication process of SHM involves multiple steps that could be challenging when working with a  $\text{CaF}_2$  substrate, which is why it was not pursued for this particular thesis work.

### 2.5.1 Flow from a narrow to wide flared channel

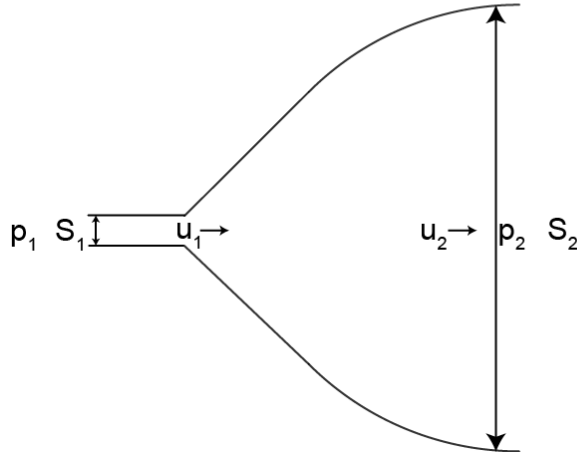


Figure 2.8: Flow through a flared channel wall. The force experienced by the flaring wall is given by  $F_{\text{wall}} = p_1(S_1 - S_2) + \frac{1}{2}\rho u_1^2 S_1 \left(2 - \frac{S_2}{S_1} - \frac{S_1}{S_2}\right)$ .

In the previous sections, we explored fluid flow in straight and curved channels. Now, we shift our focus to the flow from a narrow to flared channel, as depicted in Figure 2.8. This design is commonly employed in rapid micromixer designs, where a compact mixing

area with minimized dimensions is combined with a widened observation area. This is particularly relevant in IR spectroscopy, where the observation area must be large enough to accommodate measurement with IR beam size ranging from tens to hundreds of microns.

The transition from a narrow to a flared channel leads to variations in the forces exerted on the channel walls. Bernoulli's equation is employed to deduce the connection between the forces encountered by the channel walls throughout the flow. Assuming steady, incompressible, and inviscid (negligible viscosity) fluid flow, Bernoulli's equation establishes a connection between the pressure ( $p$ ), velocity ( $u$ ), and elevation ( $h$ ) of the fluid along a streamline as follows:

$$p + \frac{1}{2}\rho u^2 + \rho gh = C \quad (2.22)$$

Note that the Bernoulli's equation above can be modified to accounts for the energy loss due to viscous dissipation within the fluid by adding  $-\mu \left(\frac{\partial y}{\partial v}\right)^2$  on the right hand side. However, in our analysis, we assume an inviscid condition. This choice allows us to develop intuition and understand the fundamental principles of fluid flow without considering the complexities introduced by viscosity.

For the flared channel design depicted in Figure 2.8, let's denote the narrow section as subscript "1" and the wide section as subscript "2". Rearranging Bernoulli's equation, we obtain the following relationship:

$$p_2 - p_1 = \frac{1}{2}\rho(u_1^2 - u_2^2) \quad (2.23)$$

We can utilize Equation 2.23 and incorporate mass conservation, expressed as  $u_2 = u_1 \frac{S_1}{S_2}$ , to derive an expression for the force experienced by the flared wall. Considering only the force in the direction of flow, we have  $F = [p_1 S_1 + \rho u_1^2 S_1] - [p_2 S_2 + \rho u_2^2 S_2]$ . Substituting the mass conservation relationship simplifies the equation as follows:

$$F_{\text{wall}} = p_1(S_1 - S_2) + \frac{1}{2}\rho u_1^2 S_1 \left( 2 - \frac{S_2}{S_1} - \frac{S_1}{S_2} \right) \quad (2.24)$$

In cases where  $S_1 \ll S_2$ , which is common in microfluidic mixer designs, Equation 2.24 can be approximated as  $F = -S_2 \left( p_1 + \frac{1}{2}\rho u_1^2 \right)$ , indicating that the force is proportional to the surface area of the wider channel. The flared shape allows for an even distribution of this force across the channel walls, maintaining steady flow streamlines. However, if the narrow channel abruptly widens (at a 90° angle), the force will be sudden and disrupt the flow, leading to dead volume and potential damage to the channel walls.

On the other hand, when  $S_1$  and  $S_2$  are comparable in size, the force exerted on the channel walls are small or negligible. If there is no constraints set by spectroscopic measurement, it is advisable to keep the width of observation channel within a factor of five larger than the mixer.

## 2.6 Conclusion and Outlook

This chapter covered theoretical aspects of microfluidic flow, including velocity distribution in circular and rectangular microchannels, curved geometries, and flow from narrow to wide flared channels.

In analyzing rectangular microchannels, obtaining an analytical solution for the flow proved challenging. However, investigating the solution's implications revealed that the width-to-height ratio ( $\frac{w}{h}$ ) significantly influences velocity and flow rate. Shallow microchannels with  $\frac{w}{h} > 2$  exhibit a nearly constant velocity distribution, except near the walls, where the no-slip boundary condition results in zero velocity. In curved geometries, we studied flow dynamics using Newton's laws, finding that low Reynolds numbers in microfluidic devices result in predictable flow but pose challenges for efficient mixing. Strategies for enhanced mixing include twisted pipes and bas-relief structures, utilizing secondary flows and chaotic

particle trajectories. The Peclet number helps evaluate mass or heat transfer effectiveness in micro scale devices.

In light of the discussions presented, there are several avenues for future research in understanding the flow in microfluidic devices. Firstly, the quest for analytical solutions in rectangular microchannels remains an open challenge. Alternative approaches using numerical methods such as computational fluid dynamics simulation could yield valuable insights into the velocity distribution and flow behavior within these channels. Furthermore, exploring the effects of additional factors, such as channel surface properties or flow modifiers, on the velocity profile and flow rate could lead to novel design strategies for microfluidic devices.

In curved geometries, further investigations into the relationship between the channel curvature, number of turns, Reynolds number, and mixing efficiency would be valuable. Additionally, exploring the impact of different fluid properties, such as viscosity or density variations, on the flow behavior in curved channels could uncover new insights into fluid dynamics and improve the design of microfluidic mixers.

## 2.7 Appendix

### 2.7.1 *Ohm's and Kirchhoff's law analogs in pressure driven flow*

The elementary rules of circuit design, based on laws of Ohm and Kirchhoff, can be extended to the analysis of pressure-driven flow in fluid systems as follows:

**Ohm's law analogy:** Ohm's law relates current density  $\mathbf{j}$  to electric field  $\mathbf{E}$  as  $\mathbf{j} = \sigma\mathbf{E}$ , where  $\sigma$  is conductivity. In fluid flow, the analogous relationship is Darcy's law, which relates average velocity  $\mathbf{u}_{\text{avg}}$  to pressure gradient  $\nabla p$  as  $\mathbf{u}_{\text{avg}} = -\frac{k}{\mu}\nabla p$ , where  $k$  is permeability dependent on channel shape and  $\mu$  is the viscosity.

**Kirchhoff's law analogy:** In fluid flow systems, the principle analogous to Kirchhoff's Law in electrical circuits is that the total flow rate entering a junction is equal to the total



flow rate leaving that junction, ensuring mass conservation.

Table 2.1 provides a comparison of basic terminologies in electrical and fluidic system.

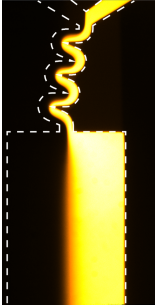

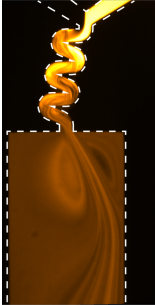
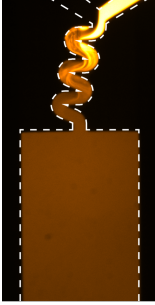
Terminologies	Electrical System	Fluidic Analogs
Electric/Hydraulic Resistance	$R = \frac{\sigma^{-1}L}{\pi a^2}$	$R_H = \frac{8\mu L}{\pi a^4}$
Potential/Pressure Difference	$\Delta V = IR$	$\Delta p = QR_H$
Ohm's/Darcy's Law	$\mathbf{j} = \sigma \mathbf{E}$	$\mathbf{u}_{avg} = \frac{-k}{\mu} \nabla p$
Kirchhoff's Law	$\sum_{k=1}^N I_k = 0$	$\sum_{k=1}^N Q_k = 0$

Table 2.1: Comparison of terminologies used in electrical system and their fluid analogs.

The analogy is particularly useful in building models for predicting flow in mixer designs, such as flow focusing [115, 57, 58].

### 2.7.2 Terminology used to describe flow patterns in microfluidics literature

Table 2.2: Flow patterns in microchannel

Flow Types	Definition	Images
Laminar Flow	Flows with inherent stability, where fluid moves in orderly sheets or lamina	
Transitional Flow	Flow with inherent instability, transitioning between laminar and turbulent flow.	
Recirculatory Flow	Flow with regions where velocity is in the opposite direction of the main flow.	
Chaotic Flow	Flow where streamlines separate exponentially as a function of time.	

# CHAPTER 3

## FABRICATION AND CHARACTERIZATION OF IR COMPATIBLE MICROFLUIDIC MIXER

### 3.1 Overview

So far, we've established the theoretical foundation for studying fluid flow in microchannels. In this chapter, we shift our focus to the practical aspects of microfluidic mixer fabrication. The fabrication process encompasses various stages, from mixer design to photolithography and finally bonding.

Throughout this chapter, we will spotlight key challenges and considerations related to fabrication, such as device reproducibility and bonding issues. We will also delve into strategies for overcoming these challenges, offering valuable insights into successful fabrication practices. By the end of this chapter, readers will have gained a comprehensive understanding of the fabrication techniques, and design considerations involved in creating IR compatible microfluidic mixer. This knowledge will serve as a foundation for subsequent chapters, where the focus will shift towards experimental validation, characterization, and optimization of the fabricated microfluidic mixer.

### 3.2 Microfluidic mixer

Microfluidic mixers can broadly be divided into two types:

- **Passive Mixers:** Passive microfluidic mixers operate without the need for external power or active control mechanisms. They rely on secondary flow and chaotic advection, which can be generated by modifying the geometry of the microchannel, such as using a twisted geometry or bas-relief structures on the channel floor. In this thesis, we focus on a specific passive mixer design called the zigzag, as depicted in Figure 3.3.

Zigzag mixers have gained significant attention in microfluidics due to their ability to promote efficient mixing within a compact design. The zigzag geometry induces repeated folding and stretching of fluid streams, resulting in enhanced interfacial contact and diffusion. By incorporating multiple loops and bends in the channel design, zigzag mixers generate secondary flows and induce chaotic advection, effectively breaking down concentration gradients and facilitating rapid mixing [4].

- **Active Mixers:** Unlike passive mixers, active microfluidic mixers incorporate external power sources or control mechanisms to drive and manipulate fluid flow. These mixers offer greater flexibility and control over the mixing process but are challenging to fabricate due to integration of external component such as micro pumps, valves, sensors, and actuators within the micro channel. This thesis will not delve into the discussion of active microfluidic mixers due to their inherent complexity. However, an excellent review on active microfluidic mixers is available for those interested in exploring this topic further [116, 117].

### **3.3 Fabrication of IR compatible microfluidic mixer**

The fabrication process for the microfluidic device consists of several steps. It begins with designing the microfluidic channel using computer-aided design (CAD) software. The designed channel is then transferred onto a CaF<sub>2</sub> window through the process of photolithography. The next step involves bonding the patterned CaF<sub>2</sub> window with a drilled CaF<sub>2</sub> substrate to enclose the microfluidic channel. This bonding process ensures the integrity and functionality of the device. Finally, the bonded assembly is integrated into a flow cell, allowing for the controlled flow and manipulation of fluids within the microfluidic channel. The initial prototype is fabricated on a 1 mm thick and 40 mm diameter IR-transparent CaF<sub>2</sub> window. The design details are illustrated in Figure 3.1.

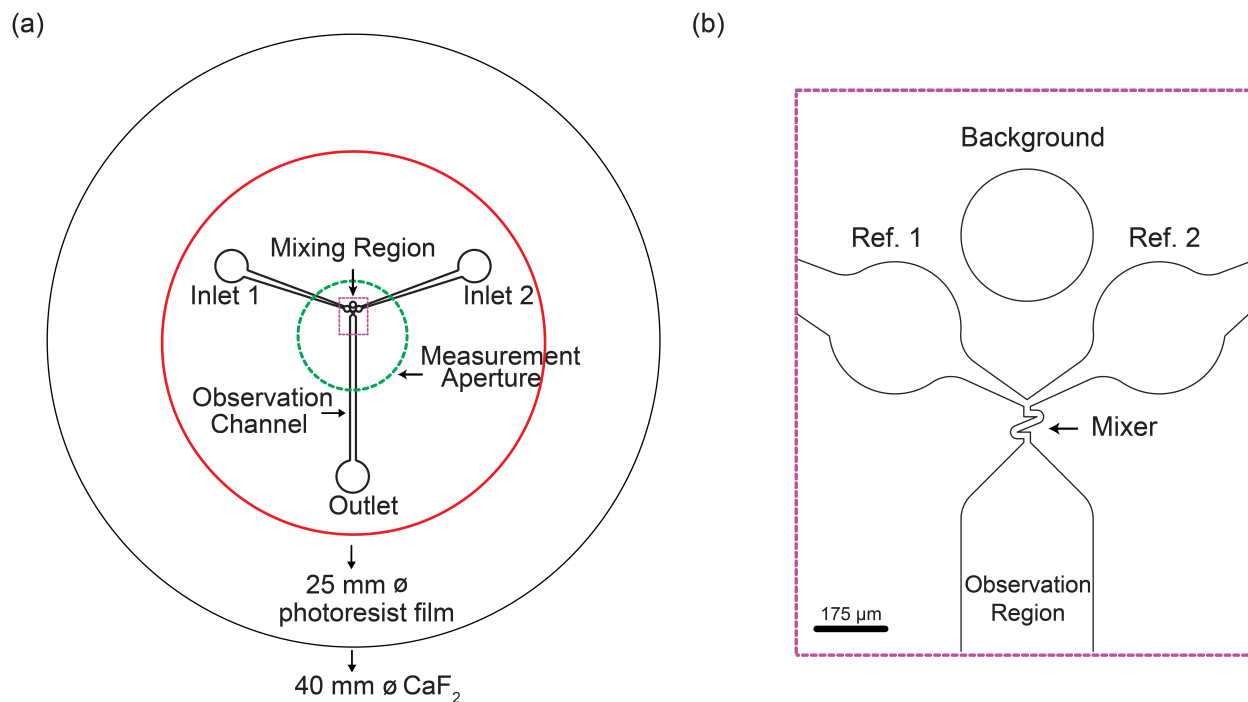


Figure 3.1: Design details on a 40 mm  $\varnothing$  CaF<sub>2</sub> window. (a) A 25 mm  $\varnothing$  photo resist film of uniform thickness ( 30  $\mu\text{m}$ ) coats the window, as depicted by red circle, onto which the channels are etched. Fluid is introduced through two inlet ports located at the top of the device, flows through the mixing region, and exits via an outlet port at the bottom. (b) Design of mixing region. A 350  $\mu\text{m}$  diameter sampling region is incorporated in the inlet channels that transmits the entire focused IR beam and is used to acquire reference IR spectra of the inlet solutions and an air background. With in the mixer, the two inlets merge into a 20  $\mu\text{m}$  channel at the beginning of the mixing region and flare out after the mixing region into a 350  $\mu\text{m}$  wide observation channel to accommodate measurement with IR beam.

### 3.3.1 Mixer design

Achieving effective mixing in microchannels under laminar flow conditions poses a challenge. One successful approach to mixing under laminar flow involves implementing a herringbone pattern with diagonal grooves on the channel floor, as discussed in Chapter 2. This design promotes the repeated stretching and folding of fluid layers, resulting in chaotic particle trajectories. This, in turn, reduces the diffusion distance, thereby enhancing mixing. However, the staggered herringbone mixer faces challenges in achieving rapid mixing, with mixing

times in the order of hundreds of milliseconds, similar to existing IR stopped flow instruments. Additionally, the fabrication process for the staggered herringbone mixer is complex, involving multiple lithography steps and potential additional challenges. Other 3D mixer designs, such as embedded barriers, intersecting channels, and convergent-divergent channels, also present fabrication difficulties, particularly when working with a non-conventional  $\text{CaF}_2$  substrate.

To achieve sub-microsecond mixing, a short and simple zigzag mixer design is considered optimal. Computational fluid dynamics (CFD) simulations have played a significant role in this optimization process. Previous studies have shown that a sharper turning angle in the zigzag pattern improves mixing efficiency [3]. Additionally, the ratio between the turning length and the channel width has been identified as another important factor influencing the mixing performance [106]. A PDMS-based mixer with a maximum turning angle of  $30^\circ$  has been successfully fabricated [2]. However, the need for a relatively high minimum flow rate of 1 mL/min to achieve homogeneous mixing poses challenges, such as potential leakage and device failure.

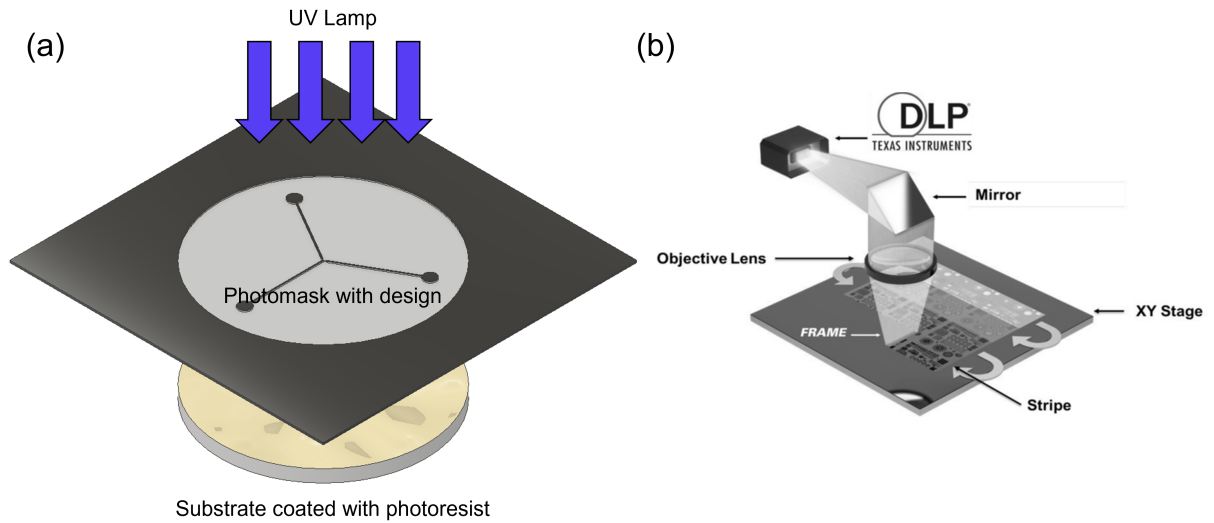


Figure 3.2: Comparison of traditional masked lithography (a) and modern maskless lithography (b), adapted from Ref [5] (Copyright 2016, with permission from SPIE digital library). In traditional photolithography, a UV lamp exposes the photoresist through a mask pattern, enabling pattern transfer onto the substrate. While traditional lithography offers well-established processes and large-scale production, it is limited by the reliance on physical masks. These masks require separate fabrication and precise alignment during the lithographic process, lowering resolution, adding complexity and increasing costs. In contrast, maskless photolithography utilizes digital light projection (DLP) with suitable laser systems to directly expose the photoresist, eliminating the need for physical masks. This approach improves resolution by two orders of magnitude compared to conventional method. Other advantage is its flexibility, as design modifications can be quickly implemented by updating the CAD layout. This enables efficient prototyping and rapid iteration of designs, making it ideal for research and development purposes.

We present a fabrication approach, utilizing a maskless lithography, which offers superior resolution compared to traditional methods, see Figure 3.2. This allowed us to directly pattern on  $\text{CaF}_2$ , eliminating the need for the additional soft-lithography step usually involved when working with PDMS. Consequently, we were able to fabricate zigzags with turns as low as  $10^\circ$ . However, there exists a trade-off between the sharp turning angle and the strength of the mixer wall. To strike a balance, a compromise of  $23^\circ$  was determined, providing a sufficiently strong channel wall while enabling mixing at a flow rate of approximately 0.7

mL/min. Although this flow rate represents an improvement compared to reported values in the literature, it is still high, necessitating several milliliters of solution. This can be problematic when working with expensive samples, and there is a risk of leakage due to high pressure when operating above 0.5 mL/min. Given these considerations, we are actively pursuing the development of diverse iterations of the zigzag mixer. This thesis will delve into three distinct mixer designs, each depicted in Figure 3.3, as we strive to refine the balance between mixing efficiency, structural integrity, and flow rate requirements.

These designs include: a one-turn design known as "inch-worm," a two-turn design referred to as "serpentine," and a three-turn design. By incorporating additional turns in the mixer, homogeneous mixing is achieved at lower flow rates, albeit at the expense of reduced time resolution. To strike a balance between improved mixing efficiency and acceptable time resolution, we opted for no more than three turns in our selection. All mixers consist of a "Y" junction formed by a 20  $\mu\text{m}$  wide and 33  $\mu\text{m}$  deep channel, followed by either a 130  $\mu\text{m}$  long inchworm or a 210  $\mu\text{m}$  long serpentine or 220  $\mu\text{m}$  long three-turn mixing region.

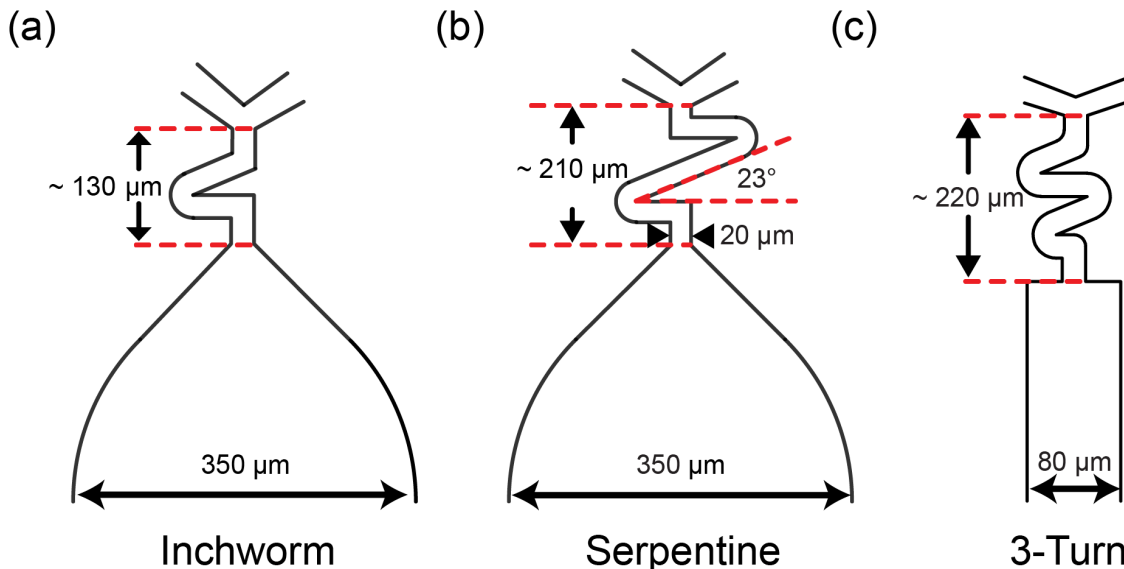


Figure 3.3: Illustration of the inchworm, serpentine and 3-turn mixer designs.

The inchworm and serpentine mixers expand into a 350  $\mu\text{m}$  wide observation channel to



accommodate measurements using a broad IR beam generated by a glowbar source, whose characterization is provided in the next section. As discussed in Chapter 2, the flaring design of the mixers ensures an even distribution of force across the channel walls, promoting steady flow streamlines exiting out of the mixer. Moreover, this design reduces the volume of solution at the first measurement point compared to a flat exit, leading to improved time resolution and minimizing dead volume at the corner.

The three-turn mixer is purposefully designed to operate at lower flow rates and is optimized for use with a tightly focused laser-based source. By incorporating three sharp turns within the mixer, secondary eddies are enhanced, resulting in effective mixing at a flow rate above 0.4 mL/min. This represents a reduction of around 50% compared to the inchworm mixer. The observation channel width remains at 80  $\mu\text{m}$ , and flaring is not emphasized as it is not significantly larger than the mixer width.

### *3.3.2 Observation channel design*

The optimization of the observation channel's design is paramount for acquiring kinetic data of the highest quality. This is especially critical in the realm of time-resolved spectroscopy within continuous-flow mixers where the measurement positions are used to determine the time delays. The design is primarily driven by the goals of enhancing time resolution and maximizing the window of observation. By achieving a high time resolution, the device enables precise measurements of rapid kinetic events, providing detailed information about dynamic processes. Simultaneously, extending the window of observation allows for a wider time range to measure the relevant phenomena, ensuring comprehensive data collection.

The time resolution of a micromixer establishes the minimum time interval between the initiation of mixing and the first kinetic measurement. In stopped-flow techniques, the term "dead time" is commonly used to characterize time resolution. Dead time refers to the duration it takes to thoroughly mix the two target solutions and transport the blended

solution to the observation cell, including the time needed to stop the flow. In the context of stopped-flow infrared spectroscopy, the effective time resolution can be limited by the rise time of the employed IR detector, potentially leading to the experimental dead time exceeding that of the stopped-flow instrument itself. Due to variations in determining the dead time for stopped-flow in the literature, we avoid using this terminology for our rapid mixers [118, 119, 120, 105].

Instead, we define the time resolution as  $\Delta\tau_0$ , using the following expression:

$$\Delta\tau_0 = \tau_{\text{mix}} + \tau_{\text{obs}} + \tau_{\text{beam}} \quad (3.1)$$

In Equation 3.1,  $\tau_{\text{mix}}$  represents the mixing time, indicating the duration for the two liquids to traverse the turns of the mixer together. This can be approximated as  $\tau_{\text{mix}} = \frac{V_{\text{mixer}}}{Q}$ , where  $V_{\text{mixer}}$  signifies the volume of the fluid in the mixer, and  $Q$  signifies the flow rate (See Figure 3.4 for visual representation).

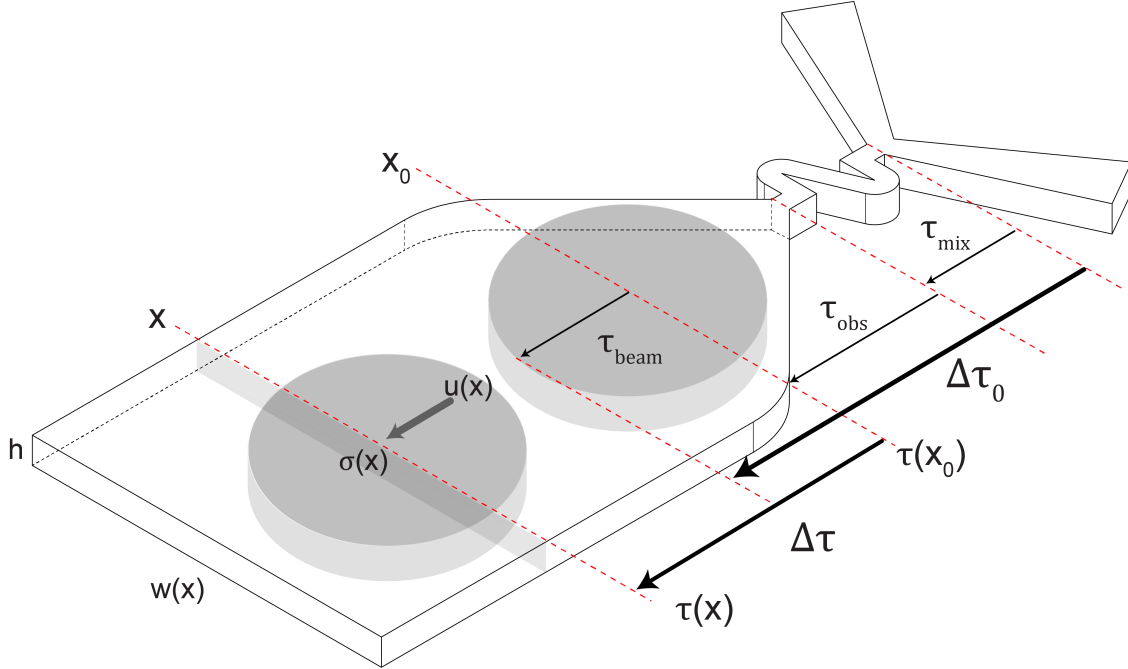


Figure 3.4: Visualization of the observation channel design aimed at assessing and enhancing time resolution. The time resolution ( $\Delta\tau_0$ ) of the measurement encompasses the mixing time ( $\tau_{\text{mix}}$ ), the time to reach the initial observation point ( $\tau_{\text{obs}}$ ), and the temporal variation of the IR probe ( $\tau_{\text{beam}}$ ). The time delay ( $\Delta\tau$ ) corresponds to the interval between consecutive measurements.

On the other hand,  $\tau_{\text{obs}}$  denotes the time needed for the solution to travel from the end of the mixer to the center of the first observation point. This quantity is approximated as  $\tau_{\text{obs}} = \frac{V_{\text{obs}}}{Q}$ , where  $V_{\text{obs}}$  represents the volume of fluid from mixer exit up to the first measurement point. These volumes are directly derived from the CAD file and provide an accurate estimate of the real mixer due to the exceptional precision of the fabrication process.

For an inchworm mixer flowing at a total rate of 0.7 mL/min, the values of  $\tau_{\text{mix}}$  and  $\tau_{\text{obs}}$  amount to 7  $\mu\text{s}$  and 150  $\mu\text{s}$  respectively. The substantial difference between these times arises from the necessity for a broader observation channel to accommodate measurements using the wide infrared (IR) light emitted by a glow bar source. A characterization of the beam size from a Bruker FTIR instrument is depicted in Figure 3.5.

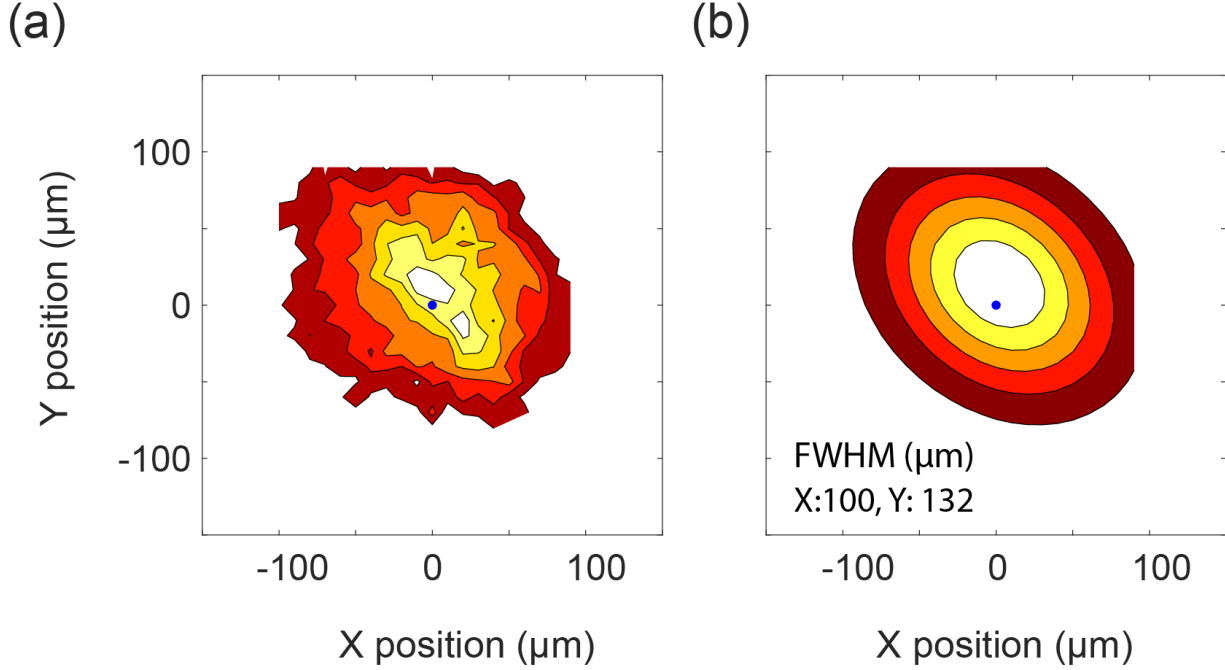


Figure 3.5: Microscope Point Spread Function (PSF) of a glow bar source from FTIR in transmission mode, captured at the focus plane. Contour plots were generated by scanning a  $5 \mu m$  pinhole across the focus plane's raw data (a) and subsequently fitted with a Gaussian fit (b) to determine the FWHM. The observed asymmetry in the beam emphasizes that the beam collimation of the glow bar source is not optimally aligned.

The third term,  $\tau_{\text{beam}}$ , characterizes the temporal variation across the measurement beam's spot size. As  $\tau_{\text{obs}}$  already considers half of the beam, we employ the half-width half-maximum (HWHM), which is half of the full-width half-maximum (FWHM). The quantity  $\tau_{\text{beam}}$  is calculated using the following formula:

$$\tau_{\text{beam}} = \frac{1}{2} \frac{hw\Delta r}{\sqrt{8 \ln 2} Q} \quad (3.2)$$

Here,  $h$  and  $w$  represent the height and width of the observation region respectively. The quantity  $\Delta r$  represents the FWHM, which can be experimentally determined by fitting the intensity of transmitted IR obtained through a pinhole using raster scan mode, as shown in Figure 3.5. The corresponding value of  $\Delta r$  for a glow bar at the sample's focus plane is  $100 \mu m$  in the X direction and  $132 \mu m$  in the Y direction. Considering the channel depth, which

is  $30 \mu\text{m}$ , the effective  $\Delta r$  is about 1.5 times larger in reality due to variations in the z-profile. Hence, we employ a value of  $200 \mu\text{m}$  for our calculations. For comparison, the FWHM for an IR beam from a well-collimated laser source is approximately  $12 \mu\text{m}$ , representing an order of magnitude improvement compared to the glow bar source. The best time resolution achievable for each mixer designs in combination with different IR beam sizes is summarized in Table 3.1.

Mixer Design	$\tau_{\text{mix}} (\mu\text{s})$	$\tau_{\text{obs}} (\mu\text{s})$	IR Beam FWHM ( $\mu\text{m}$ )	$\tau_{\text{beam}} (\mu\text{s})$	$\Delta\tau_0 (\mu\text{s})$
Inchworm	7	150	200	80	237
Serpentine	12	150	200	80	242
3-turn	15	15	12	1	31

Table 3.1: Summary of time resolution and related parameters for different mixer designs at a flow rate of  $Q = 0.7 \text{ mL/min}$  and a channel height of  $h = 30 \mu\text{m}$ .

To enhance the time resolution for kinetics measurements, in addition to reducing the mixing time, it is important to employ tighter focusing of the IR beam and reduce the observation channel width, preferably approaching the spot size of the focused beam. For the inchworm/serpentine mixers, the time resolution is primarily limited by the speed at which the measurement can be made upon exiting the mixer. In these designs, reducing the observation channel width and optimizing the focusing of the IR beam can significantly enhance the time resolution. In the case of the 3-turn mixer, the time resolution is equally influenced by the mixing time and the measurement process upon exiting the mixer. Thus, efforts should be made to minimize both the mixing time and the measurement time to achieve the best possible time resolution. One way to do that would be to perform experiment at higher flow rates.

Now that we have calculated the time corresponding to the first measurement position, let's delve into the calculation of time delay between successive measurement points. This involves mapping measurement position to time using the fluid velocity within the observation channel. Although the fluid's velocity field through the microchannel can have complex

spatial variations, in calculating the time-delays, we assume that the velocity in the channel at a particular point along the direction of fluid flow,  $u(x)$ , is governed only by the cross-sectional area through the device  $\sigma(x)$ , see Figure 3.4. The height of our channel  $h$  is constant, but the width of the channel  $w(x)$  can vary with  $x$ , so that  $\sigma(x) = hw(x)$ .

The time after first observation,  $\tau(x)$ , can then be determined from the volume of fluid,  $V(x)$ , in the device between the first measurement point,  $x_0$ , to that point,  $x$ , using the following equations:

$$V(x) = \int_{x_0}^x \sigma(x') dx' \quad (3.3)$$

$$\tau(x) = \frac{V(x)}{Q} \quad (3.4)$$

$$\Delta\tau = \tau(x) - \tau(x_0) \quad (3.5)$$

The value of  $\Delta\tau$  corresponding to distance  $\Delta x$  of 350  $\mu m$  under a flowrate of 0.7 mL/min is 315  $\mu s$ . For a linear channel of length of 7 mm, this result in a measurement time window of 6 milliseconds. To extend the measurement time window, another factor to consider in the observation channel design is the potential extension of the straight observation channel's length. However, this extension is constrained by the need to fit within the 10 mm imaging aperture and the size of the CaF<sub>2</sub> window. Consequently, two distinct designs have been implemented: a lengthy serpentine channel with curved bends (referred to as "alternating"), and a continuous "spiral" channel, as depicted in Figure 3.6. The advantage of the alternating

design lies in its straightforward time delay determination, although the impact of u-turns on the flow dynamics should be taken into account. This concern is less pronounced in the spiral design due to the smoother nature of the turns. At a flow rate of 0.7 mL/min, these designs effectively broaden the observation time window from 6 milliseconds in the straight channel to 45 milliseconds in the alternating and 36 milliseconds spiral designs.

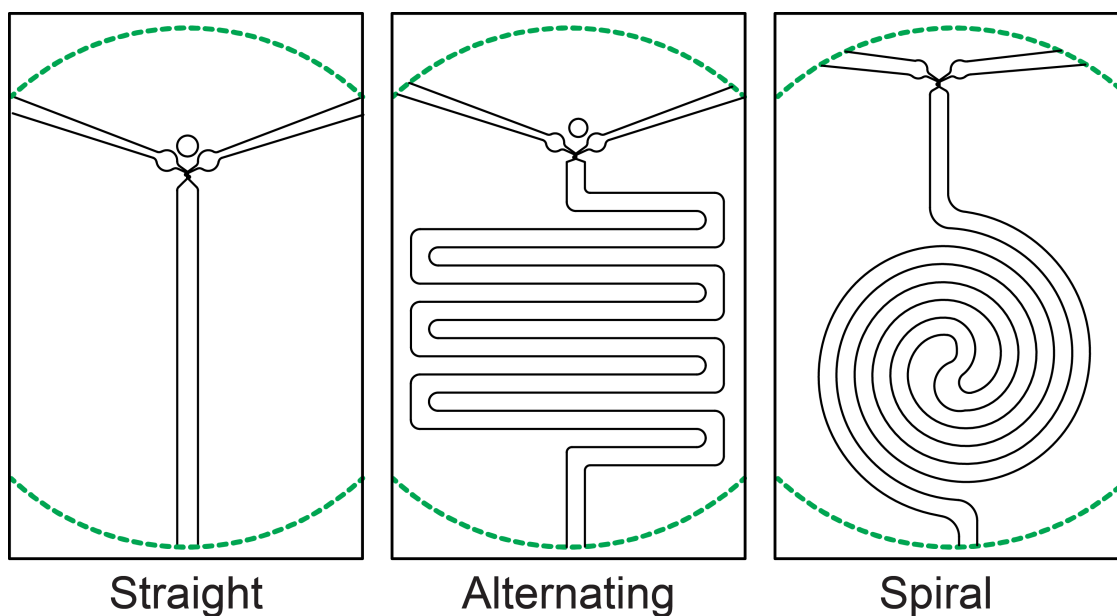


Figure 3.6: Illustration of observation channel designs within the measurement aperture, represented by a green dashed circle. The designs include a linear channel (7 mm long path) with a corresponding time window of 6 ms, an alternating channel (50 mm long path) with a time window of 45 ms, and a spiral channel (40 mm long path) with a time window of 36 ms at a flow rate of 0.7 mL/min.

To further extend the time window of observation to hundreds of milliseconds, several strategies can be employed. For linear observation channels, a gradual widening of the channel width can be implemented, causing time to increase non-linearly with distance from the mixer. An adapted alternating design could be utilized, introducing increased channel width after each turn. Additionally, utilizing a larger  $\text{CaF}_2$  material to fabricate the channel would broaden the imaging window, enabling extended observation channels and thereby expanding the achievable time window.

### 3.4 Photo-Lithography

Photo-lithography is a crucial step in device fabrication, carried out in an International Standards Organization (ISO) Class 5 cleanroom. This process involves using light to transfer a pattern from a photo-mask or a CAD design directly onto a substrate coated with a photosensitive material called a photoresist. There are two main types of photo resists used in photo-lithography: positive photo resist and negative photo resist. Positive photo resist becomes more soluble in developer solution when exposed to light, meaning that the exposed regions are removed during development, leaving behind the unexposed regions as the pattern. Negative photo resists often polymerize upon light exposure, meaning that the unexposed regions are removed during development, leaving behind the exposed regions as the pattern. Both types of photo resists can also be classified as either chemically amplified or non-chemically amplified, depending on whether a chemical reaction occurs during the exposure process to enhance the resolution of the pattern. The process is highly complex and requires careful control of numerous parameters, including the light source, mask design, exposure time, and development conditions. The success of photo-lithography ultimately depends on the ability to create highly precise patterns with feature sizes on the order of nano-meters, which is critical for achieving the desired device performance. The process typically involves the following steps:

- **Cleaning:** The substrate is cleaned to remove any contaminants that could interfere with the patterning process.
- **Vacuum Bake:** The substrate is placed in a vacuum to remove moisture and solvent from the surface, ensuring optimal adhesion and uniformity of the photo resist layer.
- **Coating:** A thin layer of photo resist is spun onto the substrate, creating a uniform coating.



- Soft bake: The photo resist is heated to a low temperature to remove any solvent and promote adhesion to the substrate.
- Alignment and exposure: The photomask is accurately positioned relative to the substrate, and then light, typically from a UV lamp or UV laser, is used to expose the photo resist.
- Post-exposure bake (PEB): A thermal treatment is applied to the photo resist-coated substrate after exposure to promote the desired chemical reactions.
- Development: The exposed photo resist is selectively removed by a developer solution, revealing the patterned substrate.
- Hard bake: The patterned substrate is heated to a higher temperature to increase the strength and stability of the photo resist pattern. This step is optional.

### 3.5 Detailed fabrication steps for AZ40XT photoresist

AZ40-XT, manufactured by Microchemical, is a chemically amplified ultrathick positive photoresist known for its remarkable sensitivity to 375 nm light. The resist has a thickness range of 15 - 100  $\mu\text{m}$ . It is composed of a phenolic novolak resin with diazonaphthoquinone sulphonate (DNQ) serving as a photo initiator. When DNQ is exposed to UV light, it undergoes a conversion into an indene carboxylic acid. This conversion increases the solubility of the phenolic resin by several orders of magnitude. The exposed area can then be selectively removed using a suitable alkaline developer. The photolithography process involved is straightforward and yields exceptional resolution in the resulting patterns. Furthermore, AZ40-XT exhibits excellent adhesion to  $\text{CaF}_2$  and solubility in organic solvents, which allows for the reusability of the  $\text{CaF}_2$  window.

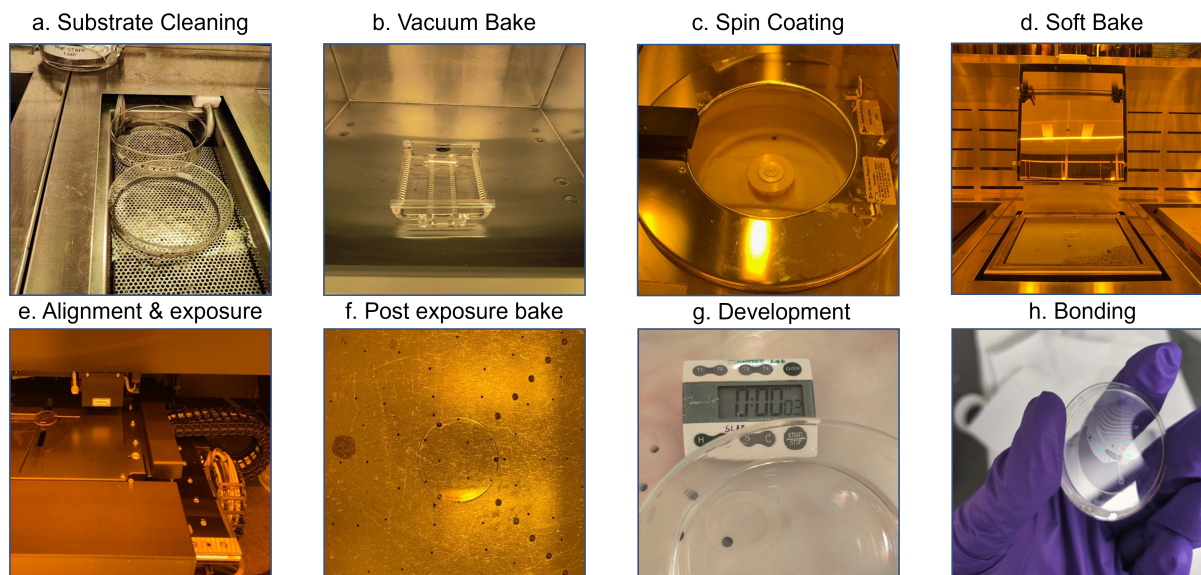


Figure 3.7: Fabrication steps for AZ40XT photoresist. (a) The  $\text{CaF}_2$  substrates are placed inside a flat-bottom glass container containing organic solvents and cleaned using ultrasonic bath. (b) The residual solvent is removed by baking in a vacuum at  $110^\circ\text{C}$ . (c) Spin coating to achieve a uniform photoresist layer on the substrate. (d) The residual solvent in the resist is removed by heating on a hot plate in a process known as soft bake. (e) The photoresist is exposed to a  $375\text{ nm}$  laser to pattern the micro channel design. (f) Post exposure baked is performed to complete the photoreaction and make the resist developable by heating in a hot plate. (g) The exposed resist is etched by dipping in a MIF 300 developer solution. (h) Microchannel is closed by bonding with drilled  $\text{CaF}_2$  window.

The fabrication of the micro channel begins with the cleaning of the  $\text{CaF}_2$  window with acetone and methanol to remove organic impurities followed by drying in a  $110^\circ\text{C}$  vacuum oven (Figure 3.7 a,b). The clean window is placed on a spinner chuck of PWM32 Controller Spinner (Headway Research Inc., USA) for spin coating photo resist (Figure 3.7 c). About  $3\text{ mL}$  of the photo resist is poured onto the substrate directly from an amber storage jar, since its high viscosity precluded pipetting. The spin coating follows a series of steps. To allow the photo resist to spread evenly across the entire surface of the substrate, the spin speed is started at  $500\text{ rpm}$  and held constant for  $10\text{ s}$ . The spin speed is then ramped up to  $2000\text{ rpm}$  with an acceleration of  $1000\text{ rpm/s}$  and maintained for a duration of  $30\text{ seconds}$  yielded an average thickness of the photoresist film of  $34\text{ }\mu\text{m}$ . A detailed discussion on the

film thickness characterization is in Section 3.7.

When spin coating AZ40-XT on  $\text{CaF}_2$  substrates, a tiny bubble is consistently observed in the photoresist film (See Figure 3.11 a, red circle). This occurrence can be attributed to various factors, including the pouring technique of the resist, the age of the resist, and the surface quality of the substrate. However, the most significant factor appears to be the degradation of the surface quality as its always evident on highly reused windows. If the bubble is located near the center, it poses a problem because the channels are etched around that area. We have found that initiating the spin process directly at 2000 rpm eliminates the bubble from the center to the sides. In addition to achieving uniform thickness, spin coating also plays a crucial role in removing the solvent from the photoresist. The spinning action causes the solvent to evaporate, leaving behind a dried photoresist film. The residual solvent in the photoresist film is removed through a soft bake process, which involves placing the substrate on a hotplate set to  $125^\circ\text{C}$  for a total duration of seven minutes (refer to Figure 3.7 d). To prevent the formation of bubbles that may arise from the rapid evaporation of solvent directly from the substrate surface, a hot plate with lift pins is utilized. The lift pins are adjusted to different heights throughout the process: initially set at 0.25 in., then lowered to 0.1 in. after two minutes, further lowered to 0.05 in. after another two minutes, and finally brought into full contact with the substrate for the remaining one minute. This gradual contact minimizes the chances of bubble formation and ensures effective solvent removal.

After soft baking, the photo resist film is exposed by direct writing of the structure with a Heidelberg Mask Less Aligner (MLA)-150 using a 375 nm laser (Figure 3.7 e). Two exposure files were prepared in AutoCAD software. The first exposure file consisted of micro channel design while the second one consisted of two concentric circles 25 mm, and 40 mm in diameter. The second exposure removes “edge bead” elevation around the substrate edge resulting from the spin coating of high viscosity photo resist. This is crucial so that a uniform layer of 25 mm diameter photo resist film is deposited on the  $\text{CaF}_2$  substrate.

Exposure dose in photolithography is the amount of light energy needed to expose a photoresist, typically measured in millijoule (mJ) per square centimeter. It determines the quality and resolution of the pattern. Insufficient dose leads to incomplete patterns, while excessive dose causes difficulties in development. The key factors for determining optimal dose are the reflectivity of the substrate, the type of photoreaction occurring in the photoresist, and the thickness of the photoresist film.

The reflectivity of a substrate refers to the amount of incident light that is reflected from its surface.  $\text{CaF}_2$  has a reflectivity of approximately 10%, whereas Si wafers have a reflectivity of around 30%. Due to the lower reflectivity of  $\text{CaF}_2$ , it requires a larger exposure dose compared to Si wafers. For AZ 40 XT, the photoreaction follows a one-photon process, meaning that the desired reaction is initiated by the absorption of a single photon with sufficient energy. The optimal exposure dose can be determined experimentally. In a specific case, a series of 375 nm laser exposures ranging from  $100 \text{ mJ/cm}^2$  to  $800 \text{ mJ/cm}^2$  (with a step of  $50 \text{ mJ/cm}^2$ ) was performed to fabricate a  $100 \text{ }\mu\text{m} \times 100 \text{ }\mu\text{m}$  square. Doses exceeding  $500 \text{ mJ/cm}^2$  led to the fabrication of high-aspect ratio microstructures. To minimize the risk of potential thermal damage caused by high light intensity,  $500 \text{ mJ/cm}^2$  was identified as the optimal exposure dose. The total exposure time depends on the speed at which this dose can be uniformly applied across the substrate using the motorized stage. In our specific design, the total exposure time is approximately seven minutes.

Following the photoactivation, a post-exposure bake (PEB) is performed by placing the substrate on a  $110 \text{ }^\circ\text{C}$  hotplate for 50-60 seconds (Figure 3.7 f). During this step, nitrogen gas is generated as a byproduct, which may result in bubble formation in the exposed area of the photoresist. To minimize the likelihood of bubbles, it is recommended to promptly remove the substrate from the hotplate after one minute.

However, for thicker substrates, it has been observed that using a higher temperature of  $115 \text{ }^\circ\text{C}$  produces better results compared to the standard  $110 \text{ }^\circ\text{C}$  temperature. Thicker sub-

strates typically have lower thermal conductivity compared to thinner ones, leading to slower and less efficient heat transfer during the PEB step. By increasing the temperature to 115 °C, the thermal energy is more effectively delivered to the thicker substrate, compensating for its lower thermal conductivity and improving the overall process.

In the final step, the exposed photoresist is removed by submerging the substrate in a fresh AZ MIF 300 alkaline developer solution. This is done for a duration of three minutes, with gentle hand agitation by hand (Figure 3.7 g). It is important to refrain from using an ultrasonic bath for agitation, as it can damage the mixer walls. Without agitation, the development process becomes uneven and takes longer to complete.

## 3.6 Bonding

The bonding step is the most challenging and least robust in the current device fabrication process. Novlak-based photoresists like AZ40-XT exhibit excellent adhesion properties on CaF<sub>2</sub> surfaces, eliminating the need for any surface treatment prior to the bonding process [121]. It is carried out in cleanroom environment to minimize the introduction of dust. The process involves compressing the "soft" photoresist between brittle CaF<sub>2</sub> using a press. By subjecting the AZ40-XT photoresist to elevated temperature and applying pressure, it can be effectively compressed between the two windows, resulting in a strong bonding that is capable of withstanding the high pressure drop generated during solution flow within the microchannel.

### *3.6.1 Anatomy of the hydraulic heat press*

During the bonding process, it is importance to closely monitor and adjust several parameters, including temperature, pressure, and alignment, to achieve the desired bonding quality. The Dulytex press, as depicted in Figure 3.8 features two 2.5 in × 6 in temperature-regulated aluminum plates. The top plate remains fixed in its position, while the bottom plate is sit-

uated on the large piston of a hydraulic bottle jack. The hydraulic bottle jack incorporates a small piston connected to a lever mechanism. By pumping the lever, the small piston moves vertically, causing the large piston to move upwards. Consequently, the bottom plate is driven towards the top plate. The following modifications enable effective monitoring and control of these parameters:

- **Addition of a pressure gauge:** A pressure gauge has been installed on the hydraulic bottle jack to accurately monitor the pressure between the aluminum plates during the bonding process.
- **Introduction of metal and/or silicone rubber shims:** Shims of varying thicknesses, ranging from 1 to 4 mm, have been incorporated. These shims allow for precise control of the height between the two metal plates, ensuring optimal bonding with  $\text{CaF}_2$  substrates of different thicknesses.
- **Utilization of Teflon or copper shim stock:** To achieve precise height adjustment and minimize the risk of substrate cracking, Teflon or copper shim stocks with thicknesses ranging from 100 to 200  $\mu\text{m}$  have been employed.

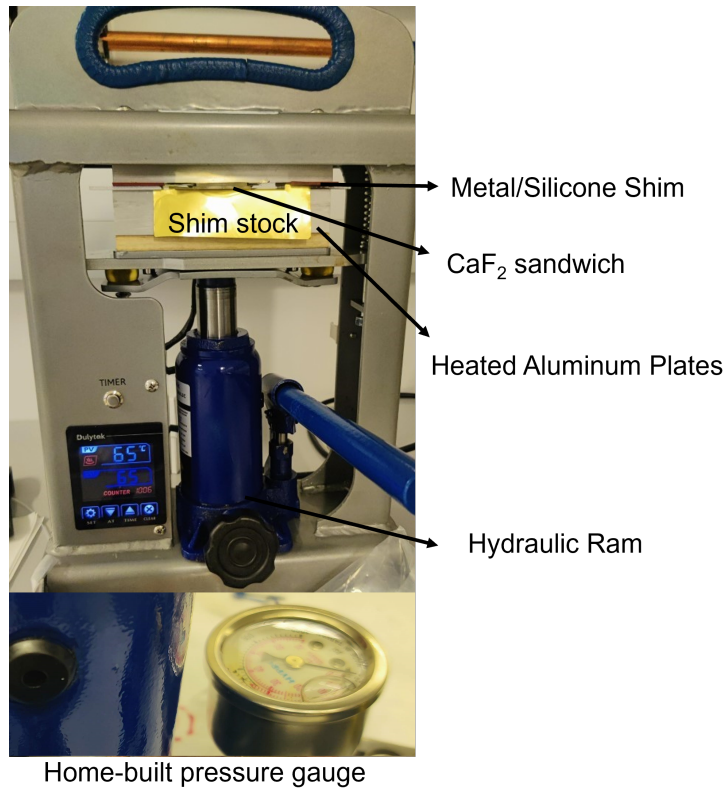


Figure 3.8: Modified dulytek press with enhancements for bonding reproducibility.

Before the bonding process, the heat press is set to the desired temperature and given sufficient time to reach thermal equilibrium. This equilibration period takes approximately 10 minutes. Next, the drilled holes (1.5 mm  $\varnothing$ ) in the  $\text{CaF}_2$  window, are carefully aligned with the channel inlets and outlet holes by hand. To simplify the alignment process, the microchannel ports in the photoresist film are intentionally designed with a slightly larger diameter of 2.2 mm. This provides a margin of error and allows for easier alignment of the drilled holes in the  $\text{CaF}_2$  window with the corresponding inlet and outlet ports. Afterward, the sandwiched  $\text{CaF}_2$  substrates are carefully positioned on the bottom aluminum plate using a substrate holder. It is crucial to exercise caution during this step to prevent any secondary burn and to ensure proper alignment of the drilled holes with the corresponding inlet and outlet ports.

The bonding process is initiated by operating the lever to move the bottom plate towards

the top plate. However, due to the attachment of the bottom plate to a pair of springs, there is a wobbly motion during this movement. As a result, the plane of the top and bottom plates may not remain parallel, leading to uneven pressure distribution across the bonding interface and increasing the risk of brittle  $\text{CaF}_2$  windows breaking. To address this issue and ensure a more uniform pressure distribution, we incorporate thick metal shim shocks on each side of the aluminum plates. These metal shim shocks help create an even spacing between the plates when they come into full contact, compensating for any misalignment caused by the wobbly motion.

These metal shim shocks serve to create a consistent spacing equivalent to the thickness of the metal when the two plates of the press come into full contact. The thickness of the metal shim shocks is adjusted based on the thickness of the sandwiched  $\text{CaF}_2$  window. For instance, for bonding a pair of 1 mm thick  $\text{CaF}_2$  windows, a 2 mm thick metal shim shocks is employed on each side of the aluminum plates. To further minimize the risk of breakage, we implement thin 100  $\mu\text{m}$  Teflon sheets as cushions for the windows. These Teflon sheets act as an additional protective layer during the bonding process. However, for thicker substrates, we replace the Teflon sheets with equivalent-sized metal shim stock. This substitution offers improved thermal conductivity, ensuring efficient heat transfer during the bonding process.

The bonding process for varying thickness of  $\text{CaF}_2$  windows involves specific temperature, pressure, and sealing techniques to prevent the formation of air bubbles and cracking. Here is a step-by-step description:

1. **Temperature:** The optimal temperature range for bonding  $\text{CaF}_2$  windows is 65-75  $^\circ\text{C}$ . For a pair of 1 mm thick  $\text{CaF}_2$  windows, it is recommended to use the lower end of this temperature range. This ensures that the bonding process is conducted without damage to mixer in the photo resist film. Conversely, for a pair of 2 mm thick  $\text{CaF}_2$  windows, the higher end of the temperature range should be used. This adjustment accounts for lower thermal conductivity of the thicker substrates and ensures effective



bonding.

2. **Pressure:** Pressure plays a crucial role in the bonding process. Optimal results are achieved within a pressure range of 400-600 psi. Initially, when the  $\text{CaF}_2$  is sandwiched between the metal plates, the pressure reading is around 150 psi. It is important to gradually increase the pressure to distribute the stress evenly across the bonding interface. For thinner windows, a pressure of 400 psi is recommended, and it should be maintained for a duration of 5-10 seconds. In the case of thicker windows, a higher pressure of 600 psi is advised, and the hold time should be extended to 15-20 seconds. It is essential to avoid applying excessive pressure too quickly, as it can subject the windows to excessive stress, thereby increasing the risk of cracks or other structural damage.
3. **Sandwiched  $\text{CaF}_2$  Placement:** If the sandwiched  $\text{CaF}_2$  is placed at the center of the plate and pressed, any residual air bubbles will be randomly dispersed throughout the micro channel. This is problematic because once the fluid flows, it spreads throughout the bubble which disintegrates the assembly. But if the windows are placed such that only one half of the cell is sealed, then the trapped air are pushed to the non-bonded side. By implementing the half-sealing technique and utilizing rotation and compression cycles, the risk of air bubble formation within the micro channel is significantly reduced. Multiple cycles of rotation and compression might be necessary for thicker substrate.
4. **Verification:** Finally, the bonded  $\text{CaF}_2$  cell assembly is inspected for any trapped air, and the microscope is used to check for any damage to the mixer. For reference, below are two visual examples of the bonding process, illustrating both successful and unsuccessful bonding outcomes.

### 3.6.2 Example I: Excellent bonding

Figure 3.9 exemplifies a successful bonding. The figure showcases a pair of 1 mm thick CaF<sub>2</sub> windows, highlighting the positive outcome of the bonding procedure. The caption accompanying the figure provides a clear and self-explanatory description of the depicted results, elucidating the successful nature of the bonding process.

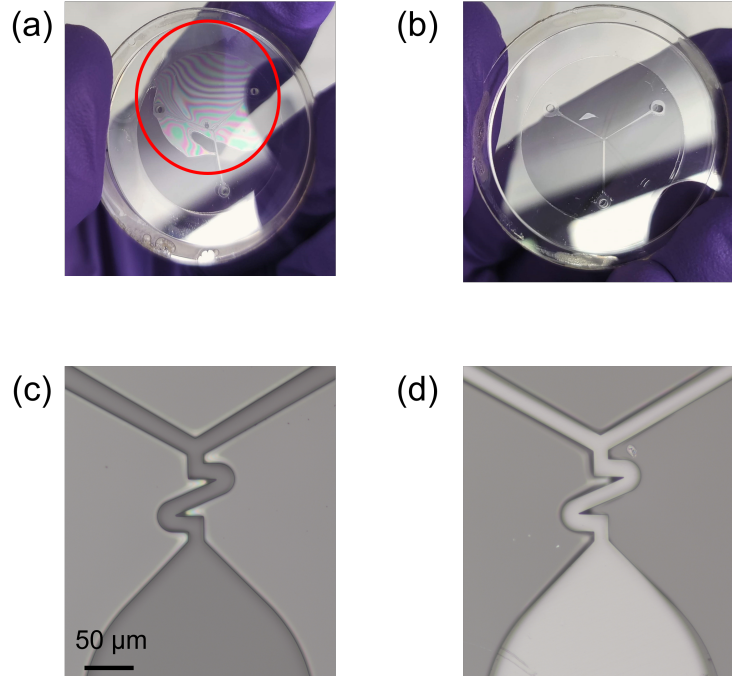


Figure 3.9: Illustration of excellent bonding process. (a) Pair of 1 mm thick CaF<sub>2</sub> assembly after the first sealing step, demonstrating complete bonding at the lower end. The presence of interference fringes (red circle) on the top side, caused by the reflection of light between the surface of the photoresist film and the drilled CaF<sub>2</sub> window, confirms that the surfaces are not fully bonded. (b) Image after the second sealing step, showcasing complete bonding with no trapped air bubbles. (c) Microscope image showcasing the serpentine mixer before the bonding process. (d) The microscope image taken after bonding reveals the intact and undamaged state of the mixer, providing positive confirmation that the bonding process did not result in any damage to the mixer.

### 3.6.3 Example II: Bonding failures

In the pursuit of improving a bonding technique, it is inevitable to encounter failures along the way. Figure 3.10 highlights some of the challenges faced during the bonding process.

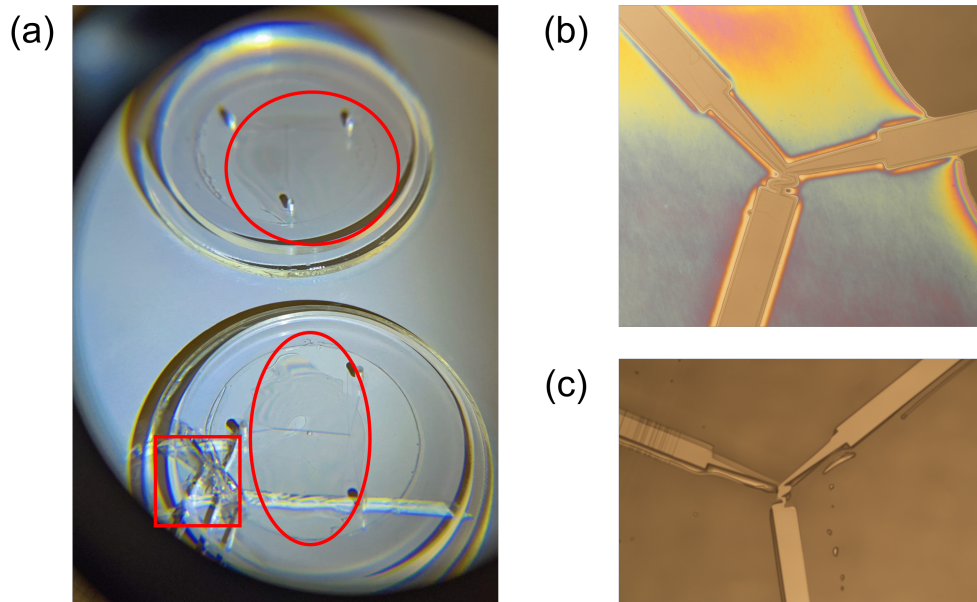


Figure 3.10: Illustration of bonding failures. In (a), two  $\text{CaF}_2$  sandwiches are shown, and the presence of interference fringes on both, as indicated by the red circle, suggests incomplete bonding between the surfaces. One  $\text{CaF}_2$  sandwich had cracks on the drilled window, as indicated by red square, suggesting excessive stress during the bonding. (b) Microscope image revealing complete bonding on one inlet (top right) and incomplete bonding elsewhere, with more prominent fringes visible. (c) Microscope image demonstrating complete bonding, but with mixer deformation.

Below, the most common failures encountered during bonding is described along with ways to address them.

- Substrate Cracking:** Figure 3.10 a illustrates an example of substrate cracking. It can arise from factors such as excessive pressure or rapid pressure increase. As described earlier Dulytex press is not a laboratory-grade instrument, as its aluminum plates are not calibrated to be perfectly horizontal. To address this limitation, a metal shim is employed to minimize the variation in the angle between the plates. However, despite this precaution, one side of the substrate experiences higher pressure, leading to consistent cracking on that particular side. Thinner substrates, with their reduced mechanical strength, are more prone to cracking in such circumstances. Placing a pressure distribution pad, such as, silicone rubber with the metal shim helps distribute the

applied pressure more evenly across the substrate surface, reducing localized stress and minimizing the occurrence of substrate cracking. Lowering the pressure and temperature while extending the bonding time can contribute to resolving the cracking issue. By reducing the applied pressure, the stress exerted on the substrate is decreased, thereby reducing the likelihood of cracking.

- **Air bubble and damage to the mixer:** Figure 3.10 b,c illustrates an example of trapped air and damage to the mixer, respectively. To address this issue, one potential solution is to incorporate a vacuum-assisted bonding method. By creating a vacuum environment, air bubbles can be effectively removed, reducing the risk of damage to the mixer. While it may not be feasible to directly add a vacuum within the Dulytex press mentioned earlier, there are dedicated laboratory instruments available specifically designed for vacuum bonding such as EVG bonding systems. These instruments offer more precise control over the bonding environment, enabling the removal of air bubbles and minimizing the potential for mixer damage. The damage to the mixer can be attributed to multiple cycle of pressing during the bonding process. Each pressing cycle imposes stress on the mixer, and over time, this cumulative stress can lead to physical damage. To mitigate the risk, fine-tune the bonding parameters to achieve optimal bonding with the fewest possible cycles. Additionally, incorporating intermediate steps for inspection and evaluation between pressing cycles can help detect early signs of damage. By closely monitoring the mixer's condition at various stages of the bonding process, any developing issues can be promptly identified and addressed before they escalate.

## 3.7 Micro channel geometry characterization

### 3.7.1 Before bonding

Accurate measurement of microchannel dimensions, including width, depth, and roughness, is crucial for designing and optimizing microfluidic devices. Optical profilometry is a reliable method for measuring these parameters. The Olympus OLS 5000 LEXT 3D Laser Confocal Scanning Microscope is an exceptional instrument for this purpose. This dual confocal microscope utilizes a 405 nm laser and a micro-electromechanical system (MEMS) scanner to achieve a resolution of 10 nm, allowing for precise measurement through surfaces. The microscope acquires multiple confocal images by shifting the z-focus position to estimate the light intensity variation curve (I-Z curve) for each pixel based on the discrete focus position (Z) and detected light intensity (I). By identifying the peak position and peak intensity of each pixel's I-Z curve, the microscope provides 3D information about the sample's surface, and peak positions. Figure 3.11 showcases the height characterization process prior to bonding, employing the LEXT 3D microscope. The process initiates with a low magnification map of the device, typically at 5X, providing an overview. Subsequently, specific regions of interest such as the mixer and film edge undergo high magnification (20X or better) 3D scanning for detailed height measurement.

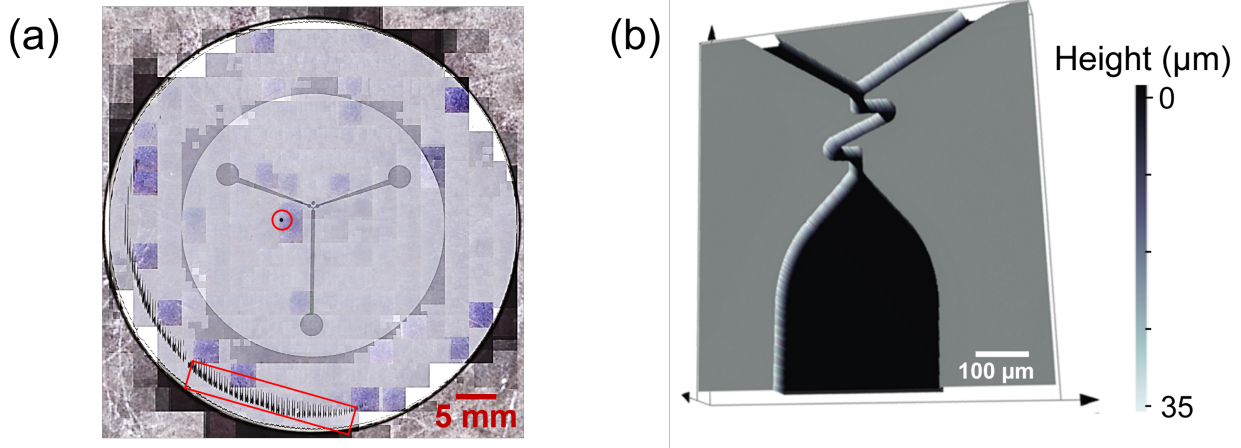


Figure 3.11: Illustrating the height characterization process using 3D optical profilometry. (a) Map image of CaF<sub>2</sub> window after photolithography with AZ 40XT photoresist, individual pixel captured at 5X magnification and stitched together. The pixelation is a result of artifacts incorporated in the stitching algorithm, stemming from auto-focusing. Noteworthy features include a microchannel, a bubble within the photoresist film (highlighted by the red circle), and areas of underdeveloped photoresist (highlighted by the red square). (b) The 3D height map of the serpentine mixer, captured at 20X magnification. The width of the channel walls in the mixer is  $20.0 \pm 0.2 \mu\text{m}$ , which is within 1% of the CAD design. The channel depth is  $34 \pm 0.5 \mu\text{m}$  and the film surface variation is 100 nm, indicating highly uniform deposition of the photoresist film. The almost 90 deg steep channel walls showcase exceptional photolithography.

### 3.7.2 After bonding

The characterization of the compression of the photoresist film resulting from bonding is essential for evaluating the quality and integrity of the bonding process. However, when the film bonds to two windows, optical profilometry is hindered by back reflection from the window surfaces. To address this issue, it is necessary to physically separate the windows while minimizing any potential damage to the film. A simple channel design, such as a microwell, was employed to facilitate this separation process. The bonding of the windows was carried out using the procedure described in Section 3.6. Subsequently, to separate the windows, the side of the window sandwich was gently wedged with the plastic tip of the substrate holder to minimize the risk of breaking the windows. This method ensured the

separation of the windows while preserving the integrity of the film. In Figure 3.12a, a depth profile plot of a 100  $\mu\text{m}$  diameter microwell is shown before and after bonding. The plot illustrates a compression of 5% in the photoresist film resulting from the bonding process.

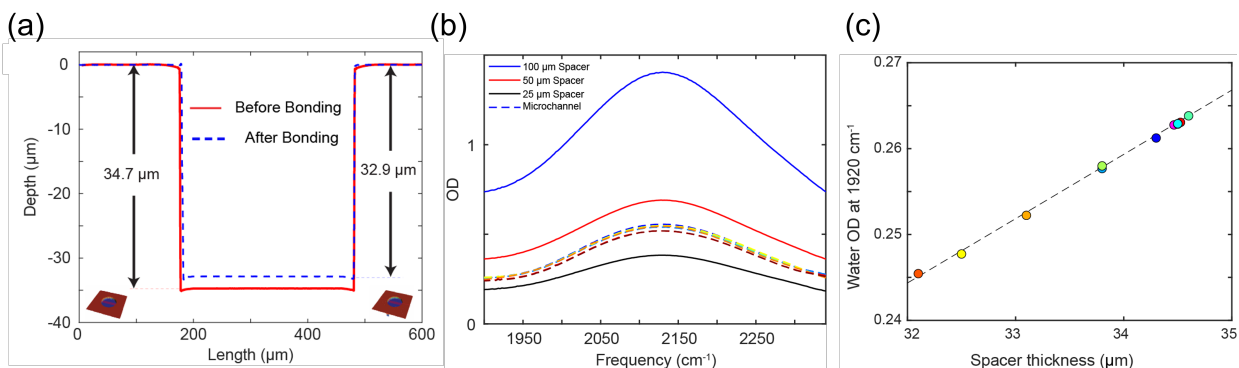


Figure 3.12: (a) Comparison of depth profile before and after bonding using laser confocal profilometry on the same microwell, with corresponding images shown at the bottom. The compression due to bonding is less than 5%. (b) FTIR spectra of water bend libration mode at known spacer thicknesses. The blue, red, and black lines represent spacer thicknesses of 100  $\mu\text{m}$ , 50  $\mu\text{m}$ , and 25  $\mu\text{m}$ , respectively, and the dashed lines represent spectra collected in microchannel devices. (c) The dashed black line represents the calibration curve constructed from taking absorption at 1920  $\text{cm}^{-1}$  from known spacer thicknesses, which was used to derive the microchannel depth, depicted by colored circles.

In addition to profilometry, we employed IR spectroscopy of water to estimate the depth of the micro channel. By measuring the absorption of water at a specific wavelength, we can employ the Beer-Lambert law to determine the path length traveled by the light. We created a calibration curve by measuring the spectra from a known spacer path lengths and used it to estimate the channel depth for different devices. We specifically selected a weak absorption peak at 1920  $\text{cm}^{-1}$ , which is located around the tail of the bend libration combination band, to prevent detector saturation. The spectra and calibration curve are depicted in Figure 3.12b and c, respectively. Based on our measurements, the average microchannel depth was determined to be  $34.1 \pm 0.9 \mu\text{m}$  across twelve devices. This result is consistent with the findings from the profilometry measurement, highlighting the robustness of the lithography and bonding processes in producing reproducible devices.

### 3.7.3 *Lithography for alternative photo resists with enhanced chemical compatibility*

The need for alternative photo resists arises when prototyping or fabricating micro channels involving reactions with organic solvents. While AZ40-XT may excel in prototyping, its limitations in chemical compatibility necessitate the exploration of other options. Fortunately, there are numerous photo resists available that offer improved compatibility. An example is SU-8, an epoxy-based photo resist known for its low cost, excellent chemical compatibility, and wide range of film thicknesses, ranging from 10–100  $\mu\text{m}$ . This makes SU-8 an appealing choice for micro channel fabrication, facilitating the successful implementation of organic solvent reactions in diverse applications. The second column of Table 3.2 summarizes the lithography process for fabricating a 30  $\mu\text{m}$  deep micro channel using SU8 3050 photo resist on a 40 mm  $\varnothing$ , 1 mm thick  $\text{CaF}_2$  window.

However, it is important to note that SU-8 tends to form permanent bonds with  $\text{CaF}_2$  windows, making the reuse of these windows difficult or even impossible. For more information on how to remove SU-8, refer to Section 3.8.

<b>Lithography Steps</b>	<b>SU 8</b>	<b>AZ 1518</b>
Spin Coating Speed (rpm) / Time (s)	3000 / 30	2000 / 30
Expected Depth ( $\mu\text{m}$ )	30	2.5
Soft bake temp ( $^{\circ}\text{C}$ ) / Time (min)	95 / 20	95 / 1
Exposure dose of 375 nm laser ( $\text{mJ}/\text{cm}^2$ )	400	200
PEB temp ( $^{\circ}\text{C}$ ) / Time (min)	65 / 2 and 95 / 5	110
Developer Solution / Time (s)	PGMEA / 30 (x3)	AZ MIF 300 / 30 (x2)

Table 3.2: Summary of lithography process for SU8 3050 and AZ1518 photoresist on 1 mm thick  $\text{CaF}_2$  substrate.

In addition to its primary application, the technology discussed in this chapter holds potential for the fabrication of micro channels with depths less than 5  $\mu\text{m}$ , specifically for



studying water using IR spectroscopy. Water, being a strong absorber of mid-IR light, requires minimizing the optical path length when studying its properties within an aqueous solution. To this end, the fabrication process outlined in this chapter can be adapted accordingly.

A specific example of such fabrication is demonstrated in Table 3.2, where the lithography process for creating a 2.5  $\mu\text{m}$  deep micro channel in AZ 1518 photo resist is summarized. This particular micro channel is designed using AZ 1518 photo resist on a 40 mm  $\varnothing$ , 1 mm thick  $\text{CaF}_2$  window. By employing this fabrication technique, one can effectively explore the characteristics and behaviors of water through IR spectroscopy while maintaining the crucial requirement of minimizing the optical path length in the aqueous medium.

### 3.8 Reusing calcium fluoride windows after lithography

One advantage of the fabrication method outlined in this chapter is that windows can be re-used. This aspect is crucial as it significantly lowers the overall cost of producing the devices. The process of reusing windows differ based on the characteristics of the photoresist used.

#### 3.8.1 *Removing AZ40-XT and AZ 1518 photo resist*

The AZ40-XT and AZ 1518 photo resists are soluble in organic solvents, allowing for their removal through the following wet etching processes:

- Sonicate the bonded  $\text{CaF}_2$  sandwich in acetone for 5 minutes.
- Place the assembly on a flat surface and gently insert the soft rubber tip of a cleanroom substrate wafer between the windows, applying gentle pressure toward the center. This action will cause the solvent to gradually move to the center, breaking the bonding.

- Repeat the sonication process in fresh acetone for another 5 minutes, and carefully wipe away any photo resist residue on the window surface using cleanroom wipes.
- Perform two rounds of sonication in methanol and isopropyl alcohol, each for 5 minutes.
- Clean the windows with lens paper and place them in a vacuum oven to remove any remaining solvent.

For optimal results, it is advisable to carry out the cleaning process immediately after the conclusion of the mixing experiment. This is particularly important when working with AZ photoresist, as it exhibits strong adhesion to  $\text{CaF}_2$  windows. Delaying the cleaning process for an extended period can make the removal of the photoresist more challenging.

### *3.8.2 Removing SU8 3050*

The removal of SU8 photoresist using traditional wet etching methods is not feasible due to the chemical resistance of the polymerized epoxy. However, there is an alternative method for removing the SU8 film, which involves heating the substrate to weaken the adhesion and manually peeling off the film using a sharp tool. The following alternative method for removing the SU8 film using heat and manual peeling involves potential risks, such as burns or cuts. It is based on experiential learning and should be performed with caution and proper safety measures.

- Place the bonded  $\text{CaF}_2$  sandwich on a 110 °C hotplate for 2 minutes.
- Carefully place the sandwich on a flat surface and immediately separate the windows by inserting the soft rubber tip of a cleanroom substrate wafer and applying firm pressure toward the center. It may be necessary to repeat the heating step multiple times. Use thermal gloves to prevent second degree burns.

- To remove SU8 from individual windows, place a window on a 70 °C hot plate for 1 minute. Then, using a sharp razor, gently penetrate the edge of the film and peel it off, similar to removing a protective film. Please note that this process may affect the surface quality of the CaF<sub>2</sub> window.

While these procedures enable the reusability of CaF<sub>2</sub> windows, it is important to note that they can degrade the surface quality of the windows. For instance, during ultrasonic cleaning, the high-frequency vibrations and cavitation can potentially lead to micro-fractures, surface roughening, or even breakage of the window. The use of a razor for film removal can cause scratches on the window surface. Additionally, the compression applied during bonding may introduce minor cracks, thereby limiting the window's reusability to less than 50 cycles.

Given these factors, it is crucial to handle CaF<sub>2</sub> windows with care and regularly assess their condition to ensure optimal performance and longevity throughout the fabrication process.

# CHAPTER 4

## FLOW SETUP AND CHARACTERIZATION OF MIXING

### 4.1 Overview

Chapter 3 provided a comprehensive description of the fabrication and characterization of the CaF<sub>2</sub>-based micromixer. Building upon that foundation, this chapter focuses on the integration of the micromixer into a flow cell for spectroscopic analyses. It involves the design and construction of a flow cell and integration to a syringe pump for controlled flow. To ensure a robust fluidic pathway and minimize the risk of leakage, high precision syringe pumps, rigid stainless steel syringes, and durable Teflon tubing are employed.

The primary objective of this chapter is to assess the degree of mixing achieved with the different mixer designs introduced in Chapter 3.2. This assessment is conducted through a combination of qualitative and quantitative methods using visible and IR spectroscopies. Initially, food color dyes were employed to visually evaluate the degree of mixing in the serpentine mixer, utilizing an optical microscope. Subsequently, fluorescence microscopy is used for quantitative analysis of mixing in both the serpentine and inchworm mixers, while a quenching experiment offers a molecular perspective on the mixing process. Furthermore, an additional pH mixing experiment is carried out using IR spectroscopy to complement the mixing measurements.

### 4.2 Flow cell for spectroscopy

A flow cell plays a crucial role in fluidic analysis within a microfluidic device. It provides a defined pathway for transferring samples from a source, such as a syringe pump, through the micromixer, enabling spectroscopic analysis, and finally out to a collection vessel. Designing and constructing a flow cell for spectroscopy requires careful consideration of various factors, including geometry, optical access, and compatibility. In this thesis, 3D printing, specifically

Stereolithography (SLA), is utilized to fabricate the flow cell. SLA 3D printing employs a light source, such as a laser, to solidify liquid resin into a precise and watertight plastic material. 3D printing technology offers distinct advantages by enabling the fabrication of intricate and complex designs that would pose challenges or be impractical to produce using traditional manufacturing methods such as machining. With 3D printing, the process of going from conceptualization to physical model is significantly accelerated, allowing for quick and cost-effective prototyping. This expedites the iterative design process and facilitates prompt improvements in design.

#### 4.2.1 Anatomy of flow cell

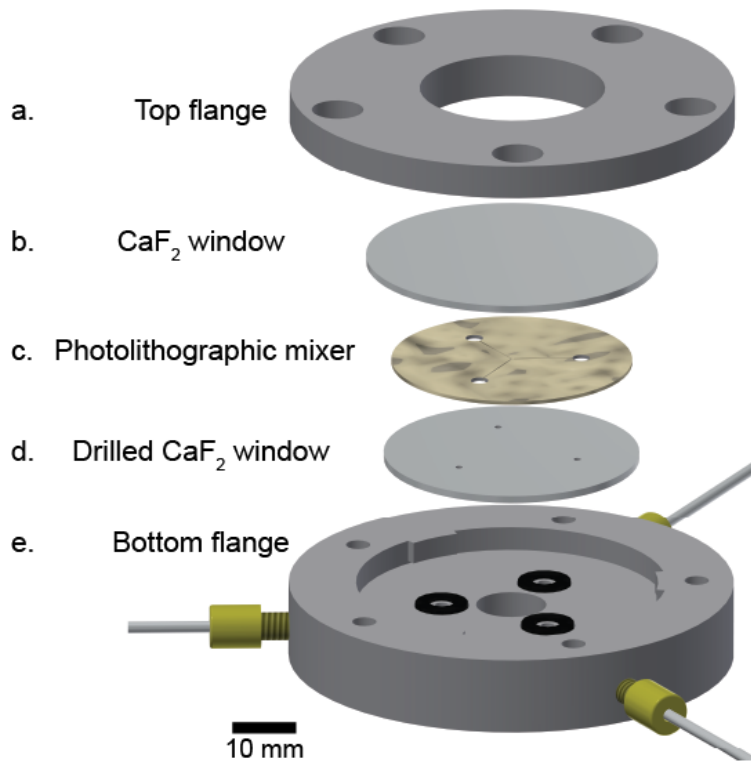


Figure 4.1: Design of the 3D printed compression cell. (a) Top compression flange, (b) 1 mm thick, 40 mm  $\varnothing$  CaF<sub>2</sub> window onto which the mixer is fabricated, (c) 33  $\mu$ m thick AZ 40XT photoresist film (d) 1 mm thick, 35 mm  $\varnothing$  CaF<sub>2</sub> window with drilled inlet and outlet ports, (e) Bottom flange containing internal tubing connections, and 10 mm  $\varnothing$  aperture for transmission measurement.

The schematic of the 3D printed flow cell along with the CaF<sub>2</sub>-based micromixer is shown in Figure 4.1. The micromixer consists of one drilled 35 mm CaF<sub>2</sub> window and one 40 mm CaF<sub>2</sub> window with the microchannel fabricated on sandwiched layers of photoresist. The mixer is compressed in a 3D-printed hard-plastic housing which directs the flow of fluid into and out of the drilled holes of the 35 mm CaF<sub>2</sub> window. Five screws in the top flange of the housing are used to make an O-ring seal between the drilled CaF<sub>2</sub> inlet and outlet ports and the bottom flange of the housing. The inlet ports of the bottom flange are connected by tubing to a syringe pump that drives the reactants through the microchannel.

The majority of the experiments presented in this thesis utilize various adaptations of the cell depicted in Figure 4.1. For the fabrication of the flow cell, we employed the Form 3+ SLA 3D printer from Formlabs. This printer utilizes a UV laser to selectively cure the liquid resin layer by layer, resulting in high-resolution prints with accurate details. The 3D printing process begins with the creation of a CAD model using software like Autodesk Inventor or Fusion 360. These CAD models capture the desired geometry and specifications of the flow cell. Once the design is finalized, the CAD model is exported in standard tessellation language (STL) format, representing the object's geometry as a collection of interconnected triangles.

To prepare the STL file for printing, it is imported into preform software, which is specific to the Formlab SLA printers. The software analyzes the geometry and generates the necessary supports that provide stability to overhanging or delicate parts of the model during the printing process, preventing print failures and ensuring structural integrity. The placement and density of supports are determined in built algorithm that take into account the geometry and orientation of the model. These supports are temporary structures that can be easily removed after printing is completed.

Figure 4.2 illustrates a complete cell assembly. To ensure a robust seal at the bottom flange, square-profile buna-N o-rings (4061T112, McMaster-Carr) are securely attached us-

ing a small quantity of cyanoacrylate adhesive (75445A73, McMaster-Carr). The adhesive effectively holds the o-rings in place, significantly reducing the possibility of leaks from the bottom counter bore of the assembly. The square-profile o-rings offer an advantage over round-profile o-rings due to their flat edges, which cover a larger surface area, thereby providing enhanced sealing capabilities.

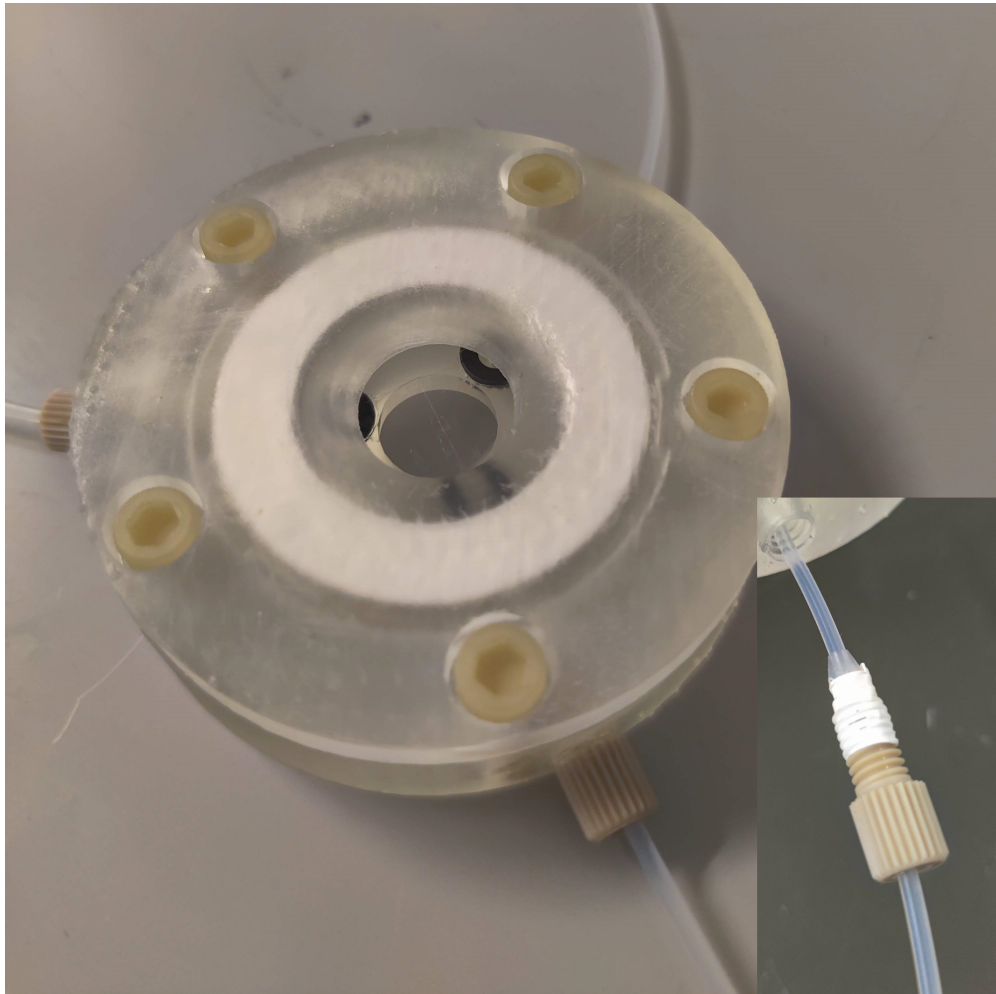


Figure 4.2: Fully assembled flow cell with detailed view of the PEEK connection in the inset

For convenient and dust free connectivity, the CAD design of entrance and exit ports of the bottom flange contain tapped holes for the attachment of NanoTight PEEK fittings (F-333 NX, IDEX, USA). These fittings, which are 0.60 in. long, feature an ethylene tetrafluoroethylene (ETFE) ferrule designed for 1/16" OD tubing. The Teflon tubing (1622L, IDEX,

USA) is inserted into the PEEK fitting and through the flow cell ports, extending into and under the counterbore of the o-rings (Figure 4.2 inset). To ensure a leak-free operation, a combination of measures is taken. Firstly, teflon tape is applied to the threads of the PEEK fitting prior to screwing it into the 10-32 tapped hole. This tape helps to prevent any potential leaks at the fitting interface. Additionally, epoxy glue is used to make the fitting permanent, further enhancing the sealing capability and ensuring long-term stability of the assembly. This meticulous approach to the cell assembly and sealing process guarantees reliable and efficient operation of the experimental setup, minimizing the risk of leaks. Once the flow cell is assembled, the next step is to connect the inlet tubing to the syringes containing the reactant solution.

For rapid mixing applications, high flow rates are typically used, which can result in significant back pressure. To overcome this back pressure, it is necessary to utilize both a syringe and a syringe pump with suitable specifications. As derived in Chapter 2, the pressure drop ( $\Delta p$ ) in a rectangular microchannel with length  $L$ , width  $w$ , depth  $h$ , and fluid viscosity  $\mu$ , flowing at a flow rate  $Q$ , can be estimated using the equation  $\Delta p \approx \frac{12\mu LQ}{wh^3} \frac{1}{\left[1-0.63\frac{h}{w}\right]}$ .

For example, in the case of a 20  $\mu\text{m}$  wide, 30  $\mu\text{m}$  deep serpentine mixer with a length of 210  $\mu\text{m}$ , the estimated pressure drop across the mixer is approximately 150 psi. To ensure reliable performance under high pressures, we have chosen 8 mL stainless steel syringes from Harvard Apparatus. These syringes are renowned for their durability and ability to withstand peak pressures of up to 1500 psi. Furthermore, they are equipped with Swagelok fittings for tubes with an outer diameter of 1/16 in., which provides a low dead volume connection for optimal fluid transfer. In conjunction with the robust syringe, the syringe pump plays a crucial role in maintaining the integrity of the flow system. We have opted for the Pump 33 from Harvard Apparatus due to its high linear force capability (maximum of 70 lbs), exceptional accuracy, and user-friendly interface. This syringe pump provides precise control over the flow rate and exerts the necessary force to overcome the back pressure within



the microchannel.

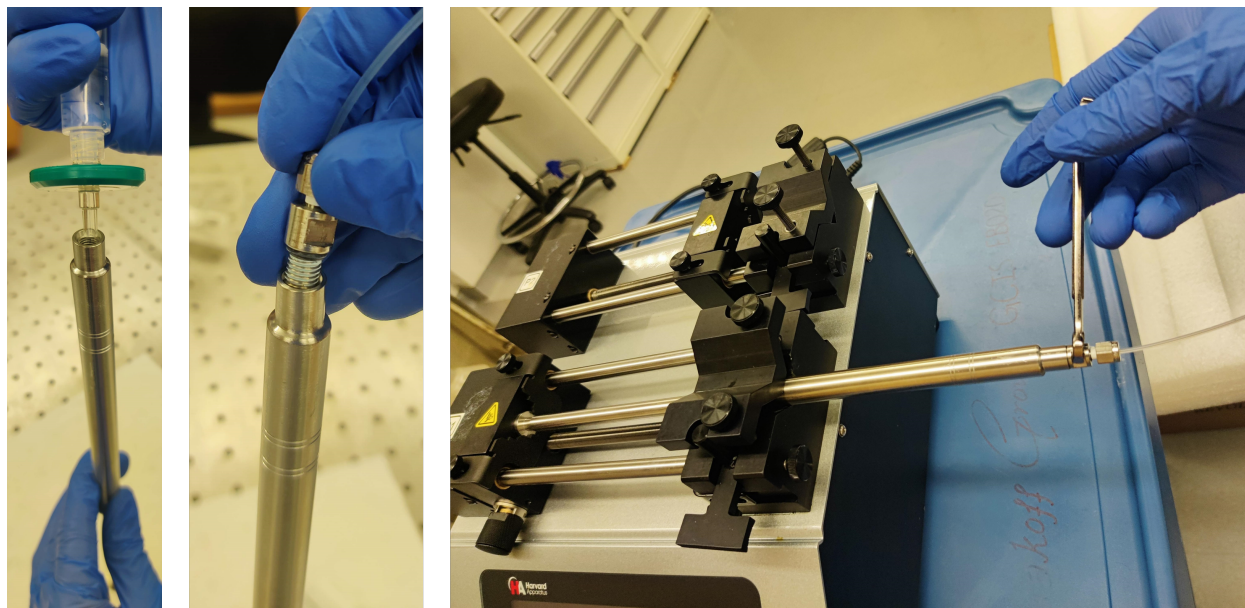


Figure 4.3: Optimized procedure for sample loading. (Left) Transfer of filtered samples into the stainless steel syringe. (Center) Correct application of Teflon tape and hand-tight attachment of the Swagelok fitting to the syringe. (Right) Secure connection of the loaded syringe to the syringe pump.

However, due to the small size of the microchannel and the presence of a 20-micron-sized mixer, which is comparable to typical dust particles, it is crucial to follow the proper loading and connection procedure to ensure optimal performance and prevent any potential issues. Drawing from my experience spanning five years in this field, the following set of instructions has been refined and proven to be highly effective in minimizing leaks and ensuring reliable operation. By diligently following these steps, one can maximize the performance and reliability of your experimental setup:

- Thoroughly clean all components of the stainless steel syringe by sonication in water and isopropyl alcohol (IPA). After cleaning, dry the syringes in an oven to remove any residual solvent. Assemble the syringes in preparation for sample loading.
- Prior to loading the samples, it is essential to filter them at least twice using  $0.2 \mu\text{m}$

syringe filters. For this purpose, we highly recommend using PTFE syringe filters, which offer excellent filtration efficiency.

- Begin the sample loading process by first transferring the filtered samples into a 10 mL BD plastic syringe. From there, carefully load the samples into the stainless steel (SS) syringe using a fresh syringe filter, as illustrated in Figure 4.3 (left). It is important to note that air bubbles may become trapped in the syringe barrel during this process. To ensure proper loading, gently tap the side of the syringe to dislodge any trapped air bubbles. Failure to remove air bubbles from the syringe barrel may compromise its functionality and performance.
- Connect the Teflon tubing into the Swagelok fitting by finger-tighten the nut onto the fitting body until resistance is felt followed by fully tightening the nut using a wrench.
- Before connecting the Swagelok female connector to the syringe male body, apply a layer of Teflon tape around the threaded portion. This helps create a tight and leak-free seal. Attach the connector to the syringe hand-tight, as shown in Figure 4.3 (center).
- Once the syringe is loaded with the sample and securely connected to the Swagelok fitting, it is ready to be attached to the syringe pump. Align the fitting with the pump's connection port and tighten it using an appropriate wrench. Ensuring a snug fit will prevent any accidental disconnections during the experiment.
- Prior to placing the  $\text{CaF}_2$  sandwich, it is essential to prime the Teflon tubes with the sample solution. Neglecting this step can result in the formation of numerous air bubbles, which have a tendency to carry any dust particles present along the way.
- Use cleanroom wipes to thoroughly dry the bottom flange o-rings, eliminating any residual solution from the priming process. Carefully align the drilled holes of the  $\text{CaF}_2$  sandwich with the corresponding o-rings, and proceed to compress the top flange

using plastic screws. It is recommended to utilize glass-filled nylon socket head screws (91221A445, McMaster-Carr). It's essential to be aware that repeated use can cause these screws and tapped holes to wear out, potentially compromising the compression of the flow cell. To address this issue, we have recently introduced metal screws that are secured together using a nut, resulting in a significant improvement in compression.

The flowcell is now ready for integration into a microscope setup. Figure 4.4 provides an illustrative example of how this integration can be achieved with Bruker Hyperion IR microscope. To facilitate this integration, a custom-designed 3D printed holder is employed to securely attach the flowcell to the motorized stage. This holder design enables convenient rotation of the flowcell, allowing for alignment of the mixer with the axis movement if necessary. Control of the motorized stage can be accomplished using either the joystick, OPUS, or the LabVIEW VI interface. The LabVIEW VI interface offers motor control with a resolution as fine as  $0.1 \mu\text{m}$ , enabling precise adjustments during experiments. The Pump 33 features a user-friendly touchscreen interface that allows for effortless control of the flow parameters, simplifying the experimental process. To facilitate observation, the microscope incorporates an LED screen that provides clear visibility of the mixer under 15x magnification, ensuring accurate positioning of the mixer and the following channel within the flowcell setup.

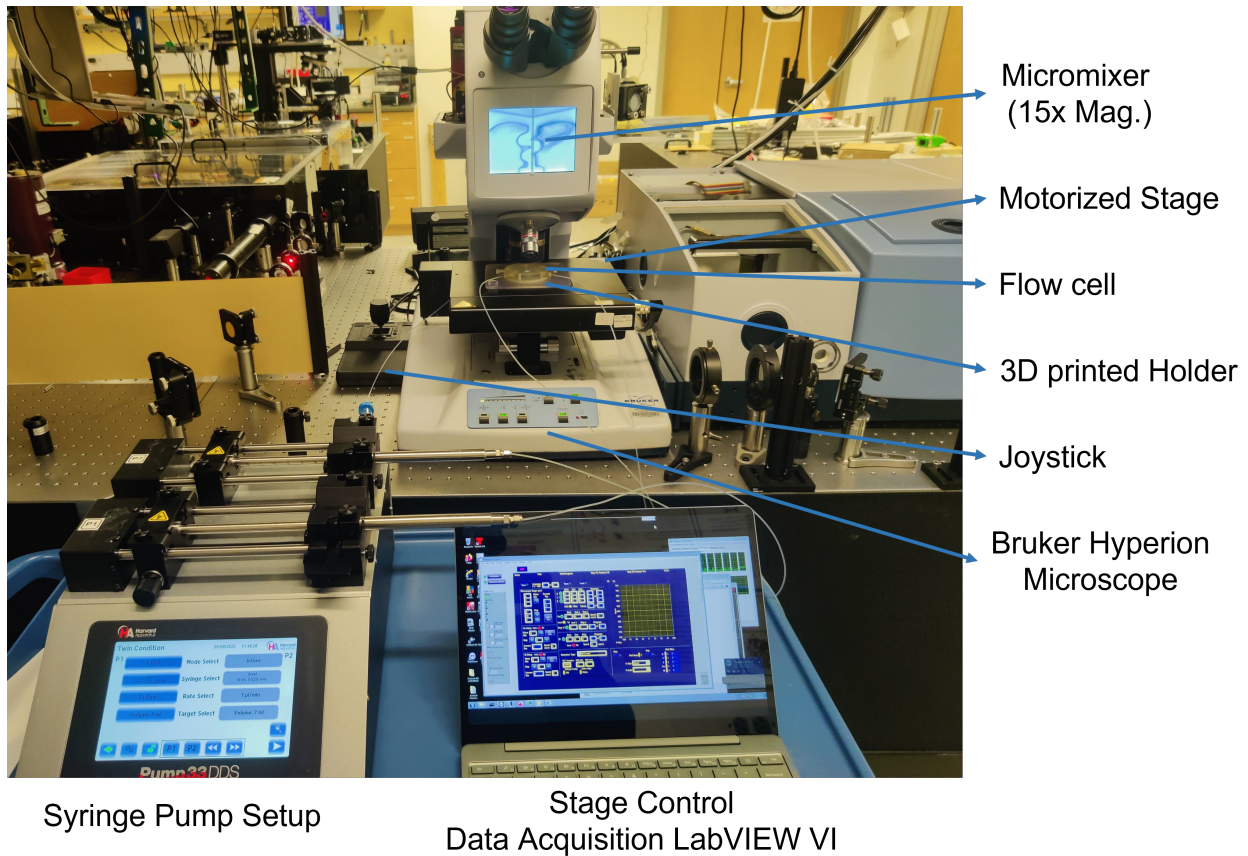


Figure 4.4: Experimental setup involving integration of flowcell into Bruker Hyperion IR microscope.

### 4.3 Characterization of mixing

Mixing can be characterized at both qualitative and quantitative levels, by analyzing various parameters, such as the spatial distribution of the mixed fluids, the uniformity of concentration gradients. In our study, we employed a series of optical and IR microscopy techniques to characterize the mixing process.

#### 4.3.1 *Mixing of colored solution*

The efficiency of mixing in the microchannel was assessed qualitatively by observing the mixing of two different food color solutions in water. This simple yet effective method allowed

for a visual inspection of mixing homogeneity. Microscope images of the mixing process in a serpentine mixer at various flow rates are presented in Figure 4.5. The images were captured using a 12-megapixel camera on an Olympus BH2 Upright Microscope equipped with trans-illumination and a 10x magnification objective.

To enhance the visibility of the mixing patterns, the captured colored images were subjected to image processing using the Color/Channel Tool in ImageJ software. Specifically, the red color channel was isolated to highlight the regions where mixing occurred. The resulting processed images clearly depict the areas of mixing, as illustrated in Figure 4.5. At a flow rate of 100  $\mu\text{L}/\text{min}$ , the two food color solutions flow parallel to each other, representing laminar flow. As the flow rate is increased to 200  $\mu\text{L}/\text{min}$ , the laminar flow becomes distorted, with the degree of distortion becoming more evident at flow rates ranging from 300-500  $\mu\text{L}/\text{min}$ , suggesting some level of mixing of the food colors. Above 600  $\mu\text{L}/\text{min}$ , it becomes difficult to distinguish the two colored solutions, providing a qualitative conclusion of homogeneous mixing.

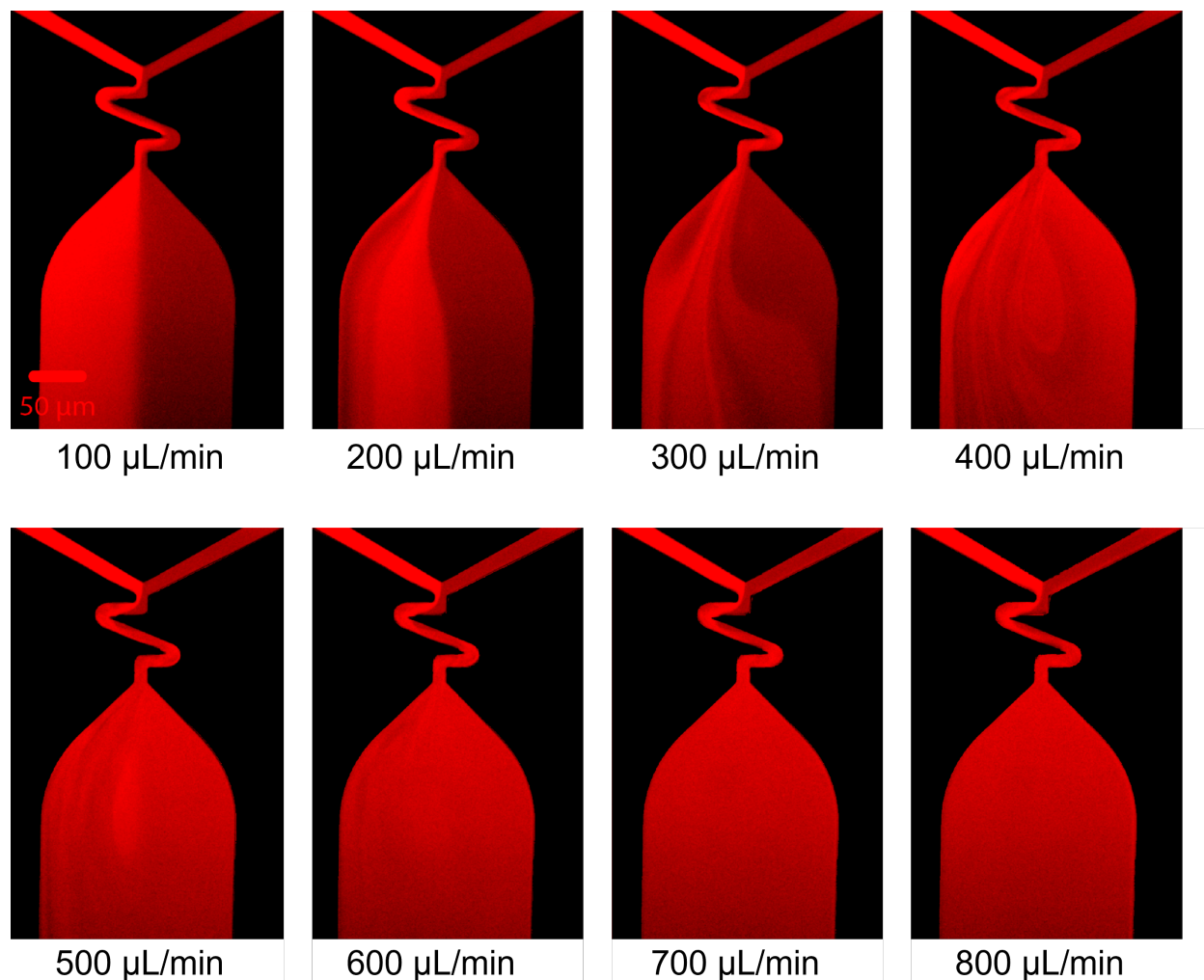


Figure 4.5: Qualitative assessment of food color mixing in the microchannel. The images demonstrate the mixing process at different flow rates, highlighting the transition from laminar to turbulent increased flow with increased mixing homogeneity with increasing flow rates.

#### 4.3.2 *Mixing of rhodamine 6G with water*

The spatial uniformity of mixing was further characterized by fluorescence imaging of the observation channel upon mixing of a Rhodamine 6G solution with water. Images were acquired using an inverted fluorescence microscope (Nikon Ti-eclipse, 10× objective) with a CCD camera (iXon X3, Andor). The filter cubes of G-2E/C (excitation filter: 528-553 nm bandpass, dichromatic mirror: 565 nm long pass, emission filter: 590-650 nm bandpass) was



employed. These imaging tools enabled the acquisition of high-quality images, facilitating the quantitative assessment of concentration gradients and providing valuable insights into the mixing process. Figures 4.6 a,c show images of the fluorescence distribution in the observation channel at various flowrates for the “inchworm” and “serpentine” type mixer, respectively. Figures 4.6 b,d show the corresponding transverse fluorescence count profile 150  $\mu\text{m}$  downstream from the mixer exit. At a flowrate of 100  $\mu\text{L}/\text{min}$  the flow is laminar in both mixers with little diffusion across the interface separating dye solution and water. At flowrates between 300  $\mu\text{L}/\text{min}$  and 500  $\mu\text{L}/\text{min}$  swirls from the folding of flow between solutions is observed. A spatially uniform fluorescence distribution is observed at a flowrate greater than 600 and 700  $\mu\text{L}/\text{min}$  for the “serpentine” and “inchworm”, respectively, as verified by plateauing of the transverse fluorescence count profiles at these flowrates.

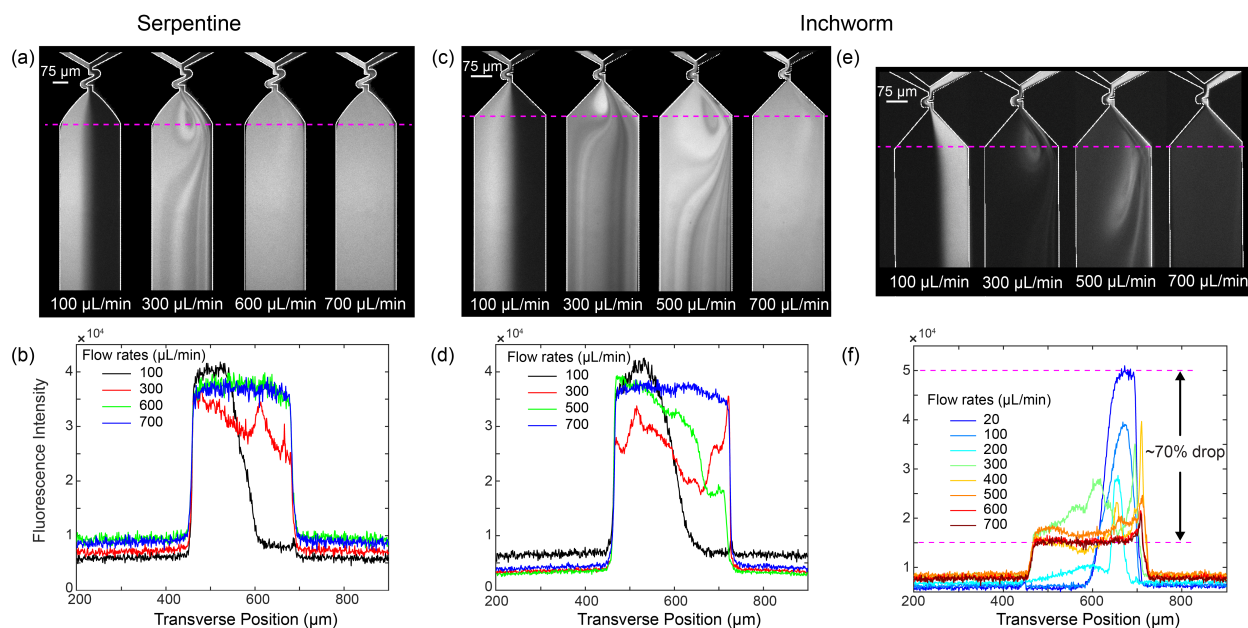


Figure 4.6: Fluorescence images of the observation channel following mixing of 50  $\mu\text{M}$  rhodamine 6G solution and water in (a) serpentine and (c) inchworm mixer at a flowrate 100, 300, 500/600 and 700  $\mu\text{L}/\text{min}$ . Fluorescence distribution across the channel 150  $\mu\text{m}$  from the exit of the mixer, dashed magenta line, is shown on (b) and (d) suggest homogeneous mixing at flowrate  $>600$   $\mu\text{L}/\text{min}$ . (e) Fluorescence images of the observation channel following the quenching reaction of 1  $\mu\text{M}$  fluorescein by 0.5 M potassium iodide in an “inchworm” mixer. (f) Fluorescence distribution suggests 70 % drop in fluorescein fluorescence upon complete mixing.

### 4.3.3 Quenching of fluorescein fluorescence

The quenching of dye fluorescence in a micromixer serves as a valuable method for assessing whether homogeneous mixing has been achieved at the molecular scale. This process involves the suppression of fluorescence emitted by a slowly diffusing dye, such as fluorescein, when it is mixed with a buffer that contains a fast-diffusing quencher, such as potassium iodide (KI). This is because iodide ions quench light emission by providing a non-fluorescent pathway through which excited fluorescein molecules can relax to their ground state [122]. The fluorescence quantum yield of a fluorescein and iodine mixture depends strongly upon the concentration of iodide. Previous research has demonstrated that a concentration of 0.5 M of potassium iodide can achieve a quenching efficiency of approximately 70% in fluorescein fluorescence [123, 124].

The mixing of a 1  $\mu$ M fluorescein with 0.5 M KI was examined in the same inverted fluorescence microscope with filter cubes of U-MWB2 (excitation filter: 460-490 nm bandpass, dichromatic mirror: 500 nm long pass, emission filter: 520 nm IF). The results complement the observation seen with fluorescence dilution of Rhodamine 6G (Figures 4.6 e,f). Laminar flow with persistent fluorescent streams are observed in the observation channel below 500  $\mu$ L/min, but at a flowrate of 700  $\mu$ L/min, the peak fluorescence and integrated area under the fluorescence profiles are reduced by 70%, as expected for completion of the quenching reaction. At the highest flow rates, a small excess of fluorescein fluorescence is observed within 10  $\mu$ m of the right wall in the observation channel, suggesting that the “inchworm” design does under-perform the “serpentine” in terms of transverse mixing homogeneity. However, quenching uniformity following the inchworm mixer is otherwise constant across the measured regions of the observation channel.



### 4.3.4 Mixing in 3-Turn mixer

This design of three turn mixer serves two purposes: (1) minimizing the back pressure that could lead to leaking and or mixer damage, by allowing homogeneous mixing at lower flow rates compared to inchworm and serpentine mixer, and (2) improving the time resolution of the measurement by allowing measurement with tightly focused IR beam from a laser source. Incorporating multiple turns within the mixer's geometry enables chaotic advection even at lower flow rates, resulting in improved intermixing of fluid streams. Narrowing the width of the observation region reduces the  $\tau_{obs}$ , thus improving the time resolution.

The fluorescence images of the observation channel in the 3-turn mixer following quenching reaction of  $1 \mu\text{M}$  fluorescein with  $0.5 \text{ M}$  KI at different flowrate is shown in Figure 4.7 (a). The transverse fluorescence distribution across the channel at a distance  $30 \mu\text{m}$  from the exit of the mixer (dashed white line) is shown in Figure 4.7 (a). The distribution reaches a plateau at flow rates of  $350 \mu\text{L}/\text{min}$  and higher. This indicates that the 3-turn mixer is capable of achieving effective mixing at flow rates approximately half those required by serpentine and inchworm mixers.

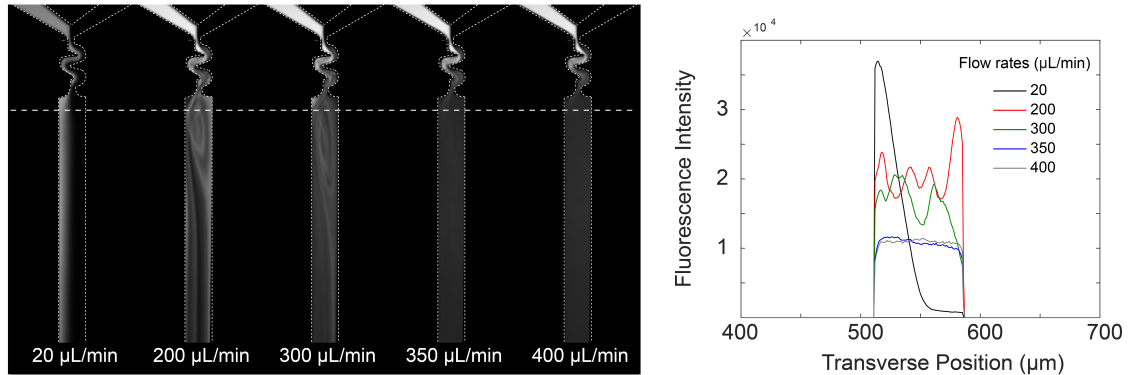
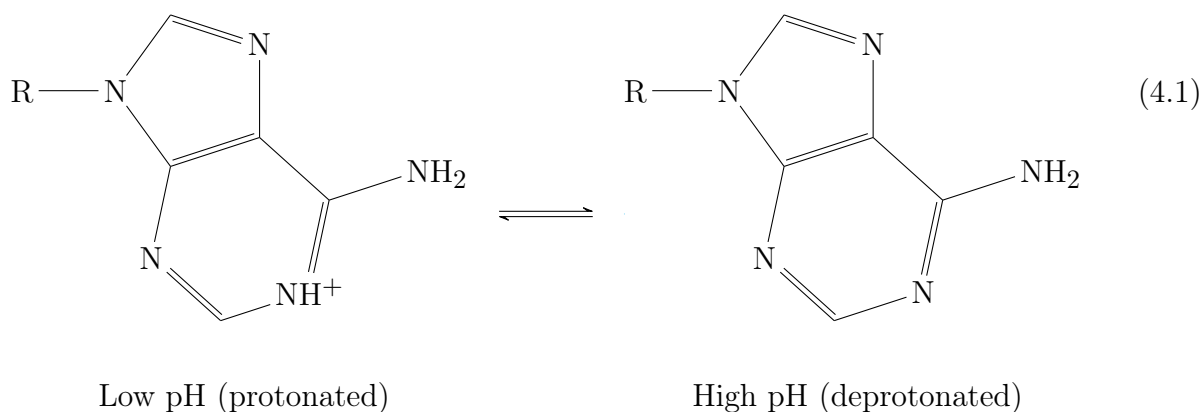


Figure 4.7: (a) Fluorescence images of the observation channel in 3-turn mixer following quenching reaction 1, 100, 300 and 600  $\mu\text{L}/\text{min}$ . (b) Fluorescence distribution across the channel  $30 \mu\text{m}$  from the exit of the mixer, dashed magenta line, suggest homogeneous mixing at flowrate  $>300 \mu\text{L}/\text{min}$ .

### 4.3.5 IR spectroscopy to demonstrate mixing

To confirm that these fluorescence imaging observations are consistent with infrared spectroscopy measurements, we monitored pH-jump experiments of adenosine monophosphate (AMP) using the serpentine mixer. AMP can be used as a ratio metric pH indicator near its 3.8 pKa using the strong and clearly resolved absorbance bands at  $1666\text{ cm}^{-1}$  and  $1624\text{ cm}^{-1}$  that arise from the protonated and deprotonated states of the adenosine ring, respectively.



In Equation 4.1, the ribose-phosphate moiety of AMP is represented by R. Since protonation/deprotonation reactions in water are expected to occur within a few microseconds, a homogeneously mixed solution should be fully equilibrated at the final pH upon exiting the mixing channel [125, 126, 127]. Because the AMP vibrational transitions overlap with the  $\text{H}_2\text{O}$  bending vibration, we performed experiments in  $\text{D}_2\text{O}$ . The pH of the solution measured using standard glass electrode and is reported as  $\text{pH}^*$ , which can be converted to pD using  $\text{pD} = \text{pH}^* + 0.41$  [128]. We monitored mixing of a 16 mM,  $\text{pH}^* 3$  AMP solution with 50 mM,  $\text{pH}^* 6.9$  sodium phosphate buffer as a function of flowrates. The large IR spot size in the microscope limits the ability to fully assess the spatial variation of pH within the observation channel, however we can test for spectral variations between the left and right sides of the channel. Figure 4.8 shows peak normalized FTIR spectra with the measurement focus centered on either side of the observations channel near the exit of a serpentine mixer

and compares these spectra with those of steady-state AMP solutions at the initial (dashed magenta) and final pH (dashed red). Consistent with the fluorescence characterization, the IR spectra varies, from reproducing the individual input solutions at the 100  $\mu\text{L}/\text{min}$ , to variations consistent with inhomogeneous mixing for 300  $\mu\text{L}/\text{min}$ , to spatially uniform and consistent with the final pH for flowrate of 600  $\mu\text{L}/\text{min}$ .

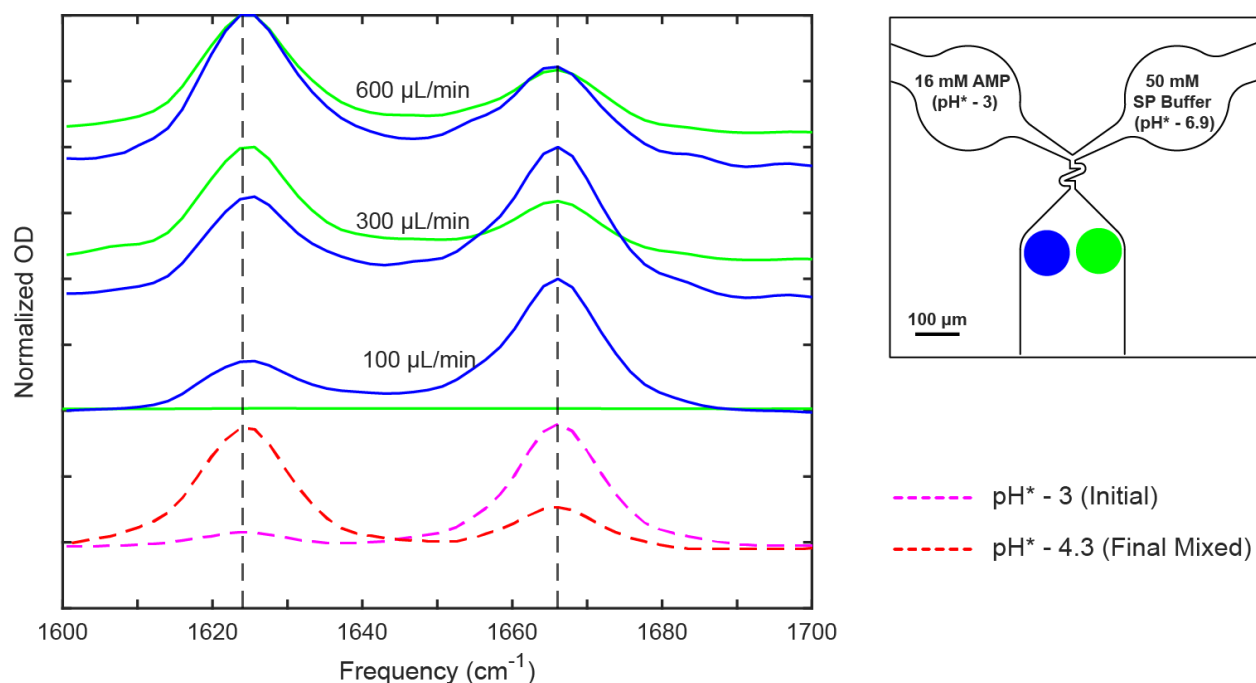


Figure 4.8: Peak normalized FTIR spectra at a flowrate 100, 300, 600  $\mu\text{L}/\text{min}$  of AMP pH jump experiment monitored at the exit of the “serpentine” mixer. The blue and green dot in the inset shows the measurement location and the relative size of the IR beam and the steady state spectra and initial and final pH is shown in dashed magenta and red lines, respectively. The rise in  $1624\text{ cm}^{-1}$  and drop in  $1666\text{ cm}^{-1}$  mode with increasing flowrate, which become uniform across both measurements at 300  $\mu\text{L}/\text{min}$  suggests homogeneous mixing, consistent with fluorescence imaging.

#### 4.4 Improving flowcell assembly

The utilization of 3D printing enables rapid prototyping of flow cells. However, certain drawbacks related to chemical compatibility, robustness, and durability should be considered. In particular, the commonly used Formlabs clear resin is incompatible with various organic

solvents such as acetone and methanol, making flow cell cleaning challenging. Consequently, it is common to encounter small dust particles within the microchannel when reusing the flow cell. Figure 4.9a illustrates an example of a dust particle obstructing the serpentine mixer, potentially originating from cured resin in the flow cell's fluid connection ports. This obstruction increases the hydrodynamic resistance as the fluid flows through the mixer, leading to the buildup of localized pressure. This pressure can result in catastrophic outcomes, such as, leaking from the o-ring interface, damage to mixer wall, and breaking of the bonded surface. In some cases, the pressure stress can even propagate to the brittle  $\text{CaF}_2$  windows, leading to cracks, as depicted in Figure 4.9 b.

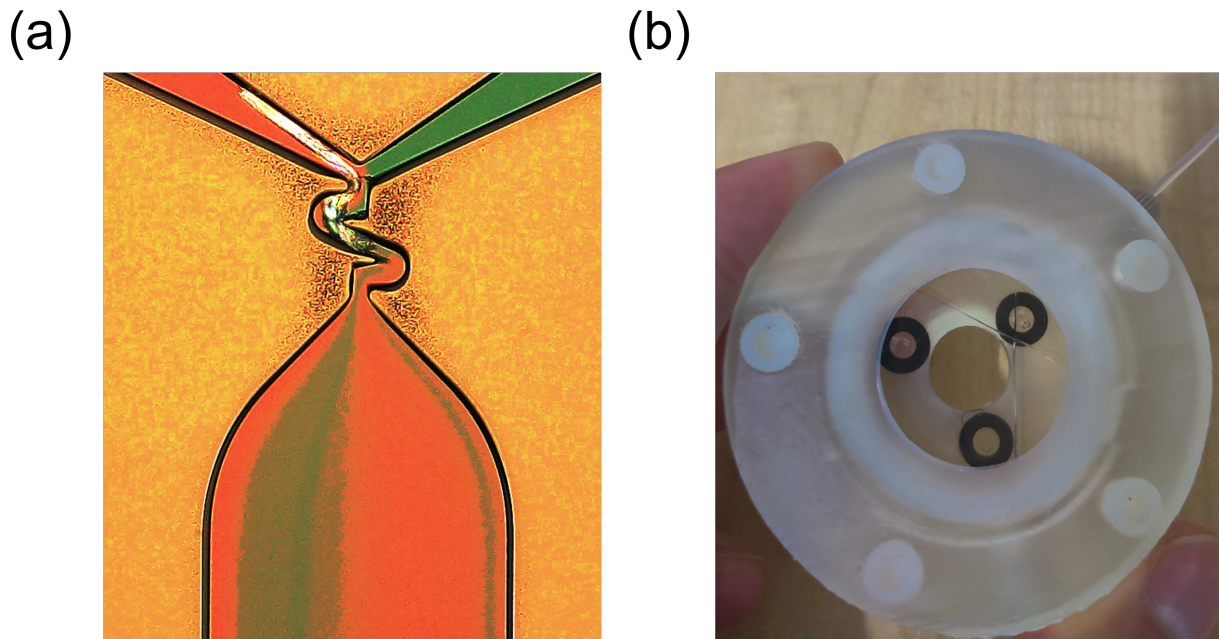


Figure 4.9: Illustration of common failures observed during mixing experiments. (a) Microscope image depicting dust particles lodged in a serpentine mixer, leading to blockage. The clogged mixer can cause a buildup of high pressure, potentially damaging the mixer wall. Additionally, this can result in catastrophic failure of the flow cell, as demonstrated by cracks in the  $\text{CaF}_2$  sandwich assembly shown in (b).

To minimize the risk of dust, the flow cell should be cleaned in a cleanroom environment. For optimal results, the recommended cleaning method is to sonicate the cell using a resin-compatible solvent such as isopropyl alcohol (IPA). Sonication effectively dislodges tiny

particles from the cell surface that otherwise would flow into the microchannel. However, repeated sonication can impact the strength of epoxy-glued inlet connection port and decrease the lifespan of the flow cell. Other factors, including print quality and post-printing processing, can also influence the overall lifespan of the flow cell. Repeated tightening of compression screws can tear or loosen the thread in the bottom flange. This problem manifests as screws loosening from high pressure generated during flow experiment. In practice, it is typical to reuse a 3D printed flow cell for approximately five to ten experiments. Other suggested improvements are itemized below.

- **Improving the compression of the flow cell:** The effective performance of the flow cell depends on the tightness of the compression provided by the top flange. However, the plastic screws used for tightening into the threaded 3D printed body may experience wear and tear over time, which can affect their durability. To address this issue, one potential solution is to utilize metal locktite bolts for compression. This requires ensuring that the holes in the top and bottom parts of the flow cell are large enough to accommodate the locktite bolts. The bolts should be securely fastened with metal nuts, offering superior compression compared to plastic screws. This enhancement can contribute to improved durability and longevity of the flow cell assembly.
- **Improving the robustness of the flow cell:** The  $\text{CaF}_2$  sandwich assembly plays a critical role in the flow cell, but it is prone to cracking and fractures, as shown in Figure 4.9 b. To enhance its robustness, one approach is to use thicker  $\text{CaF}_2$  windows. Thicker windows can provide increased strength and resistance to external forces. However, in situations where thinner windows are necessary, such as for 2D IR spectroscopy, it is recommended to incorporate a cushioning mechanism. This can be achieved by using a PTFE washer (shown in Figure 4.2, part number 96371A213 from McMaster-Carr), which helps minimize mechanical stress caused by uneven external forces from the top

compression flange.

Another challenge associated with 3D printed flow cells is their limited temperature withstand capabilities. These flow cells can typically withstand temperatures up to 80°C, limiting its usage to room temperature experiments. To address this limitation, it is beneficial to construct the final flow cell using metal materials. Metal offers improved temperature resistance, as well as enhanced robustness and durability.

Figure 4.10 showcases an early version of a machined flow cell crafted from brass, featuring nanoport assemblies for solution inlet and outlet. While this particular device does not support mixing experiments, it proves highly effective for conducting high-quality difference spectroscopy or temperature-dependent studies. It is important to note that machining a flow cell from metal generally requires more time and effort compared to 3D printing, due to the intricacies involved in the machining process.

Once a design is refined through the 3D printing process, it would be ideal to transition to a metal machined version to enhance the durability and versatility of the flow cell. This enables the flow cell to withstand higher temperatures, expands the range of possible experiments, and ensures long-term reliability.

a. Nanoport connection

b. Brass top flange

c. Drilled  $\text{CaF}_2$  window

d. Mixer

e.  $\text{CaF}_2$  window

f. Brass bottom flange

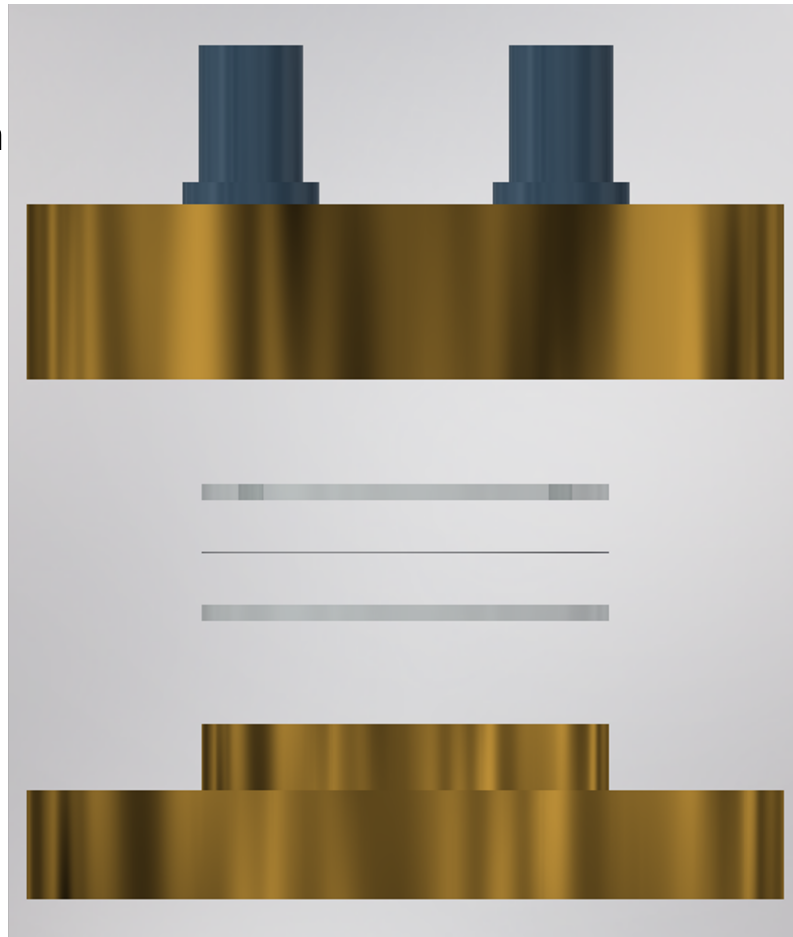


Figure 4.10: Design of the machined brass flow cell. (a) Nanoport assemblies for internal tubing connection (N-333, IDEX, USA), (b) Brass flange with opening for nanoport, and through holes for 8-32 screws (c) 1 mm thick, 25 mm  $\varnothing$  drilled  $\text{CaF}_2$  window with 1.5 mm  $\varnothing$  two holes 19 mm apart, (d) Mixer - either photoresist film or 3M 30  $\mu\text{m}$  double sided sticky tape, (e) 1 mm thick, 25 mm  $\varnothing$   $\text{CaF}_2$  window (f) Bottom brass flange with tapped holes for 8-32 screws.

# CHAPTER 5

## TIME-RESOLVED IR SPECTROSCOPY IN AQUEOUS SOLUTION

### 5.1 Overview

Time-resolved spectroscopy is a powerful technique utilized in various scientific disciplines to investigate dynamic processes. Its main advantage lies in the ability to observe the evolution of molecular systems on various time scales. In contrast to conventional spectroscopy, which focuses on steady-state and equilibrium properties, time-resolved spectroscopy captures the time-dependent behavior of a system.

When employing time-resolved spectroscopy to extract kinetic and dynamic information from a chemical system, several key considerations must be addressed. These include achieving high temporal resolution to capture rapid dynamic events, optimizing the signal-to-noise ratio for accurate data analysis, carefully selecting the data acquisition time to cover the entire temporal evolution without introducing artifacts, ensuring precise calibration of the time axis for accurate determination of time intervals, utilizing appropriate data processing methods tailored to the system's characteristics, ensuring instrument stability and data reproducibility, and selecting suitable models for interpretation that accurately represent the underlying processes. In this chapter, we delve into aspects of extracting time-resolved data using IR spectroscopy.

### 5.2 Data acquisition

We will start by explaining the instrumentation and data acquisition process. The absorption measurements were performed in transmission measurement mode using either a commercial FTIR instrument (Vertex 70, Bruker Optics Inc., USA) or homebuilt FTIR instrument con-



nected to IR microscope (Hyperion 2000, Bruker Optics Inc., USA). The primary distinctions between the setups are the IR source, interferometer, and data acquisition software.

The Vertex 70 FTIR instrument is equipped with a glowbar source, which utilizes a silicon carbide (SiC) resistor heated by an electric current. Glowbar sources are known for providing a broad range of infrared wavelengths (1–50  $\mu\text{m}$ ) with high reliability and long service life. The ROCKSOLID interferometer, employed in the Vertex 70, is a Michelson interferometer design that incorporates dual retroreflecting cube corner mirrors arranged in an inverted double pendulum configuration. It features a wear-free pivot mechanism at the center of mass, eliminating mirror tilt and shear, and providing exceptional stability, reliability, and resistance to vibration and thermal effects. This design ensures a high signal-to-noise ratio, enabling fast and accurate measurements. The beam splitter used in the setup is a potassium bromide (KBr) with a bandwidth ranging from 400 to 8000  $\text{cm}^{-1}$ . Data is collected using the video assisted measurement wizard in the Bruker OPUS software.

The homebuilt FTIR setup utilizes a tunable mid-IR source generated by an optical parametric amplifier (OPA) with a 1 MHz 1033 nm fiber laser pump source. Further details regarding the design and characterization of this setup can be found elsewhere [129]. The OPA offers simple tuning capabilities within the range of 3–7.5  $\mu\text{m}$ , providing >10 nJ pulse energy, 85–165  $\text{cm}^{-1}$  bandwidth, and 140–540 fs durations. The setup utilizes a Mach-Zehnder interferometer as the interferometer, and additional details about it can be found in Lukas Whaley-Mayda’s thesis (page 159) [130]. Data acquisition is performed using the FEIR Hyperion LabVIEW VI.

Both setups are connected to an IR microscope (Hyperion 2000, Bruker Optics Inc., USA), as depicted in Figure 5.1, which illustrates the beam path. The microscope is equipped with a single-channel liquid nitrogen-cooled mercury cadmium telluride (MCT) infrared detector (IR Associates FTIR-16-0.50) for detecting the glowbar IR source. For the laser IR source, a fast photovoltaic MCT detector (Boston Electronics PVM10.6) is utilized. Addi-

tionally, the microscope includes a color camera (Bosch Dinion XF) and a motored XYZ sampling stage with an adjustment accuracy of  $0.1 \mu\text{m}$  and a repeatability of  $1 \mu\text{m}$ . These features enable the visualization and mapping of the microchannel for mixing experiments.

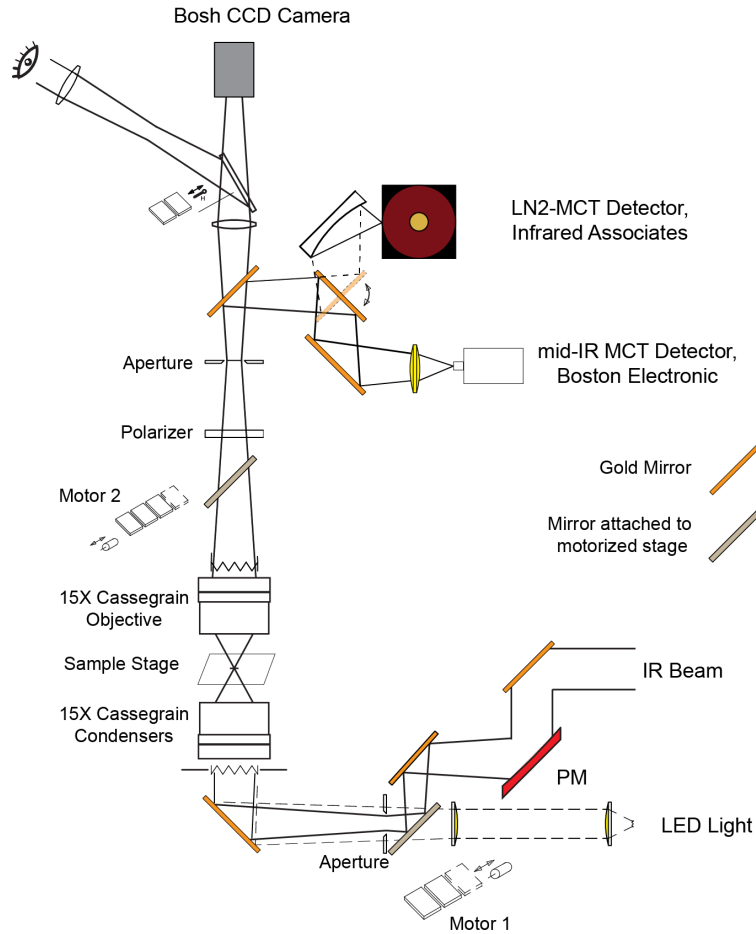


Figure 5.1: Beam path of the Hyperion 2000 infrared microscope in transmission mode. The IR beam enters the microscope from the bottom left, traverses several gold and parabolic mirrors for alignment, and aligns in parallel with visible LED illumination. It then proceeds through the 15X Cassegrain condenser, focusing onto the sample plane. The objective collects the light, which can be visualized using a binocular or the colored camera. The light is subsequently detected by either of the IR detectors. Motor 1 and 2 facilitate switching between three measurement modes: visible, IR, or IR/visible mode, achieved by selectively configuring appropriate optics. For instance, when using the IR/visible measurement mode, the gold mirror is replaced with a dichroic mirror that reflects IR light while allowing visible light to pass through. This enables simultaneous mapping and measurement of the sample.

### 5.3 Optimization of instrument parameters

Several factors such as resolution, scan speed needs to be consider while acquiring a kinetic data. Generally, in selecting the total number of IR measurement points, one needs to take into account a series of trade offs in flow rates and total sample volume, the number of time points to properly sample relaxation processes, and the desired spectral resolution and baseline noise of the IR spectra. A total volume of 8 mL permits a maximum of 22 min of measurement time at a flowrate of 700  $\mu\text{L}/\text{min}$ . To adequately get to the baseline of a relaxation process, the measured time points should span three times the  $1/e$  decay time. For most kinetic studies, measurement can be performed with a modest spectral resolution ( $4-16\text{ cm}^{-1}$ ) but this could heavily depend on the type of system being investigated and the line width of IR modes of interest. The IR brightness of the sample relative to the solvent background determines the minimum average needed to collect a spectra with a good signal to noise.

Table 5.1 summarizes the measurement parameters typically used in a standard experiment for the two setups, taking into account the aforementioned factors.

Measurement parameters	OPUS	LabVIEW
IR source	Glowbar	Laser
Aperture size (mm)	2	NA
Wavenumber range ( $\text{cm}^{-1}$ )	400 – 4000	2000 – 2200
Spectral resolution ( $\text{cm}^{-1}$ )	4	4
Acquisition speed per spectrum (s)	2	3
Number of average	4	5
Total number of measurement points	30 – 35	30 – 35
Data Acquisition time (min)	10 – 12	12 – 15

Table 5.1: Measurement parameters used for two instrument setups.

## 5.4 Data processing

Data processing plays a crucial role in spectroscopy as it enables the extraction of meaningful information from raw spectral data. The goal of data processing is to enhance the spectral quality by reducing noise, eliminating solvent and artifacts, and correcting baseline shifts. Data processing facilitates the identification and quantification of chemical components, thereby improving qualitative and quantitative analysis. In the context of the data presented in this thesis, the data processing steps are minimal and involve subtracting the background and correcting baseline shifts.

### 5.4.1 *Background subtraction*

Performing reactions in aqueous solutions presents a challenge in IR spectroscopy due to the strong and broad absorption bands exhibited by water in the mid-IR region. Therefore, it is crucial to subtract a reference spectrum of the solvent to effectively remove the water absorption bands. This background removal is typically the first step in our data analysis workflow. Figure 5.2 illustrates an example of the background correction process.

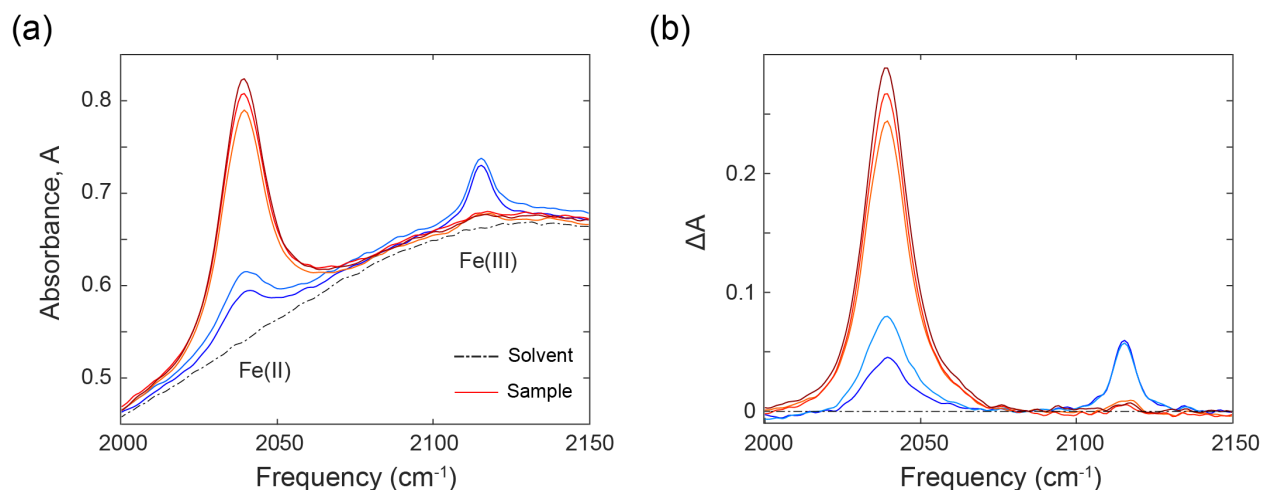


Figure 5.2: Example of solvent background correction. (a) FTIR spectra collected at various time delays in a typical mixing experiment (colored line), and solvent solution collected at one of the reference channels (black dashed). The smoothly sloping baseline in the spectra is dominated by the bend-libration combination band of  $\text{H}_2\text{O}$  and the CN vibration of ferri-ferrocyanide sits on top of the solvent at  $2115\text{ cm}^{-1}$  and  $2037\text{ cm}^{-1}$ , respectively. (b) Spectra after subtracting the spectra of the background solvent solution.

#### 5.4.2 Baseline correction

Baseline correction is necessary when the spectrum's baseline significantly deviates from the expected horizontal line. To apply appropriate correction techniques and obtain accurate spectral data, it is crucial to identify the underlying causes of baseline shifts. These shifts can be attributed to various factors, including:

1. **Instrumental factors:** Baseline shifts in a spectrum can be caused by instrumental factors, such as baseline drift, electronic noise, or variations in the detector response. These factors introduce a systematic offset in the measured signal, leading to a baseline shift. In our observations, we have found instrumental factors to be the dominant cause of baseline shifts in data collected using a laser as an infrared (IR) source.
2. **Sample-related factors:** Baseline shifts can also be caused by properties of the sample itself. Uneven thickness or a rough surface of the sample can lead to variations

in the measured signal and result in a baseline shift. In our microchannels, deformations due to bubbles in the photoresist film can contribute to uneven path lengths, resulting in baseline shifts.

3. **Environmental factors:** Changes in temperature, pressure, or atmospheric conditions can lead to baseline shifts in spectra due to their impact on the optical properties of the sample or the instrument. The Bruker vertex spectrometer is specifically designed to minimize the effects of environmental factors. However, in our microchannels, where we have limited control over these factors, baseline shifts can occur. For instance, the design of our microchannels includes a mixer that gradually widens to an observation channel, causing a drop in pressure, which can contribute to baseline shifts.
4. **Experimental artifacts:** Improper handling of the sample, misalignment of the spectrometer, or other experimental artifacts can introduce baseline shifts. In our specific experiments, we observed significant baseline shifts in the spectrum due to clipping of the IR beam with the 3D printed body, which was necessary for long-time spectra acquisition.

The correction process involves subtracting the baseline from the spectrum, aligning the band edges with the theoretical baseline (ideally 0% for absorption spectra or 100% for transmission). In this thesis, three different baseline correction techniques is presented and their utility is discussed.

## **Baseline correction using a linear offset**

In most of the experiments performed using the Bruker glow bar IR source, the baseline shift is minimal, and a simple correction method using a linear offset should suffice. The baseline shifts are common in spectra collected at late time delays and can be attributed to clipping

of the IR beam by the flow cell body. An example of such baseline shifts and correction by either adding or subtracting a linear offset is shown in Figure 5.3.

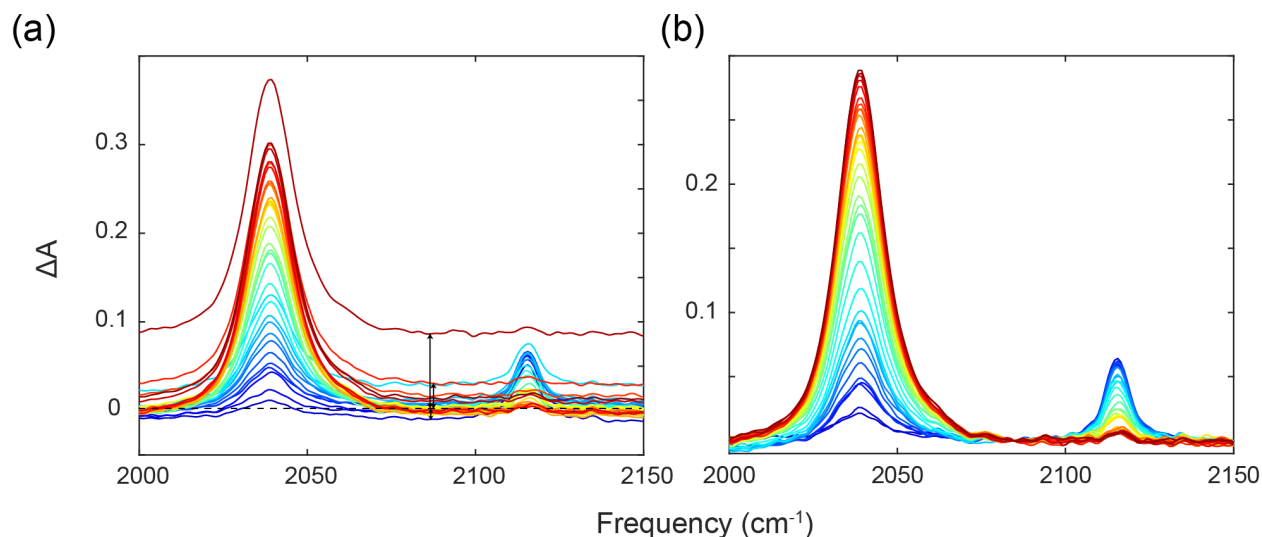


Figure 5.3: Illustration of a simple baseline correction using a linear offset. (a) The background subtracted transient FTIR absorption spectra between 2000-2150  $\text{cm}^{-1}$  as a function of mixing time delays from 0.1 ms (blue) to 35 ms (red). Residual baseline offsets, which we attribute to clipping of the beam by the flowcell bottom flange is evident at long delays. (b) Transient spectra after correcting for baseline shifts by subtracting/adding a linear offsets (black arrows) to match the change in absorbance at a frequency where there is no molecular absorption (2085  $\text{cm}^{-1}$  for this case).

## Baseline correction - Discrete wavelet transform

The discrete wavelet transform (DWT) is a powerful method for spectral baseline correction. Our research group has extensively utilized this method, developed by former student Paul Sanstead. Detailed information on the methodology, including the algorithm and wavelet basis selection, can be found in his thesis (page 100) [131].

We employed the DWT to correct baseline shifts in the transient absorption spectra obtained with the laser IR source. We observed significant baseline shifts in the experimental data collected with the laser IR source, which could not be adequately corrected using a linear offset. Therefore, the DWT approach was chosen for more effective baseline correction. An example of DWT is provided in Figure 5.4.

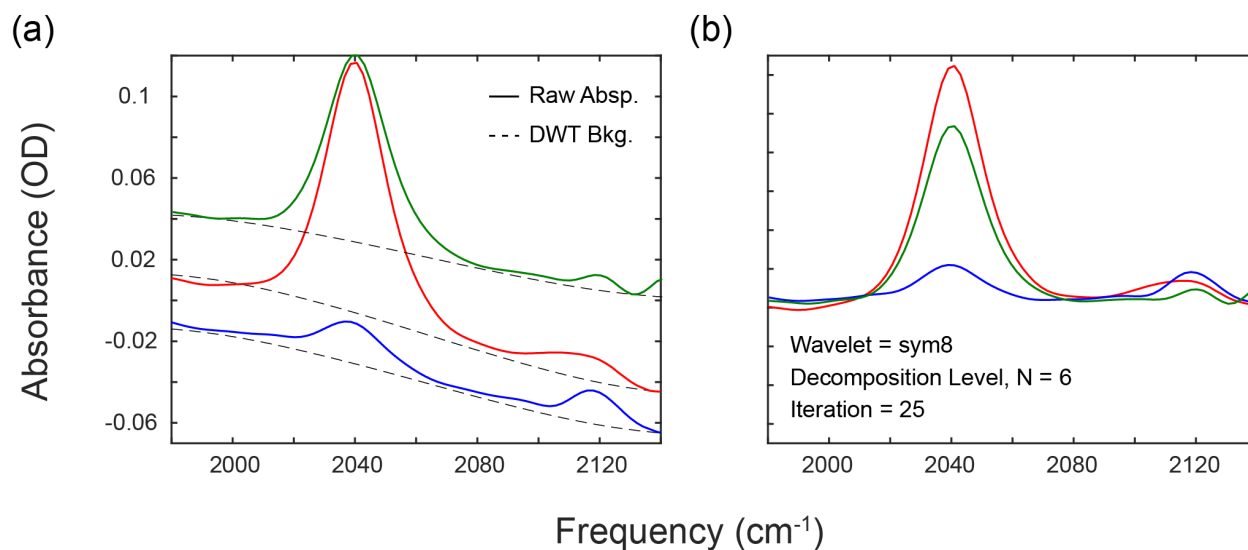


Figure 5.4: Illustration of baseline correction using DWT. (a) FTIR spectra collected at three different time points in a reduction of ferricyanide by ascorbic acid. The DWT method was used to construct an offset background (dashed black). (b) Spectra after DWT baseline correction, showing both the sloping and offset corrected effectively.

### 5.4.3 Comparison of baseline correction methods

Excessive data processing has the potential to introduce artifacts, which may ultimately undermine the accuracy and objectivity of spectral data interpretation. As a spectroscopist, it is imperative to emphasize the importance of minimal data processing to preserve the integrity of the original data. Many contemporary data acquisition software packages, such as Bruker OPUS, include built-in baseline correction methods, such as the rubberband baseline correction. To demonstrate the consequences of overcorrection, we present a visual comparison of the original data alongside several baseline correction schemes shown in Figure 5.5. This comparison highlights the impact of different correction approaches on the data. Notably, the DWT baseline correction method demonstrates superior performance by effectively correcting the baseline without overfitting the data. Conversely, the linear offset method proves inadequate for this dataset, as it results in an increased in peak  $\Delta OD$ , while the rubberband method excessively fits the data, leading to a decrease in  $\Delta OD$ .



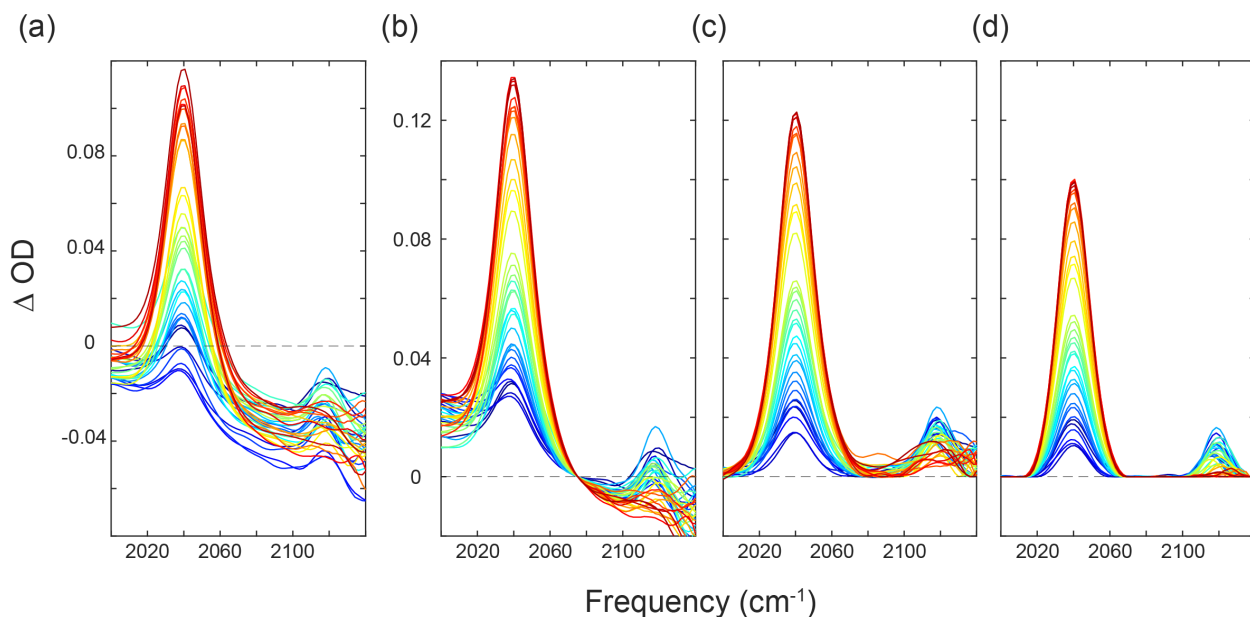


Figure 5.5: Comparison of baseline correction methods for the ferrocyanide reduction reaction. (a) Raw transient spectra showing incremental time delays (color gradient from blue to red). (b) Linear offset correction, which aligns the data at  $2075\text{ cm}^{-1}$  but does not correct the sloping baseline. (c) Discrete Wavelet Transform (DWT) correction, effectively correcting the sloping baseline with minimal change in absorbance. (d) Rubberband correction, resulting in over correction and reduction in  $\Delta OD$ .

## 5.5 Appendix

### 5.5.1 Data reproducibility

The method discussed in this chapter not only enables the extraction of valuable information from time-resolved spectroscopy experiments but also ensures the reproducibility of data collection. Figure 5.6 demonstrates the high reproducibility of the kinetic data obtained using the kinetic apparatus described in this thesis.

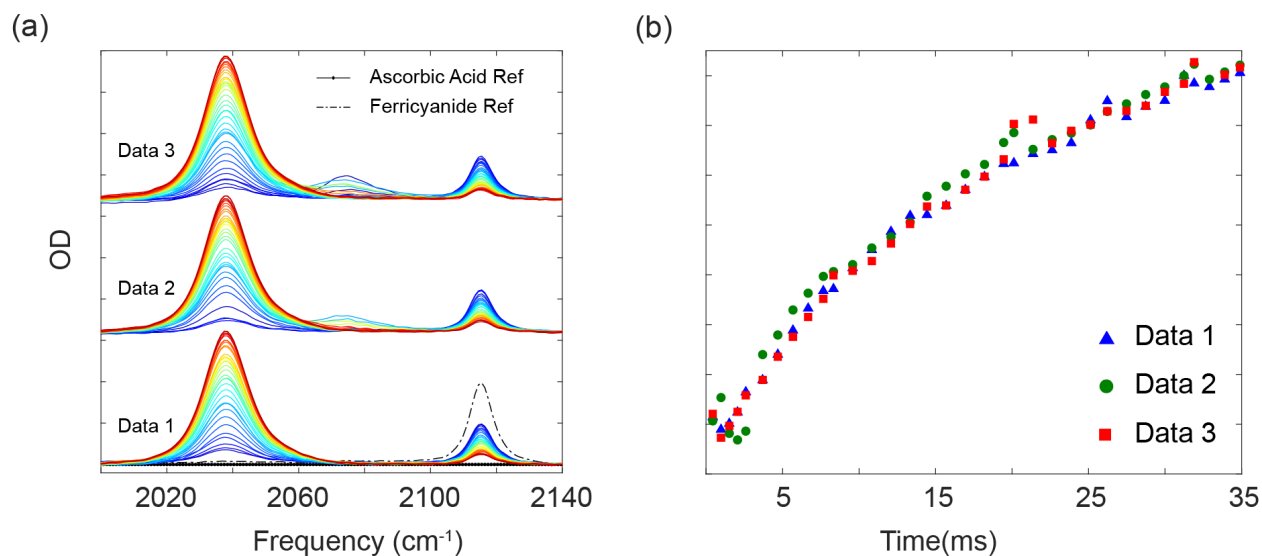


Figure 5.6: Illustration of data reproducibility. (a) Solvent-background subtracted and baseline-corrected spectra for the mixing of 0.1 M ascorbic acid with 25 mM potassium ferricyanide prepared in 0.1 M, pH 8 sodium phosphate buffer. The three data sets were obtained using the same micromixer and measurement parameters. In addition to the ferro and ferricyanide peaks, data 2 and 3 exhibit a peak at  $2075\text{ cm}^{-1}$ , which can be attributed to Prussian blue formation from residual ferrocyanide reacting with the fresh ferricyanide solution. (b) The corresponding kinetics show consistent growth of the ferrocyanide mode at  $2037\text{ cm}^{-1}$ , confirming the reproducibility of the kinetic data.

# CHAPTER 6

## DEMONSTRATING ABILITY TO PROBE MILLISECOND AND MICROSECOND KINETICS

### 6.1 Overview

Existing IR-compatible rapid mixing technology has made significant progress in enabling fast chemical mixing and measurements [86, 90, 93]. However, there remains a notable lack of emphasis and capability when it comes to probing kinetics with time resolution of milliseconds or better. The current focus in the field has primarily been on achieving rapid mixing and compatibility with IR spectroscopy, with less emphasis on accurately probing kinetics with such fine time resolution. This highlights the need for further advancements to effectively capture and characterize rapid molecular events, enhancing our understanding of fast chemical kinetics and its diverse applications in various fields.

In this chapter, we provide an overview of the performance of the IR mixer for fast chemical kinetics measurements. Specifically, we examine a model reaction involving the reduction of ferricyanide by ascorbic acid, which allows us to tune the reaction kinetics within the timescale range of milliseconds to microseconds by adjusting the pH. We propose strategies for extracting the relaxation rates from these measurements, employing fitting and normalization techniques. Additionally, we compare our experimental results with an existing theoretical model to validate the results of our experiments. Through this comparison, we discuss the significance of our findings in advancing the field of fast chemical kinetics measurements, addressing current limitations, and expanding our understanding of rapid molecular processes.

## 6.2 Ferricyanide reduction by ascorbic acid

The reduction of ferricyanide by ascorbic acid is excellent model reaction because it has a noticeable change in the absorption spectrum, indicating the progress of the reduction process. Ferricyanide solution is yellow with a narrow peak absorbance at 420-430 nm, while colorless ferrocyanide has a broader absorbance peak at 290-320 nm in the UV region. The reaction mechanism has been well-established, showing simpler kinetics and pH-dependent rates, making it popular for testing the performance of rapid mixers with UV/visible detection [132, 133, 134, 135, 136]. Additionally, the use of easily accessible and non-hazardous reagents, potassium ferricyanide and ascorbic acid, adds to the convenience of experimentation.

To our knowledge, there have been no previous reports on the kinetics investigation of this reaction using IR spectroscopy. However, the distinct  $C\equiv N$  stretch vibrations of ferricyanide and ferrocyanide ions make them suitable for investigation through IR spectroscopy [137, 138, 139]. Figure 6.1 shows the FTIR absorption spectra of 25 mM ferricyanide (red) and ferrocyanide (blue) in a solution of 0.5 M phosphate buffer at pH 6.6. The ferricyanide peak is centered at  $2115\text{ cm}^{-1}$  which upon reduction shifts to  $2037\text{ cm}^{-1}$ .

The observed red shift in the  $C\equiv N$  vibrational frequency upon reduction is due to back bonding, which involves the sharing of electron density from a metal center to a ligand's antibonding orbital [140]. This interaction influences the vibrational properties of metal-ligand complexes, especially those involving metal cyanides. The strength of back bonding are fundamentally dictated by the electronic properties of the metal center within these cyanide complexes. In particular, metal centers with greater electron-rich characteristics exhibit a higher propensity for effective back bonding to the nitrile carbon, which in turn weaken the  $C\equiv N$  vibration [141]. This manifests as lower  $C\equiv N$  stretching frequency in infrared spectrum.

The variation in peak absorbance of two modes can be attributed to the difference in

molar extinction coefficients between the ferrocyanide mode ( $4.24 \times 10^3 \text{ M}^{-1} \text{ cm}^{-1}$ ) and the ferricyanide mode ( $1.18 \times 10^3 \text{ M}^{-1} \text{ cm}^{-1}$ ). The ratio of transition dipole strength between the ferrocyanide and ferricyanide modes, determined from calculating the integrated IR peak area is 7:1. This ratio aligns with values reported in the existing literature for these species, providing further validation of this model system [142, 143, 138].

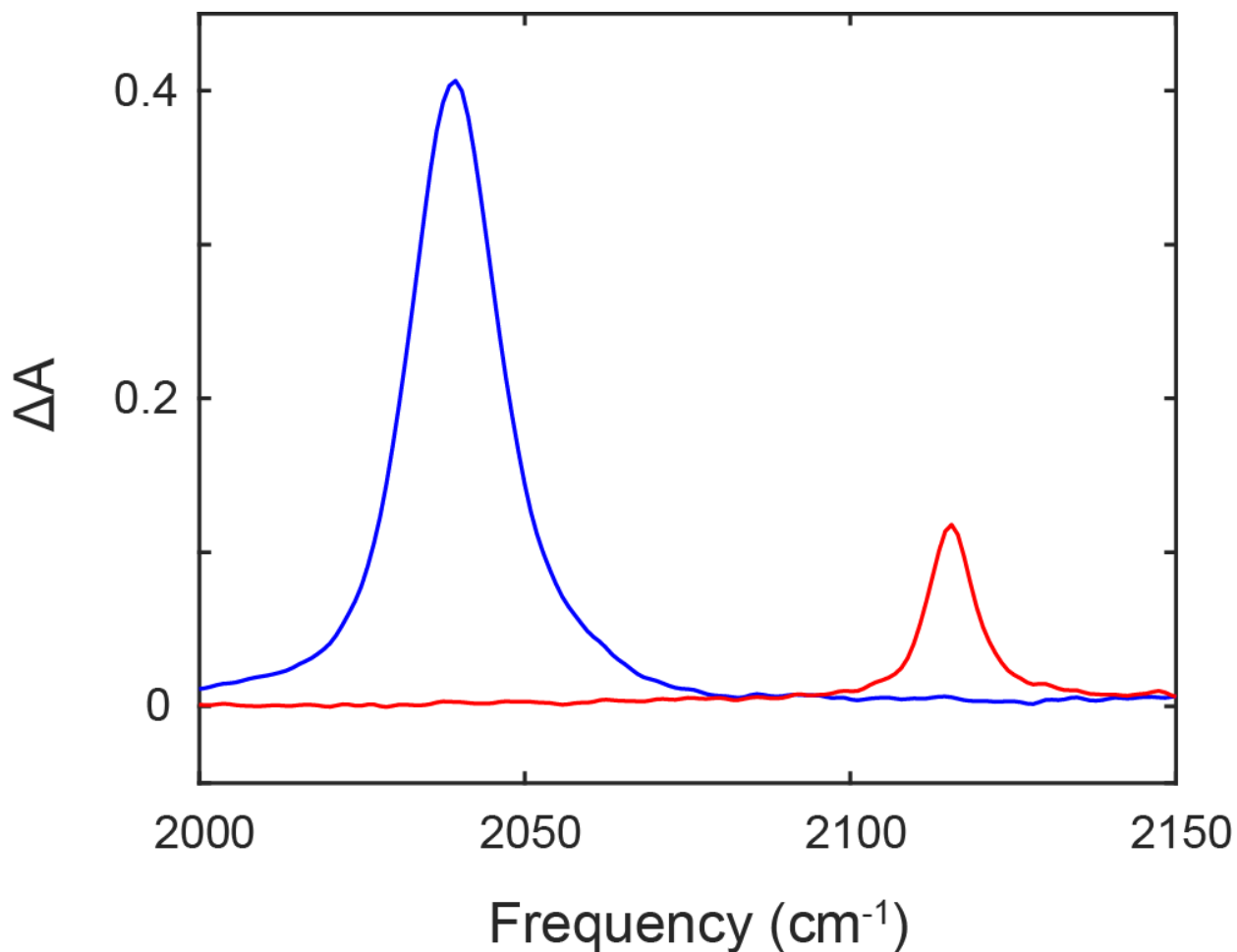
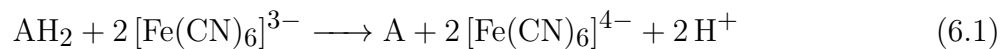


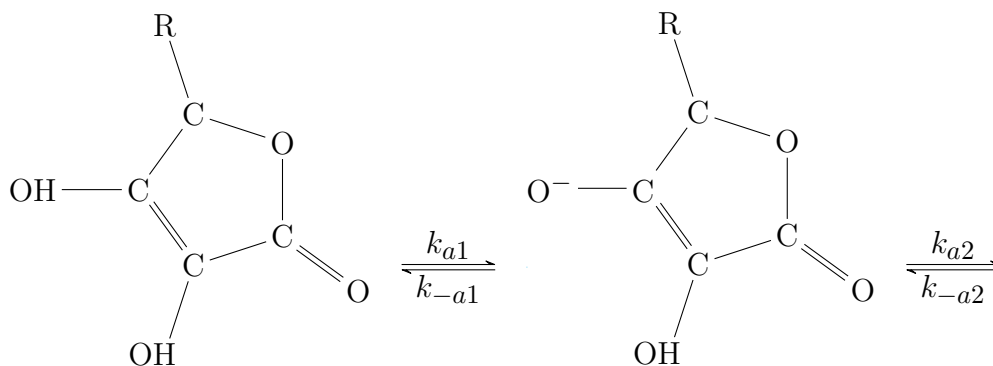
Figure 6.1: Equilibrium FTIR absorption spectra of 25 mM ferricyanide (red) and ferrocyanide (blue). The ferricyanide mode is centered at  $2115 \text{ cm}^{-1}$  with a full width at half maximum (FWHM) bandwidth of  $9 \text{ cm}^{-1}$ . The ferrocyanide mode is centered at  $2037 \text{ cm}^{-1}$ , with a FWHM bandwidth of  $17 \text{ cm}^{-1}$ .

### 6.2.1 Reaction mechanism

The net reaction scheme originally described by Erdey and Svehla [144] is given by

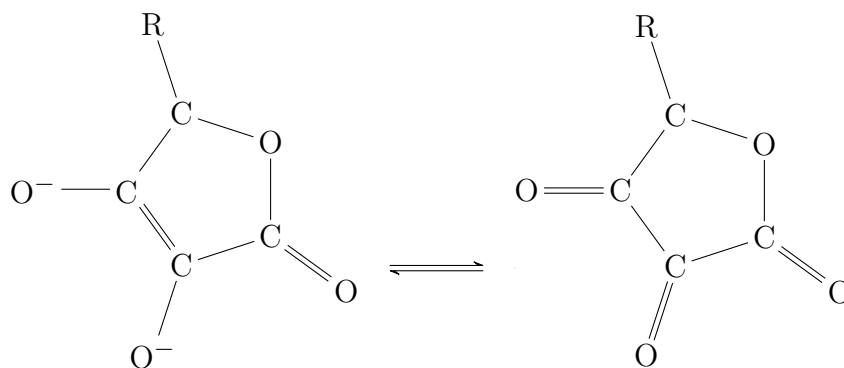


where  $\text{AH}_2$  represents the ascorbic diacid and A is dehydroascorbic acid. Various forms of ascorbic acid are shown below, where R represent  $\text{OHCH}-\text{CH}_2\text{OH}$  :



Ascorbic acid ( $\text{AH}_2$ )

Ascorbate anion ( $\text{AH}^-$ )

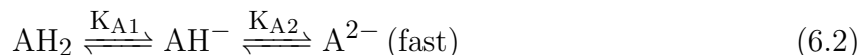


Ascorbate di-anion ( $\text{A}^{2-}$ )

Dehydro-ascorbic acid (A)

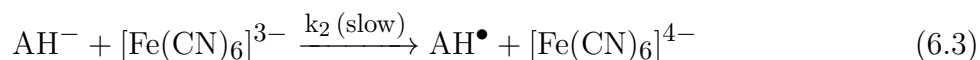
The reaction mechanism, which is a detailed sequence of elementary reactions that contribute to the overall reaction is understood to be a multi step process involving the ascorbic acid/base equilibria and an ascorbate free radical intermediate [132, 133].

First, let's look into the ionization of ascorbic acid into ascorbate anion ( $AH^-$ ) and ascorbate dianion ( $A^{2-}$ ) in a reversible process.



In equation 6.2,  $K_{A1}$  and  $K_{A2}$  represent the equilibrium constants for the dissociation of ascorbic acid and ascorbate anion, respectively. These constants quantitatively express the extent of ionization of the acid and its anion and are determined from titration experiments of ascorbic acid using an oxidizing agent such as iodine. The dissociation constants  $K_{A1}$  and  $K_{A2}$  of ascorbic acid at room temperature have been reported in the literature to be in the order of  $6.7 \times 10^{-5}$  M and  $3.1 \times 10^{-12}$  M [145, 136, 146]. It's important to note that the specific values of  $K_{A1}$  and  $K_{A2}$  can vary depending on factors such as temperature, solvent, and ionic strength.

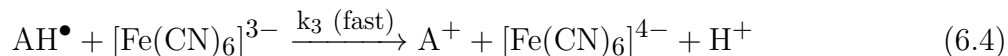
In the initial step of the reaction, the intermediate anion  $AH^-$  is subjected to attack by ferricyanide in a slow and rate-determining process, resulting in the formation of ascorbate free radical ( $AH^\bullet$ ) and ferrocyanide.



As the overall reaction can only proceed as fast as its slowest step, this particular step plays a crucial role in determining the reaction rate. Moreover, this shows that rate of the reaction is greatly influenced by pH since the degree of protonation of ascorbic acid experiences significant changes with varying pH levels.

The ascorbate free radical is a reactive species and immediately reacts with a fresh fer-

ricyanide to reduce it to ferrocyanide.



This intermediate dianion,  $\text{A}^{2-}$ , is attacked by ferricyanide to produce ascorbate anion free radical ( $\text{A}^{-\bullet}$ ) and ferrocyanide.



Finally, ( $\text{A}^{-\bullet}$ ) reacts immediately with fresh ferricyanide to give ferrocyanide and dehydroascorbic acid.



### 6.3 Rate law and kinetic model

A rate law is a mathematical expression that describes the relationship between the rates of chemical reactions and the concentrations of reactants. The rate law for this reaction is expressed as follows:

$$-\frac{d[\text{Fe}(\text{CN})_6^{3-}]}{dt} = k [\text{Fe}(\text{CN})_6^{3-}][\text{A}]_0 \quad (6.7)$$

Equation 6.7 indicates that the reaction is second order overall, with first-order dependence on concentration of both  $[\text{Fe}(\text{CN})_6^{3-}]$  and  $[\text{A}]_0$ . The quantity  $k$  is the rate constant. The notation  $[\text{A}]_0$  is employed to signify the presence of various forms of ascorbic acid within the aqueous solution. This collective representation is intended to encompass the entities  $[\text{AH}_2]$ ,  $[\text{AH}^-]$ , and  $[\text{A}^{2-}]$  since multiple forms of ascorbic acid could potentially be present. This relationship can be expressed mathematically as  $[\text{A}]_0 = [\text{AH}_2] + [\text{AH}^-] + [\text{A}^{2-}]$  and can be further expanded in terms of the acid dissociation constants as:



$$\begin{aligned}
[\text{AH}^-] &= \frac{K_{A1}[\text{AH}_2]}{[\text{H}^+]} \\
[\text{A}^{2-}] &= \frac{K_{A2}[\text{AH}^-]}{[\text{H}^+]}
\end{aligned}
\tag{6.8}$$

Substituting these relationships into the equation for  $[\text{A}]_0$ , we arrive at the following equation:

$$[\text{AH}_2] = \frac{1}{\left(1 + \frac{K_{A1}}{[\text{H}^+]} + \frac{K_{A1}K_{A2}}{[\text{H}^+]^2}\right)} [\text{A}]_0
\tag{6.9}$$

Now, to derive  $k$ , we start by writing the mechanistic rate equations for  $[\text{Fe}(\text{CN})_6^{3-}]$ ,  $[\text{AH}^\bullet]$  and  $[\text{A}^{-\bullet}]$  as:

$$\begin{aligned}
-\frac{d[\text{Fe}(\text{CN})_6^{3-}]}{dt} &= k_2[\text{Fe}(\text{CN})_6^{3-}][\text{AH}^-] \\
&\quad + k_3[\text{Fe}(\text{CN})_6^{3-}][\text{AH}^\bullet] \\
&\quad + k_4[\text{Fe}(\text{CN})_6^{3-}][\text{A}^{2-}] \\
&\quad + k_5[\text{Fe}(\text{CN})_6^{3-}][\text{A}^{-\bullet}]
\end{aligned}
\tag{6.10}$$

$$\frac{d[\text{AH}^\bullet]}{dt} = k_2[\text{Fe}(\text{CN})_6^{3-}][\text{AH}^-] - k_3[\text{AH}^\bullet][\text{Fe}(\text{CN})_6^{3-}]
\tag{6.11}$$

$$\frac{d[\text{A}^{-\bullet}]}{dt} = k_4[\text{Fe}(\text{CN})_6^{3-}][\text{A}^{2-}] - k_5[\text{A}^{-\bullet}][\text{Fe}(\text{CN})_6^{3-}]
\tag{6.12}$$

Invoking the steady state approximation on the radical species, we can express  $[\text{AH}^\bullet]$  and  $[\text{A}^{-\bullet}]$  as follows:

$$[\text{AH}^\bullet] = \frac{k_2[\text{AH}^-]}{k_3}
\tag{6.13}$$

$$[A^{-\bullet}] = \frac{k_4[A^{2-}]}{k_5} \quad (6.14)$$

Substituting for  $[AH^{\bullet}]$  and  $[A^{-\bullet}]$  into equation 6.10 gives:

$$-\frac{d[\text{Fe}(\text{CN})_6^{3-}]}{dt} = \left( \frac{2k_2K_{A1}}{[H^+]} + \frac{2k_4K_{A2}K_{A1}}{[H^+]^2} \right) [\text{Fe}(\text{CN})_6^{3-}][AH_2] \quad (6.15)$$

After several algebraic steps and substituting the relation given by equation 6.9, we obtain the following equation:

$$-\frac{d[\text{Fe}(\text{CN})_6^{3-}]}{dt} = \left( \frac{2(k_2 + \frac{k_4K_{A2}}{[H^+]})}{1 + \frac{[H^+]}{K_{A1}} + \frac{K_{A2}}{[H^+]}} \right) [\text{Fe}(\text{CN})_6^{3-}][A]_0 \quad (6.16)$$

Therefore,  $k$  can be expressed as follows:

$$k = \frac{2(k_2 + \frac{k_4K_{A2}}{[H^+]})}{1 + \frac{[H^+]}{K_{A1}} + \frac{K_{A2}}{[H^+]}} \quad (6.17)$$

The Equation 6.17 provide a theoretical model for the pH dependence of the overall second-order rate constant. The model has been reported to work well in the pH range 1-8.5 [133]. This reaction has not been extensively studied at alkaline pH because the reaction is expected to occur within the timescale of hundreds of microseconds, surpassing the time resolution capabilities of typical stopped flow mixers.

The empirical rate constants,  $k_2$  and  $k_4$ , can be determined by fitting the experimental data to the model. An alternative approach involves assessing the rate constant  $k$  under conditions of low pH. In this scenario, equation 6.17 simplifies to  $k = \frac{2k_2}{1 + \frac{[H^+]}{K_{A1}}}$ . By utilizing known values for  $[H^+]$  and  $K_{A1}$  and the measured rate  $k$ , the value of  $k_2$  can be derived. These empirical rate constants  $k_2$  and  $k_4$  have been previously documented as  $4.58 \times 10^2 \text{ M}^{-1}\text{s}^{-1}$  and  $6.02 \times 10^6 \text{ M}^{-1}\text{s}^{-1}$ , respectively [132, 133]. These constants will play a crucial role in validating our experimental findings.

### 6.3.1 *pH dependence of the reduction rate*

The kinetic rates of this reaction is expected to vary with pH as follows:

**Acidic (pH < 7):** Under acidic conditions, the reaction rate is limited by the higher concentration of hydronium ions ( $\text{H}^+$ ). In equation 6.3 the reverse reaction is favorable and therefore limits the availability of the active reactant species  $\text{AH}^-$ . As a result, the reaction rate is expected to be relatively slow with relaxation times reported in the range of several minutes in the literature [133].

**Neutral conditions (pH = 7):** Under neutral conditions, the reaction rate is expected to be faster than under acidic conditions, but slower than under basic conditions. This is because the ascorbic acid molecule is only partially ionized and exists in both ionic and non-ionic forms. The reaction is expected to follow second-order kinetics with respect to both the ferricyanide ion and ascorbic acid. Relaxation time in several tens of millisecond have been reported in the literature, which made it a popular choice in testing the performance of stopped flow mixing apparatus [136, 132, 133]

**Basic conditions (pH > 7):** Under basic conditions, the reaction rate is expected to be the fastest because the ascorbic acid molecule is mostly ionized and exists mainly in its highly reactive anionic forms,  $\text{AH}^-$  and  $\text{A}^{2-}$ .

It is worth noting that previous studies of this reaction have employed a pseudo first-order treatment to simplify the kinetic analysis. This approach involves maintaining a higher concentration of ascorbic acid compared to ferricyanide, typically with the concentration of ferricyanide kept at 5-10% of the concentration of ascorbic acid [132, 133, 134, 135]. In spectroscopic techniques, such as IR and UV/Vis spectroscopy, the required concentrations can vary. In the case of IR spectroscopy, the typical concentration needed is in the tens of millimolar range, which is an order of magnitude higher than that required for UV/Vis spectroscopy. This difference arises because IR spectroscopy relies on vibrational transitions that

generally have lower molar absorptivities compared to the electronic transitions measured in UV/Vis spectroscopy. In the context of the reduction experiment discussed in this thesis, a concentration of 25 mM for ferricyanide and 100 mM for ascorbic acid. Both solutions are prepared in a 0.5 M potassium phosphate buffer at pH varying from 4 to 12. The variation of pH enables the smooth modulation of kinetics across the micro-to-millisecond timescale.

## 6.4 Time-Resolved FTIR kinetics of the reduction reaction

Figure 6.2 displays the raw transient FTIR absorption spectra between 2000-2150  $\text{cm}^{-1}$  as a function of time delays, ranging from 0.2 ms (blue) to 20 ms (red), illustrating a kinetic measurement of the reduction reaction using IR spectroscopy.

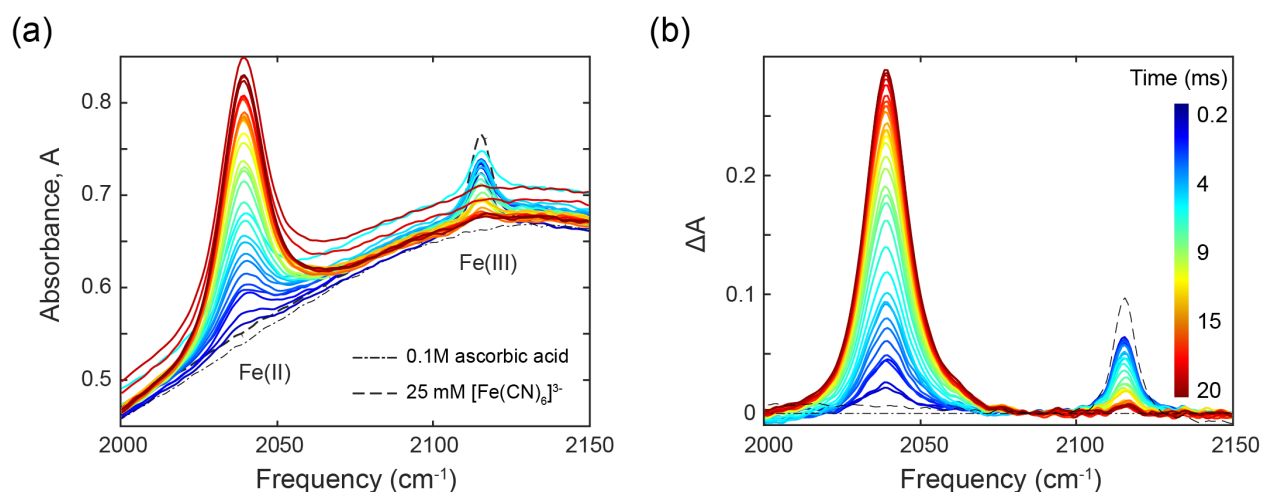


Figure 6.2: Potassium ferricyanide reduction kinetics. (a) Raw transient FTIR absorption spectra in the CN stretching region at time delays from 0.2 ms (blue) to 20 ms (red) for pH 6.6 with reference spectra at the inlets of ferricyanide (dashed) and ascorbic acids (dash-dotted). (b) The same spectra following background subtraction and baseline correction. The colorbar indicates the temporal progression of the reaction.

A smoothly sloping baseline in the spectra is dominated by the bend-libration combination band of  $\text{H}_2\text{O}$ , and the CN stretch vibrations of the ferro- and ferricyanide ions are observed as sharper peaks on top of this background at 2037  $\text{cm}^{-1}$  and 2115  $\text{cm}^{-1}$  respectively (Figure 6.2 a). This solvent background is corrected by subtracting the spectra of the

ascorbic acid solution collected at one of the reference channels (dash-dotted, Figure 6.2 a ). Any residual baseline offsets, possibly from clipping of the beam by the flow cell bottom flange at long delays, are corrected by subtracting a linear offset to match at a frequency where there is no molecular absorption ( $2085\text{ cm}^{-1}$  for this case). Figure 6.2 b shows the resulting processed absorption spectra. The temporal evolution of the spectra follows growth of the ferrocyanide mode at  $2037\text{ cm}^{-1}$  and the decay of the ferricyanide mode at  $2115\text{ cm}^{-1}$ . At the earliest mixing delay, the ferricyanide absorbance is almost halved relative to the inlet due to dilution upon mixing, and some ferrocyanide is already present, indicating the extent of reduction up to the first detection point. To extract the kinetic traces, we have the option of either using the peak absorption values of each mode or calculating the area under the curve. We have observed minimal differences between these methods, so for the sake of simplicity, we will employ the peak absorption values in our analysis.

Figure 6.3 a and b illustrates the time-dependence of the peak absorption for ferrocyanide ( $2037\text{ cm}^{-1}$ ) and ferricyanide ( $2115\text{ cm}^{-1}$ ) modes at various pH conditions, respectively. The data and fitted curves demonstrate that the relaxation process for both peaks follows the expected exponential growth and decay kinetics with a similar time constant.

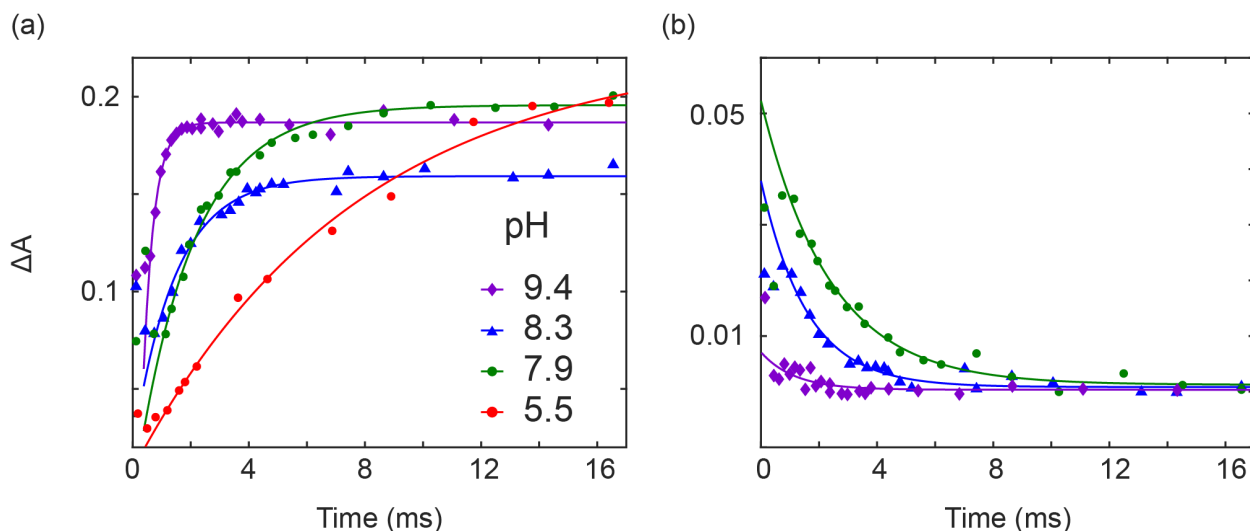


Figure 6.3: Time-dependent peak absorbance for the ferrocyanide (a) and ferricyanide (b) vibrations for pH 5.5, 7.9, 8.3, 9.4. The variations in the measured absorbance can be attributed to sample preparation, and path length variations of the microchannel. The ferricyanide mode for pH 5.5 is excluded from the plot due to high noise level in the data.

In a slightly acidic condition (pH 5.5), a kinetic process is observed to exhibit an exponential rise over time. However, the process has not yet achieved a baseline level within the duration of our observations, indicating that our instrument's time window may not be sufficient to capture the complete kinetics. The corresponding decay of ferricyanide mode at this pH is not shown due to noisy data. In slightly basic conditions (pH 7.9, 8.3), a similar exponential rise and decay is observed within the instrument's time window/resolution, suggesting that the instrument is well-suited for measuring kinetics within the range of 1-10 ms. At pH 9.4, the rise and decay occurs within the first few measurement points, indicating that the reaction rate is too fast to be measured with the current time resolution. Additionally, variations in absorption across different pH measurements (most notable in 6.3 a) suggest differences in baseline values, which are common and can be attributed to factors such as variations in sample concentration during preparation, path length, and micromixer orientation. To extract kinetic parameters from such data, a proper fitting and normalization scheme is necessary.

### 6.4.1 Fitting and normalization scheme

The absorption growth and decay of ferrocyanide and ferricyanide were simultaneously fitted using the MATLAB `lsqcurvefit` optimization routine. Both equations 6.18 and 6.19 were employed to fit the data, representing the exponential functions for ferrocyanide and ferricyanide, respectively. The simultaneous fitting approach provides a more comprehensive analysis, capturing the relaxation kinetics of both the reactant and product, compared to fitting the data independently. This is one notable advantage of measuring kinetics with IR spectroscopy because it allows simultaneous measurement of both decay of the reactant and growth of the product.

$$A(t) = A_{\infty}(1 - e^{-kt}) + A_0 \quad (6.18)$$

$$a(t) = a_0e^{-kt} + a_{\infty} \quad (6.19)$$

The chosen exponential functions allow for direct assessment of the end behavior from the fits. At  $t = 0$  and  $t = \infty$ , equation 6.18 yields the values  $A_0$  and  $A_{\infty}$ , while Equation 6.19 yields the values  $a_{\infty}$  and  $a_0$ . These values correspond to the upper baseline  $A_{\infty}$  (depicted by the blue dashed line) and the time zero value (depicted by the red dashed line) shown in Figure 6.4 a.

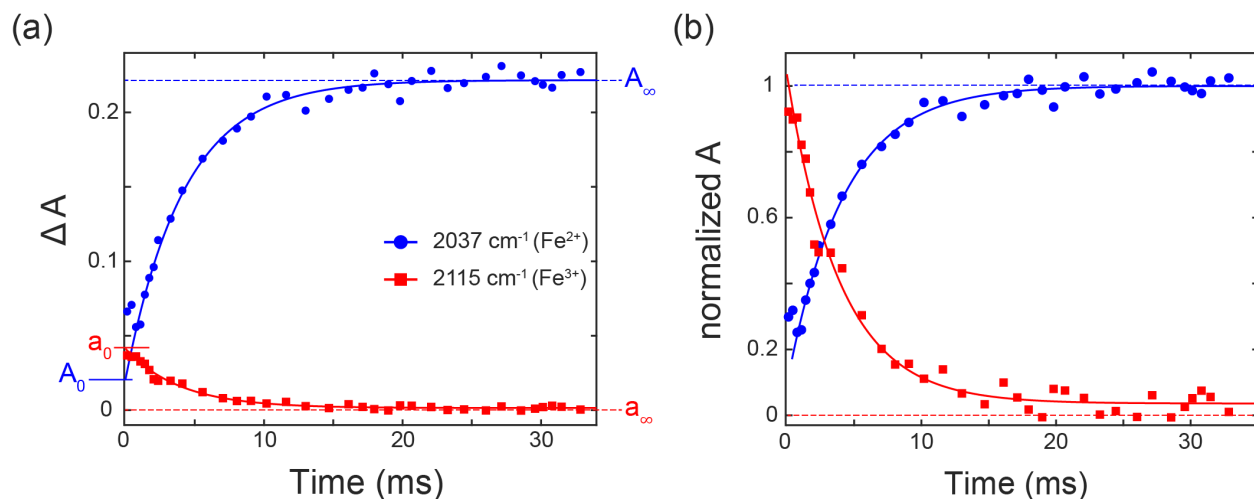


Figure 6.4: Example of fitting and normalization schemes used to extract kinetic parameters. (a) Time-dependent peak absorbance for ferricyanide (red) and ferrocyanide (blue) vibrations at pH 7.7, fitted with exponential functions to extract baselines ( $A_\infty$ ,  $a_\infty$ ) and time zero absorbance values ( $A_0$ ,  $a_0$ ). (b) Normalized time-dependent peak absorbance using time zero and baseline values.

To normalize the data, we applied the normalization scheme outlined in Equations 6.20 and 6.21. The normalized absorbance, along with the corresponding fits, is illustrated in Figure 6.4 b. The initial two data points corresponding to time delays less than 0.5 ms were excluded from the fitting process due to their deviation from the rest of the data.

$$\text{Fe}^{2+}(t) = \frac{A(t) - A_0}{A_\infty - A_0} \quad (6.20)$$

$$\text{Fe}^{3+}(t) = \frac{a(t) - a_\infty}{a_0 - a_\infty} \quad (6.21)$$

This method is extended to data collected at different pH conditions, and the normalized peak absorbance for ferrocyanide and ferricyanide are shown in Figure 6.5 a and b, respectively. To be consistent with the analysis, the initial two data points are excluded for all data.



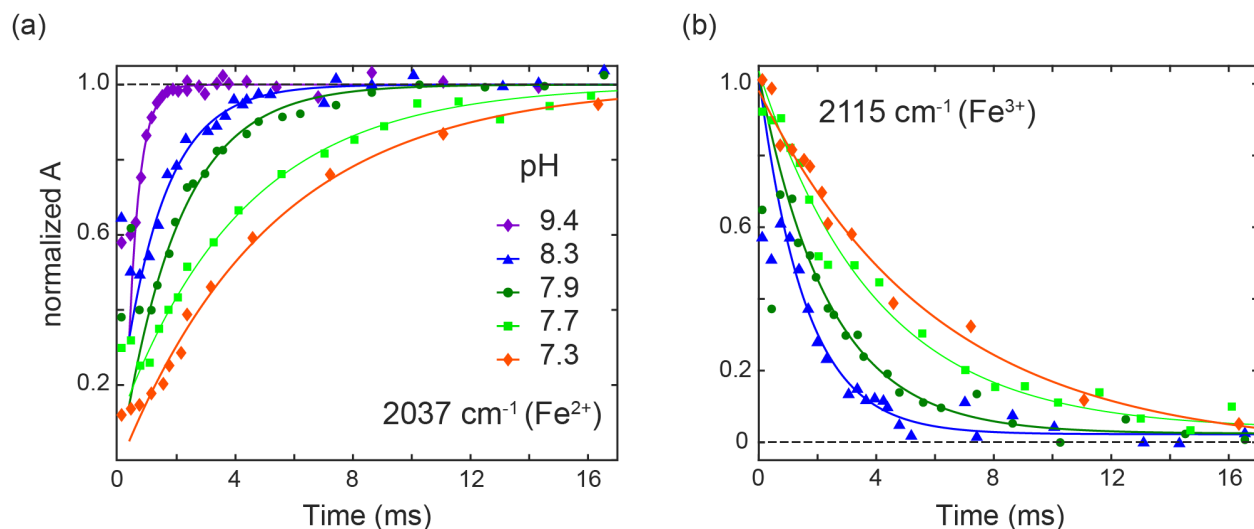


Figure 6.5: Time-dependent peak absorbance for the ferrocyanide (a) and ferricyanide (b) vibrations for pH 5.5, 7.9, 8.3, 9.4. The kinetic traces of ferrocyanide mode at pH 9.4 have already grown within the first ten measurement points indicating that the reaction rate is too fast and at the limit of the current time resolution of the device.

The values of relaxation rate constant ( $k_{obs}$ ) and relaxation time ( $\tau_{obs}$ ) obtained from the normalized fittings for different pH conditions is summarized in Table 6.1.

Solution pH			Relaxation Kinetics	
<i>Mixed pH</i>	<i>Ascorbic Acid pH</i>	<i>Ferricyanide pH</i>	$k_{obs}(s^{-1})$	$\tau_{obs}(ms)$
9.4	8.3	11.4	2650	0.4
8.3	7.9	10.7	680	1.5
7.9	7.7	8.9	500	2.0
7.7	7.5	8.3	240	4.2
7.3	7.1	7.7	190	5.2
6.6	6.5	7.0	130	7.9
4.2	4.0	5.5	50	20

Table 6.1: Summary of pH-dependent reduction kinetics. Measured pH of the initial input AA and ferricyanide solutions and the equilibrated final mixed solution are shown together with the pH dependent observed relaxation rate constants and relaxation times, ( $k_{obs}$ ) and relaxation times ( $\tau_{obs} = k_{obs}^{-1}$ ).

### 6.4.2 Validation of the relaxation rates

To validate our experimental results, we constructed a pH-dependent plot of the second-order rate constants, as shown in Figure 6.6a. By fitting the data to equation 6.17 (illustrated by the magenta line), we determined the empirical rate constants  $k_2$  and  $k_4$  to be  $6 \pm 1 \times 10^2 \text{ M}^{-1}\text{s}^{-1}$  and  $4.3 \pm 0.7 \times 10^6 \text{ M}^{-1}\text{s}^{-1}$ , respectively. These values are in well agreement with the previously reported values [133]. In summary, our instrument proves proficient in kinetic measurements within the pH range of 4-9, effectively resolving reaction kinetics with relaxation times in the range of 1 ms to 20 ms.

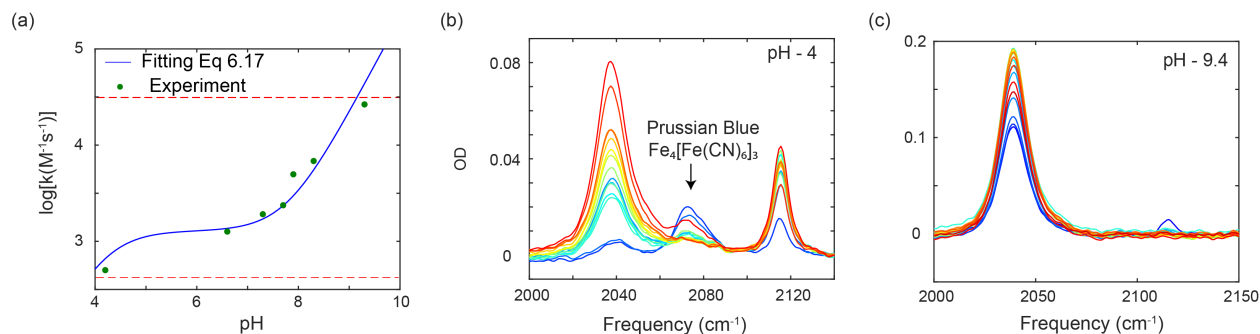


Figure 6.6: (a) Experimentally determined relaxation rate constants (green circle) plotted against pH and fitted to the Equation 6.17 (blue line) for validation of the experimental results. The dashed red lines represent the upper and lower bounds of the measurable rate constant. (b) Transient FTIR spectra captured during the reduction reaction at pH 4. The experiment was halted due to the formation of a precipitate, the prussian blue complex, marked by an absorption peak at  $2072 \text{ cm}^{-1}$ . (c) Transient FTIR spectra captured during the reduction reaction at pH 9. The reduction reaction is complete within the first few measurement points, illustrating the measurement's  $\log(k)$  limitation above 4.5.

However, beyond pH 9, the device's current time resolution limits its accuracy, as evidenced by the kinetic trace of the ferrocyanide peak in Figure 6.5 (purple line), which exhibits the exponential growth of ferrocyanide mode within the first few measurement points. The transient FTIR spectra is shown in Figure 6.6c. Similarly, below a pH of 4, the reduction rates are slower and cannot be measured due to the 20 ms time window limitations imposed by the current design of the observation channel. Previous studies by Tonomura *et al.* using the fluorescence stopped-flow method reported relaxation rates ranging from hundreds of

milliseconds at pH 4 to 30 seconds at pH 1. In our IR experiments, we also observed a competing reaction occurring at low pH values between the reduced ferrocyanide complex and the ferric ion. This led to the formation of prussian blue, which exhibit an infrared absorption peak at  $2072\text{ cm}^{-1}$ , as depicted in Figure 6.6b.

The presence of prussian blue formation may account for the significantly slower observed reaction rates reported by Tonomura *et al.* at low pH values. Additionally, even if we could extend the time window of observation, performing reactions at low pHs is challenging due to the insoluble nature of prussian blue. We observed that this complex clogged the microchannel resulting in flow obstruction and damage to the mixer.

## 6.5 Demonstration of microsecond kinetic process using a laser based IR source

In the preceding sections, the data suggests the uncertainty associated with the measuring the relaxation kinetics becomes prominent for time scales starting at approximately 1 ms. To improve this by an order of magnitude, we need to implement methodologies to enhance the time resolution.

In Chapter 3, we noted that in the context of "serpentine/inchworm" designs, the width of the observation channel as well as the dimensions of the IR probe act as limiting factors to achieving optimal time resolution. A significant improvement in time resolution can be achieved through a tightly focused beam on a narrow channel. For instance, the reduction of the IR beam's focus spot size (FWHM) from  $200\text{ }\mu\text{m}$  to  $12\text{ }\mu\text{m}$  holds the potential to enhance the temporal resolution by a factor of 100. Similarly, by decreasing the width of the observation channel from  $300\text{ }\mu\text{m}$  to  $80\text{ }\mu\text{m}$ , while keeping the flow rate constant, a comparable enhancement in resolution by approximately 100-fold can be realized. The cumulative outcome of these optimizations would translate into measurement of relaxation kinetics with an order of magnitude reduction in the uncertainty compared to the outcomes

we have attained thus far.

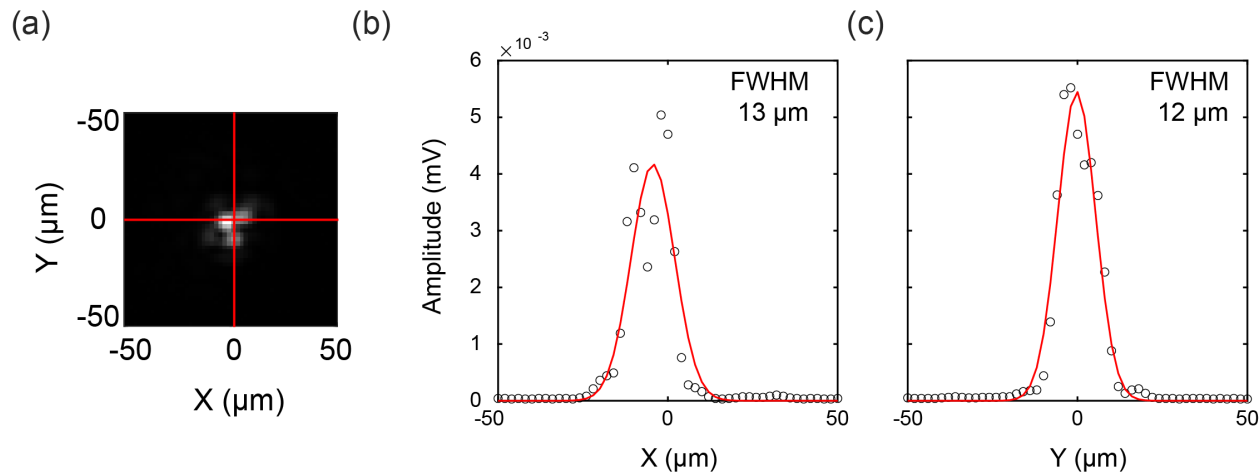


Figure 6.7: IR probe beam characterization. (a) Grayscale image of the IR intensity from a pinhole scan in the focal plane ( $Z = 0$ ). (b-c) The IR intensities (black circles) from a  $5 \mu\text{m}$  pinhole scan at the focal plane with Gaussian fit (red). The FWHM along the X and Y directions are  $13 \mu\text{m}$  and  $12 \mu\text{m}$ , respectively.

In our pursuit of achieving such enhanced resolution, we employed a tightly focused infrared source from a tunable mid-IR optical parametric amplifier (OPA) with a 1 MHz 1033 nm fiber laser pump source. The size of the IR focus at the sample plane was determined by measuring the transmission through a  $5 \mu\text{m}$  pinhole which is raster scanned across the beam, Figure 6.7. The pinhole was mounted between two 1 mm thick  $\text{CaF}_2$  windows to mimic the sample profile. This measurement is possible because of motorized stage capable of repeatable micro-positioning in the XY plane. The measured beam size represents the actual beam size convoluted with the  $5 \mu\text{m}$  pinhole. Further detailed characterization of the beam can be found elsewhere [147].

In Figure 6.7 (b-c), the amplitude corresponding to the X and Y cross-sections are depicted, resulting in a full width at half maximum (FWHM) of  $13 \mu\text{m}$  and  $12 \mu\text{m}$ , respectively. Taking the average of these cross-sections, we consider a beam size of  $12.5 \mu\text{m}$  FWHM for our analysis.

### 6.5.1 Raw kinetic data with laser IR source

The acquisition of raw kinetic data using the laser-based IR probe follows a similar measurement procedure to that of the glowbar source, with a difference in recording the solvent background measurement. To ensure a stable baseline in the absorption spectra, the background were collected at each measurement point. The laser source is sensitive to scattering compared to the glowbar, potentially leading to variations in the baseline.

Figure 6.8 illustrates the raw and processed data for the reduction reaction at pH 8.5. Starting with the sample IR intensities in Figure 6.8 (a), these are then subtracted from the background solvent intensities depicted in Figure 6.8 (b), resulting in the raw absorbance shown in Figure 6.8 (c). To address any baseline shifts present in the data, a discrete wavelet method is implemented. The application of this method is illustrated in Figure 6.8 (d) to effectively correct for any baseline fluctuations.

### 6.5.2 Fitting and normalizing the kinetic data

Figure 6.9 illustrates both the raw and normalized time-dependent absorbance profiles for ferrocyanide (blue) and ferricyanide modes (red), accompanied by their respective exponential fits. The raw data was acquired by taking the peak absorbance of each mode. The fitting and normalization procedures are based on equations 6.18, 6.19, 6.20, and 6.21. The fitting for the ferricyanide mode exhibits sub-optimal performance, which can be attributed to the high noise level within the ferricyanide mode present in the absorption spectra. A potential strategy to enhance the quality of the data involves tuning the OPA settings to align the center frequency of the IR beam more closely with  $2115\text{ cm}^{-1}$ . Despite this challenge, the ferrocyanide mode effectively captures the underlying kinetics, enabling us to extract the kinetic parameters. By employing this setup, we can expect the time resolution of  $50\text{ }\mu\text{s}$ , while performing measurement at a flow rate of  $0.3\text{ mL/min}$ . As a result, we can now measure the reduction reaction at pH greater than 8.5.

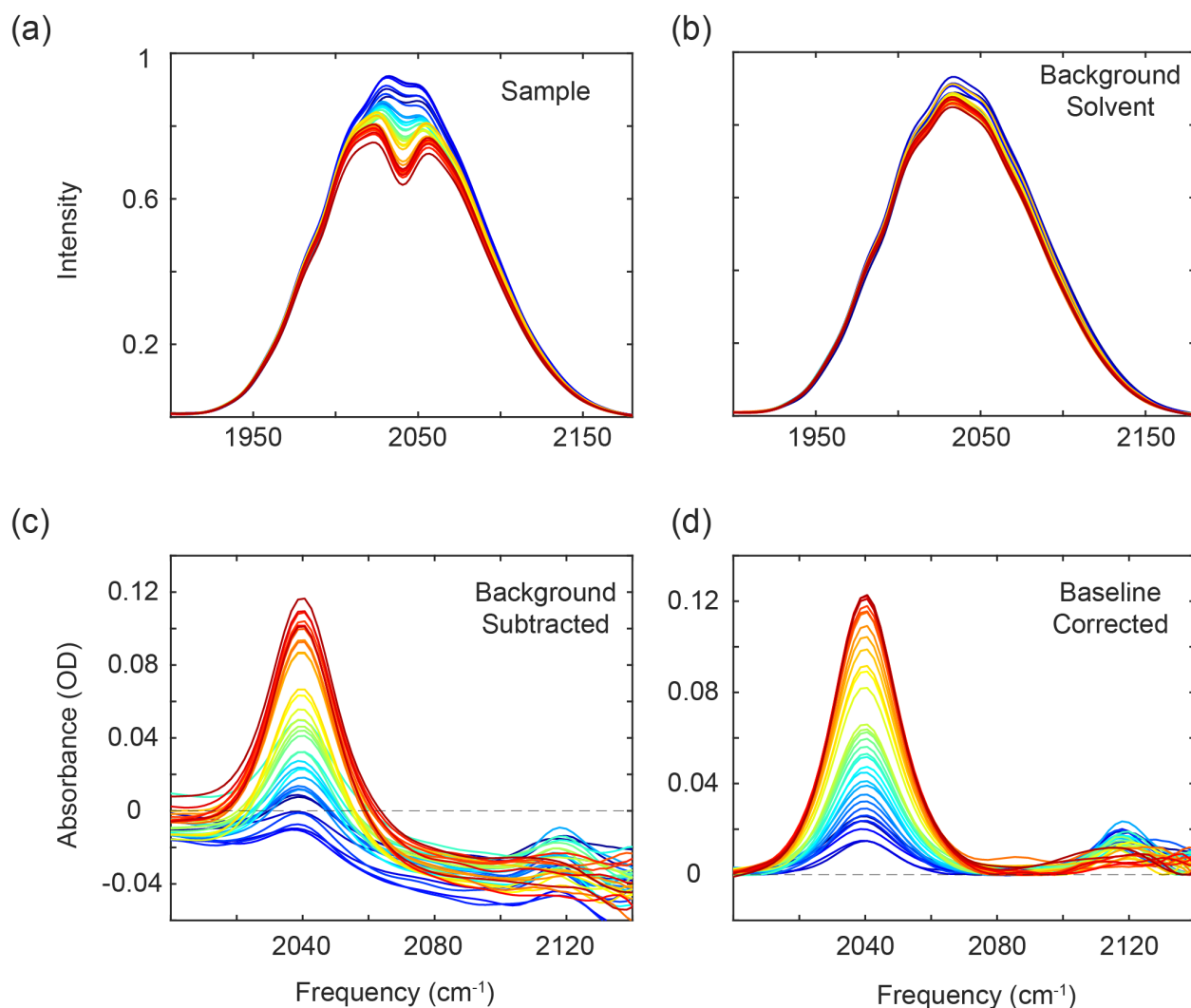


Figure 6.8: Potassium ferricyanide reduction kinetics probed with laser-based IR spectroscopy employing a 3-turn mixer. (a) IR intensities following the mixing of 0.1 M ascorbic acid with 25 mM ferricyanide within a 0.5 M potassium phosphate buffer at pH 8.5. The color transition from blue (50  $\mu$ s) to red (4 ms) on the colormap corresponds to early to late time points. The IR source, centered at 2038  $\text{cm}^{-1}$ , with FWHM of 150  $\text{cm}^{-1}$ , facilitates simultaneous probing of both ferricyanide at 2115  $\text{cm}^{-1}$  and the ferrocyanide mode at 2037  $\text{cm}^{-1}$ . (b) IR intensities of the solvent (0.5 M buffer) collected at the corresponding sample measurement points. (c) Linear IR absorption spectra from direct difference of the sample and solvent intensities. The growth of the ferrocyanide mode is evident, while the decay of the ferricyanide exhibits relatively more noise in comparison. (d) IR absorption spectra post baseline correction using a discrete wavelet method.

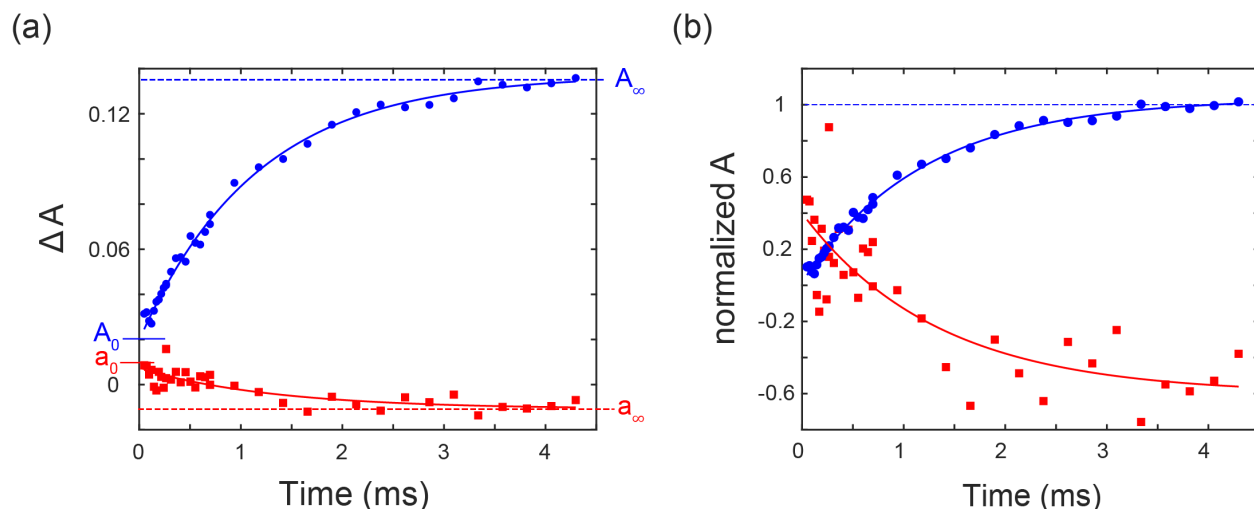


Figure 6.9: Fitting and normalization schemes. (a) Time dependent peak absorbance for ferri-cyanide mode (red squares) and ferrocyanide (blue circles), fitted with exponential functions to extract the baselines ( $A_\infty$ ,  $a_\infty$ ) and time zero absorbance values ( $A_0$ ,  $a_0$ ). (b) Application of normalization procedures using baseline and initial values, following the methodologies outlined in equations 6.21 and 6.20, along with corresponding fitting outcomes. The fitting performance for ferricyanide is somewhat compromised due to the presence of measurement noise.

In Figure 6.10 (a) the time-dependent normalized absorbance for the ferrocyanide mode is illustrated for pH values of 12.3, 11.7, and 8.5. The relaxation time obtained from the fit is 325  $\mu\text{s}$  at pH 12.3 representing the most rapid measured kinetics using an IR micromixer within our current knowledge. There is potential to explore kinetics in the 200-250  $\mu\text{s}$  range through measurements at elevated flow rates. For instance, employing a flow rate of 0.4 mL/min yields an impressive time resolution of 40  $\mu\text{s}$ . With a laser beam spot of 12.5  $\mu\text{m}$  FWHM, measurements can be obtained at a distance of 25  $\mu\text{m}$ , corresponding to a time delay of 20  $\mu\text{s}$ .

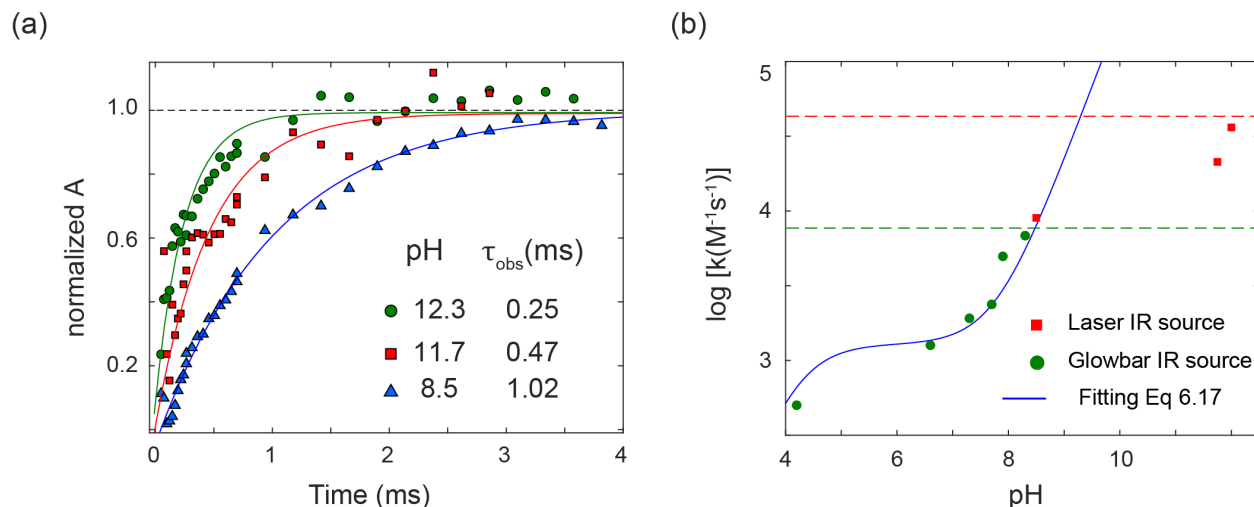


Figure 6.10: (a) Normalized time-dependent peak absorbance for ferrocyanide vibrations for pH 8.5, 11.7 and 12.3, accompanied by fitted exponential curves. The fitting and normalization methodologies are detailed in section 6.4.1. (b) pH-dependent rate constants measured experimentally using both glowbar source (green circles) and laser (red square), juxtaposed with the kinetic model derived from Equation 6.17. The dashed lines represent the limit on the fastest rate constants measurable with each method.

Figure 6.10 (b) illustrates the plot of pH dependent rate constant as determined from both methods. While we initially postulated that the divergence between the experimental data and theoretical model for pH values exceeding 9 could be attributed to the instrument's limited time resolution imposed by the broad IR light from the glowbar source, it appears that the issue is more complex. Surprisingly, even when utilizing the laser-based source with its superior resolution, this deviation persists. This observation demands a comprehensive investigation to unravel the various aspects pertaining to the model reaction and the intricacies of our instrument.

### 6.5.3 Reaction mechanism at high pH

We initiate this investigation by considering the possibility that the mechanism governing the reduction reaction under higher pH conditions differs from the previously proposed assumptions outlined in 6.2.1. This hypothesis arises due to the observation that the collected



data aligns more closely with a bi-exponential model rather than a single exponential one. In a bi-exponential fit, each exponential function signifies a distinct rate constant and amplitude. When combined, these functions offer a more precise depiction of the intricate kinetics that cannot be adequately captured by a single exponential model.

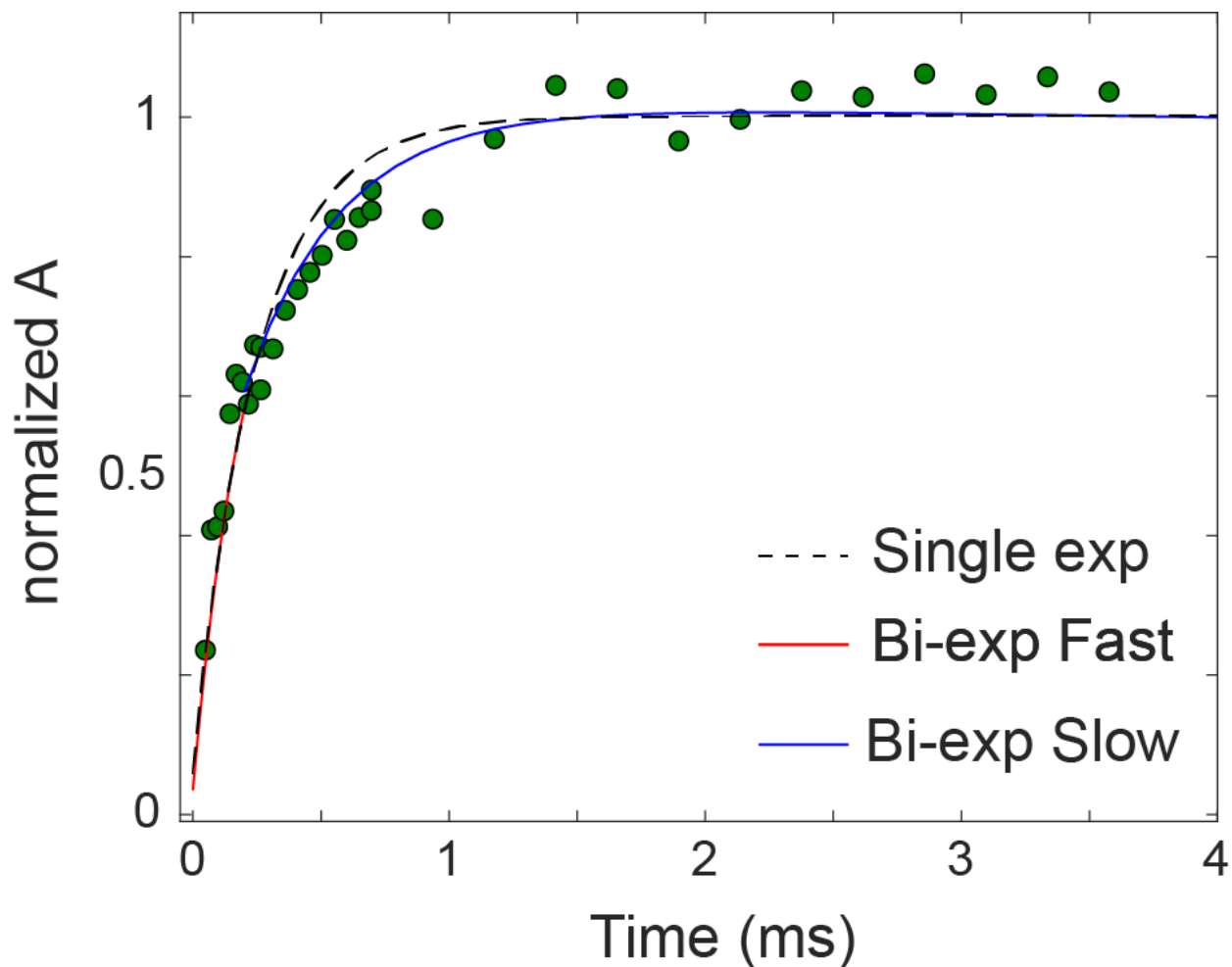
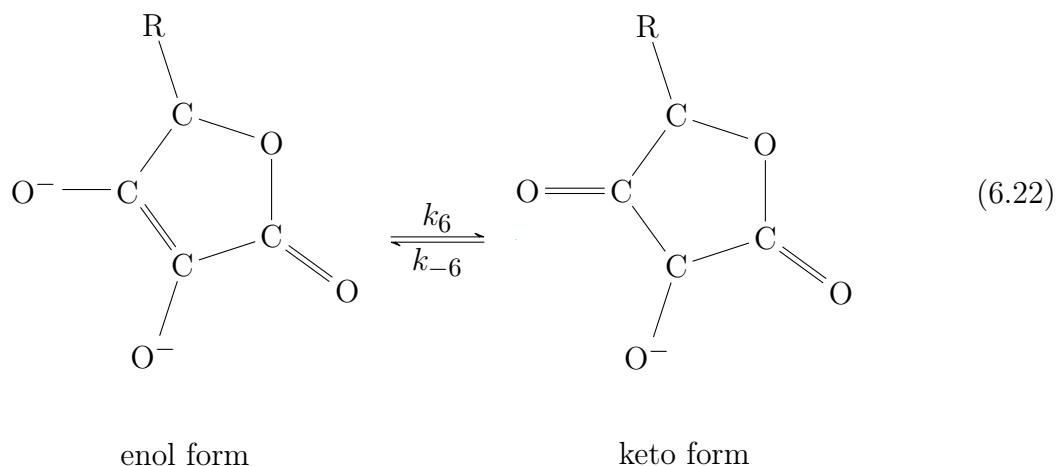


Figure 6.11: Normalized time-dependent peak absorbance for ferrocyanide vibrations for pH 12.3 fitted to a fast (red) and slow (blue) bi-exponential curves. The goodness of the fit is better compared to the single exponential.

For the data collected at pH 12.3, we present an illustration of a both bi-exponential and mono-exponential fits in Figure 6.11. Initially, during the very early stages, the reduction reaction appears to proceed with a rapid time constant, eventually transitioning to a slower time constant. This pattern therefore is better represented by bi-exponential fit compared

to single exponential. This observation holds particular chemical interest and may suggest a complex reaction scheme. However, before we delve into this hypothesis, it's crucial to acknowledge some imperfections in our instrumentation. It's highly likely that the trend observed is a result of insufficient mixing during the initial stages of the measurement. It's possible that the mixer achieved a better degree of mixing at some distance from the end of the mixer, causing the kinetic traces up to that point to appear faster. To confirm this, one approach would be to conduct the experiment at higher flow rates, where we anticipate improved mixing efficiency. We can then compare the kinetic data to determine if this pattern still persists.

On the other hand, it is also possible that the reaction at high pH is indeed complex, leading to this bi-exponential pattern. For instance, if the active reactant species is being depleted from the main reduction reaction due to a side reaction, this could result in such behavior. Ascorbic acid mainly exists in the deprotonated state as ascorbate di-anion ( $A^{2-}$ ) at high pH. The ascorbate di-anion can exist in either an enol or tautomerize to a keto-form as follows:



The enol form is considered as an active species that reduces the ferrocyanide, while the keto form does not participate in the reduction mechanism. The enol-keto equilibrium can, therefore, significantly influence the overall reaction rate. Additionally, previous studies

have documented ferricyanide's exceptional oxidative potency in alkaline media as an efficient electron-abstracting reagent [148]. This suggests the need for a different mechanistic scheme for the reduction reaction at high pH. To propose a new mechanism, we require extensive kinetic data, which is currently lacking.

## 6.6 Discussion and Outlook

We have demonstrated the utility of an IR-compatible rapid mixer for resolving reaction kinetics occurring in hundreds of microseconds to tens of milliseconds, using a model reduction reaction of ferricyanide by ascorbic acid. This serves as a promising proof-of-concept for future studies on rapid reaction kinetics. As we plan to implement these methodologies in the investigation of complex biological systems such as DNA hybridization and protein folding, several pitfalls must be carefully considered.

We observed deviation in the peak absorption values for the initial two measurement points when fitting the data collected with the inchworm mixer to exponential curves (refer to Figure 6.5). These deviations occurred at time points corresponding to 200  $\mu\text{s}$  and 400  $\mu\text{s}$  and are situated within 1 mm from the mixer's exit. What's particularly intriguing is that this observation is consistent across all pH data sets, indicating a potential overestimation of the peak absorption value. As a result, further investigation is warranted to gain a deeper understanding of this recurring trend. Several factors could contribute to this observation. The most probable hypothesis is that it results from inadequate mixing during the initial stages of the measurement.

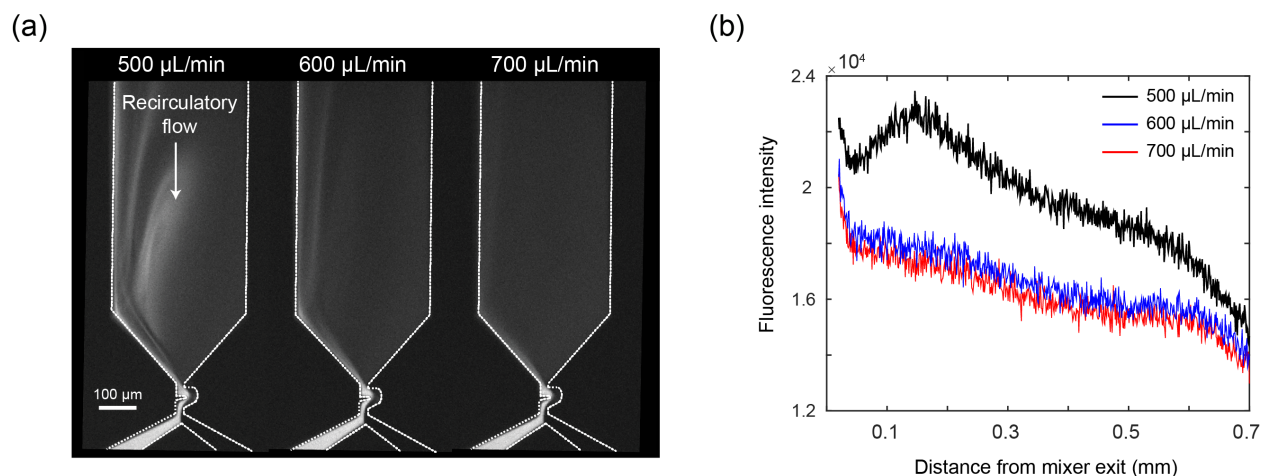


Figure 6.12: (a) Fluorescence images capturing the observation channel after the quenching reaction of 1  $\mu\text{m}$  fluorescein by 0.5M potassium iodide within an inchworm mixer. (b) A fluorescence intensity plot as a function of distance from the mixer exit, recorded at three distinct flow rates. The gradual incline is a result of non-uniform excitation caused by a halogen lamp. The data indicates that, at a flow rate of 500  $\mu\text{L}/\text{min}$ , a minimum distance of 0.7 mm from the mixer's exit is required for complete quenching.

During the mixing process, the reactant solutions undergo a series of stirring events in the turns of the mixer that maximizes diffusion to ultimately mix the solutions. There are interesting and unpredictable flow patterns in the observation channel during the process. To obtain reliable and meaningful data, it is crucial to identify the point in time when the reactant mixture reaches a state of homogeneity. In our experiments utilizing the inchworm mixer, the results derived from fluorescence quenching involving fluorescein and potassium iodide suggest a predominantly homogeneous mixture at a flow rate of 700  $\mu\text{L}/\text{min}$ , as depicted in Figure 6.12 (a). It is worth noting, however, that even at this flow rate, there remains a slender stream measuring a few microns in width on the left side of the mixer that appears to be inadequately mixed.

For our infrared (IR) measurements, we consistently used inchworm-style mixers at a flow rate of 700  $\mu\text{L}/\text{min}$ . Since these mixers are single-use, there are inherent variations in their performance from one experiment to another. Given that each mixer cannot be individually characterized for extent of mixing using fluorescence quenching and used simultaneously for

IR measurements, any deviations in the flow pattern due to incomplete mixing can lead to anomalies in the data. For instance, if a recirculatory flow pattern, as observed in the case of  $500 \mu\text{L}/\text{min}$  (Figure 6.12 a), occurs, then the initial few measurements can be confounded by insufficient mixing. In such scenarios, it appears that the reactant mixture within the inchworm mixer eventually achieves homogeneity after the first two measurement points.

Another important consideration is the potential impact of the instrumentation on the measured kinetics. In relaxation techniques, such as temperature jump spectroscopy, the observed time-dependent behavior (O) is often modeled as the convolution between the true system response (S) and the instrument response function (IRF) [149]. In such instances, the IRF is typically determined by the solvent's temperature profile, which can usually be fitted to a stretched exponential function. However, when dealing with a rapid mixer, determining the instrument response function becomes a challenging task due to the intricacies involved in mixing and fluid dynamics. Despite the universal nature of mixing processes, it is noteworthy that the field of mixing does not enjoy the same level of scientific rigor, as emphasized by J. Ottino in 1989 [150], which makes a comprehensive analysis challenging.

In conclusion, we have demonstrated the utility of an IR-compatible rapid mixer for studying reaction kinetics, specifically focusing on the reduction reaction of ferricyanide by ascorbic acid. Our proof-of-concept micro mixer holds great potential for further development in studying complex biological systems, such as DNA hybridization and protein folding. With advancements in microfluidic technologies, spectral analysis, and data processing, we envision deeper insights into the dynamics of rapid chemical and biological reactions. This platform opens new possibilities for understanding and manipulating complex molecular processes and may impact fields such as drug discovery, catalysis, and biomolecular engineering.

## 6.7 Appendix

### 6.7.1 *Sample preparation*

Potassium ferricyanide  $K_3[Fe(CN)_6]$ , ferrocyanide  $K_4[Fe(CN)_6]$ , L-ascorbic acid, anhydrous potassium phosphate monobasic, dibasic, and tribasic salts were purchased from Fisher Scientific and used as received. Both ascorbic acid and potassium ferricyanide were prepared in the buffer solution on the day of the experiment to avoid unwanted reactions with oxygen and moisture in the atmosphere. The pH of each reagent and final mixture were measured using a standard glass electrode pH meter.

## REFERENCES

- [1] Nuclear Power. Laminar and turbulent flow, n.d. Accessed: November 1, 2023.
- [2] Ying Li, Chao Liu, Xiaojun Feng, Youzhi Xu, and Bi-Feng Liu. Ultrafast microfluidic mixer for tracking the early folding kinetics of human telomere g-quadruplex. *Analytical Chemistry*, 86(9):4333–4339, 2014.
- [3] Ying Li, Dalu Zhang, Xiaojun Feng, Youzhi Xu, and Bi-Feng Liu. A microsecond microfluidic mixer for characterizing fast biochemical reactions. *Talanta*, 88:175–180, 2012.
- [4] A. D. Stroock, S. K. Dertinger, A. Ajdari, I. Mezic, H. A. Stone, and G. M. Whitesides. Chaotic mixer for microchannels. *Science*, 295(5555):647–51, 2002.
- [5] Steffen Diez. The next generation of maskless lithography. In *Emerging Digital Micromirror Device Based Systems and Applications VIII*, volume 9761, page 976102. SPIE.
- [6] Catharina Goedecke. Physical chemistry pioneer: Svante arrhenius (1859–1927).
- [7] James K Laylin. *Nobel laureates in chemistry, 1901-1992*. Chemical Heritage Foundation, 1993.
- [8] Ernest Rutherford and Frederick Soddy. Lx. radioactive change. *The London, Edinburgh, and Dublin Philosophical Magazine and Journal of Science*, 5(29):576–591, 1903.
- [9] Josh Van Houten. A century of chemical dynamics traced through the nobel prizes. 1956: Hinshelwood and semenov. *Journal of chemical education*, 79(4):414, 2002.
- [10] Carlos R Baiz, Bartosz Błasiak, Jens Bredenbeck, Minhaeng Cho, Jun-Ho Choi, Steven A Corcelli, Arend G Dijkstra, Chi-Jui Feng, Sean Garrett-Roe, and Nien-Hui Ge. Vibrational spectroscopic map, vibrational spectroscopy, and intermolecular interaction. *Chemical reviews*, 120(15):7152–7218, 2020.
- [11] Marie Louise Groot and Rienk Van Grondelle. *Femtosecond time-resolved infrared spectroscopy*, pages 191–200. Springer, 2008.
- [12] O. G. Berg and P. H. von Hippel. Diffusion-controlled macromolecular interactions. *Annu Rev Biophys Biophys Chem*, 14:131–60, 1985.
- [13] DAVID Shoup, GIOVANNI Lipari, and ATrILA SzABO. Diffusion-controlled bimolecular reaction rates. the effect of rotational diffusion and orientation constraints. *Biophysical Journal*, 36(3):697–714, 1981.
- [14] A JohnáElliot. Estimation of rate constants for near-diffusion-controlled reactions in water at high temperatures. *Journal of the Chemical Society, Faraday Transactions*, 86(9):1539–1547, 1990.

- [15] Gerald Wilemski and Marshall Fixman. General theory of diffusion-controlled reactions. *The Journal of chemical physics*, 58(9):4009–4019, 1973.
- [16] Alastair M North. Diffusion-controlled reactions. *Quarterly Reviews, Chemical Society*, 20(3):421–440, 1966.
- [17] Peter Regenfuss, Robert M Clegg, Mack J Fulwyler, Francisco J Barrantes, and Thomas M Jovin. Mixing liquids in microseconds. *Review of Scientific Instruments*, 56(2):283–290, 1985.
- [18] Robert L Berger, Bohdan Balko, and Howard F Chapman. High resolution mixer for the study of the kinetics of rapid reactions in solution. *Review of Scientific Instruments*, 39(4):493–498, 1968.
- [19] Osman Bilsel, Can Kayatekin, Louise A Wallace, and C Robert Matthews. A microchannel solution mixer for studying microsecond protein folding reactions. *Review of scientific instruments*, 76(1):014302, 2005.
- [20] Hamilton Hartridge and Francis John Worsley Roughton. A method of measuring the velocity of very rapid chemical reactions. *Proceedings of the Royal Society of London. Series A, Containing Papers of a Mathematical and Physical Character*, 104(726):376–394, 1923.
- [21] Francis John Worsley Roughton and GA Millikan. Photoelectric methods of measuring the velocity of rapid reactions i-general principles and controls. *Proceedings of the Royal Society of London. Series A-Mathematical and Physical Sciences*, 155(885):258–269, 1936.
- [22] Britton Chance. The accelerated flow method for rapid reactions. *Journal of the Franklin Institute*, 229(6):737–766, 1940.
- [23] Britton Chance, Quentin H Gibson, Rudolf H Eisenhardt, and K Karl Lonberg-Holm. Rapid mixing and sampling techniques. *Science*, 146(3652):1697–1699, 1964.
- [24] H Gutfreund. [7] rapid mixing: Continuous flow. *Methods in enzymology*, 16:229–249, 1969.
- [25] Britton Chance. Intracellular reaction kinetics. *Discussions of the Faraday Society*, 20:205–216, 1955.
- [26] Britton Chance. Rapid and sensitive spectrophotometry. i. the accelerated and stopped-flow methods for the measurement of the reaction kinetics and spectra of unstable compounds in the visible region of the spectrum. *Review of Scientific Instruments*, 22(8):619–627, 1951.
- [27] Peter S. Kim and Robert L. Baldwin. Specific intermediates in the folding reactions of small proteins and the mechanism of protein folding. *Annual Review of Biochemistry*, 51(1):459–489, 1982.



- [28] C. R. Matthews. Pathways of protein folding. *Annu Rev Biochem*, 62:653–83, 1993.
- [29] Bing-Feng Shi, Yang-Hui Zhang, Jonathan K. Lam, Dong-Hui Wang, and Jin-Quan Yu. Pd(ii)-catalyzed enantioselective ch olefination of diphenylacetic acids. *Journal of the American Chemical Society*, 132(2):460–461, 2010.
- [30] Heinrich Roder, Kosuke Maki, Hong Cheng, and M. C. Ramachandra Shastri. Rapid mixing methods for exploring the kinetics of protein folding. *Methods (San Diego, Calif.)*, 34(1):15–27, 2004.
- [31] David B. Green, James Lane, and Richard M. Wing. A standard session stopped-flow nmr tube. *Applied Spectroscopy*, 41(5):847–851, 1987.
- [32] J Luchins and S Beychok. Far-ultraviolet stopped-flow circular dichroism. *Science*, 199(4327):425–426, 1978.
- [33] Munehito Arai and Kunihiro Kuwajima. Rapid formation of a molten globule intermediate in refolding of -lactalbumin. *Folding and Design*, 1(4):275–287, 1996.
- [34] Simon J. George, Gillian A. Ashby, Christopher W. Wharton, and Roger N. F. Thorneley. Time-resolved binding of carbon monoxide to nitrogenase monitored by stopped-flow infrared spectroscopy. *Journal of the American Chemical Society*, 119(27):6450–6451, 1997.
- [35] Simon J. George, Sergei Kurkin, Roger N. F. Thorneley, and Simon P. J. Albracht. Reactions of h<sub>2</sub>, co, and o<sub>2</sub> with active [nife]-hydrogenase from allochromatium vinosum. a stopped-flow infrared study. *Biochemistry*, 43(21):6808–6819, 2004.
- [36] John S. Olson. [38] *Stopped-flow, rapid mixing measurements of ligand binding to hemoglobin and red cells*, volume 76, pages 631–651. Academic Press, 1981.
- [37] Boping Liu, Hitoshi Matsuoka, and Minoru Terano. Stopped-flow techniques in ziegler catalysis. *Macromolecular Rapid Communications*, 22(1):1–24, 2001.
- [38] Elizabeth G Kelley, Michael HL Nguyen, Drew Marquardt, Brian B Maranville, and Ryan P Murphy. Measuring the time-evolution of nanoscale materials with stopped-flow and small-angle neutron scattering. *JoVE (Journal of Visualized Experiments)*, (174):e62873, 2021.
- [39] Heinz Fabian and Dieter Naumann. Methods to study protein folding by stopped-flow ft-ir. *Methods*, 34(1):28–40, 2004.
- [40] Simon J George, Sergei Kurkin, Roger NF Thorneley, and Simon PJ Albracht. Reactions of h<sub>2</sub>, co, and o<sub>2</sub> with active [nife]-hydrogenase from allochromatium vinosum. a stopped-flow infrared study. *Biochemistry*, 43(21):6808–6819, 2004.

- [41] Peter Hinsmann, Johannes Frank, Peter Svasek, Michael Harasek, and Bernhard Lendl. Design, simulation and application of a new micromixing device for time resolved infrared spectroscopy of chemical reactions in solution. *Lab on a Chip*, 1(1):16–21, 2001.
- [42] Bengt Nölting. *Protein folding kinetics: biophysical methods*. Springer Science Business Media, 2005.
- [43] Brian C Dunn and Edward M Eyring. Stopped-flow rapid-scan fourier transform infrared spectroscopy. *Applied spectroscopy*, 53(3):292–296, 1999.
- [44] Nicolas H Pinkowski, Pujan Biswas, Jiankun Shao, Christopher L Strand, and Ronald K Hanson. Thermometry and speciation for high-temperature and-pressure methane pyrolysis using shock tubes and dual-comb spectroscopy. *Measurement Science and Technology*, 32(12):125502, 2021.
- [45] Raphael Horvath, Edward J King, Florian Eigenmann, Markus Mangold, and Andreas Hugi. Development of fast frequency comb mid-infrared spectroscopy for stopped flow applications. In *Applied Industrial Optics: Spectroscopy, Imaging and Metrology*, page F1A. 3. Optica Publishing Group.
- [46] Robin Rammelsberg, Sophie Boulas, Harald Chorongiewski, and Klaus Gerwert. Setup for time-resolved step-scan ftir spectroscopy of noncyclic reactions. *Vibrational Spectroscopy*, 19(1):143–149, 1999.
- [47] George M Whitesides. The origins and the future of microfluidics. *nature*, 442(7101):368–373, 2006.
- [48] Younan Xia and George M Whitesides. Soft lithography. *Annual review of materials science*, 28(1):153–184, 1998.
- [49] Mu Chiao. A microfabricated pdms microbial fuel cell. *Journal of Microelectromechanical systems*, 17(6):1329–1341, 2008.
- [50] Holger Becker and Claudia Gärtner. Polymer microfabrication methods for microfluidic analytical applications. *ELECTROPHORESIS: An International Journal*, 21(1):12–26, 2000.
- [51] Gwo-Bin Lee, Shu-Hui Chen, Guan-Ruey Huang, Wang-Chou Sung, and Yen-Heng Lin. Microfabricated plastic chips by hot embossing methods and their applications for dna separation and detection. *Sensors and Actuators B: Chemical*, 75(1-2):142–148, 2001.
- [52] Shantanu Bhattacharya, Arindom Datta, Jordan M Berg, and Shubhra Gangopadhyay. Studies on surface wettability of poly (dimethyl) siloxane (pdms) and glass under oxygen-plasma treatment and correlation with bond strength. *Journal of microelectromechanical systems*, 14(3):590–597, 2005.

- [53] Mark A Eddings, Michael A Johnson, and Bruce K Gale. Determining the optimal pdms–pdms bonding technique for microfluidic devices. *Journal of Micromechanics and Microengineering*, 18(6):067001, 2008.
- [54] Alexandra Borók, Kristóf Laboda, and Attila Bonyár. Pdms bonding technologies for microfluidic applications: A review. *Biosensors*, 11(8):292, 2021.
- [55] Cyrus Weijie Beh, Weizhuang Zhou, and Tza-Huei Wang. Pdms–glass bonding using grafted polymeric adhesive—alternative process flow for compatibility with patterned biological molecules. *Lab on a Chip*, 12(20):4120–4127, 2012.
- [56] Gwo-Bin Lee, Chih-Chang Chang, Sung-Bin Huang, and Ruey-Jen Yang. The hydrodynamic focusing effect inside rectangular microchannels. *Journal of Micromechanics and Microengineering*, 16(5):1024, 2006.
- [57] James B Knight, Ashvin Vishwanath, James P Brody, and Robert H Austin. Hydrodynamic focusing on a silicon chip: mixing nanoliters in microseconds. *Physical review letters*, 80(17):3863, 1998.
- [58] Olgica B Bakajin, James P Brody, Jeff Chou, Shirley S Chan, Thomas AJ Duke, James Knight, Lydia L Sohn, Ashvin Vishwanath, Robert H Austin, and EC Cox. Polymer dynamics and fluid flow in microfabricated devices. In *Micro-and Nanofabricated Structures and Devices for Biomedical Environmental Applications*, volume 3258, pages 100–113. SPIE.
- [59] Philipp Schulze, Martin Ludwig, Frank Kohler, and Detlev Belder. Deep uv laser-induced fluorescence detection of unlabeled drugs and proteins in microchip electrophoresis. *Analytical chemistry*, 77(5):1325–1329, 2005.
- [60] 2006.
- [61] Hye Yoon Park, Xiangyun Qiu, Elizabeth Rhoades, Jonas Korlach, Lisa W Kwok, Warren R Zipfel, Watt W Webb, and Lois Pollack. Achieving uniform mixing in a microfluidic device: hydrodynamic focusing prior to mixing. *Analytical chemistry*, 78(13):4465–4473, 2006.
- [62] David E Hertzog, Benjamin Ivorra, Bijan Mohammadi, Olgica Bakajin, and Juan G Santiago. Optimization of a microfluidic mixer for studying protein folding kinetics. *Analytical chemistry*, 78(13):4299–4306, 2006.
- [63] Petra S. Dittrich and Andreas Manz. Single-molecule fluorescence detection in microfluidic channels—the holy grail in tas? *Analytical and Bioanalytical Chemistry*, 382(8):1771–1782, 2005.
- [64] WE Moerner and David P Fromm. Methods of single-molecule fluorescence spectroscopy and microscopy. *Review of Scientific instruments*, 74(8):3597–3619, 2003.

- [65] Shimon Weiss. Measuring conformational dynamics of biomolecules by single molecule fluorescence spectroscopy. *Nature structural biology*, 7(9):724–729, 2000.
- [66] Smitha S Varghese, Yonggang Zhu, Timothy J Davis, and Stephen C Trowell. Fret for lab-on-a-chip devices—current trends and future prospects. *Lab on a Chip*, 10(11):1355–1364, 2010.
- [67] Rahul Roy, Sungchul Hohng, and Taekjip Ha. A practical guide to single-molecule fret. *Nature methods*, 5(6):507–516, 2008.
- [68] Elizabeth A Jares-Erijman and Thomas M Jovin. Fret imaging. *Nature biotechnology*, 21(11):1387–1395, 2003.
- [69] Linliang Yin, Wei Wang, Shaopeng Wang, Fenni Zhang, Shengtao Zhang, and Nongjian Tao. How does fluorescent labeling affect the binding kinetics of proteins with intact cells? *Biosensors and Bioelectronics*, 66:412–416, 2015.
- [70] Bekir Salih and Renato Zenobi. Maldi mass spectrometry of dye peptide and dye protein complexes. *Analytical chemistry*, 70(8):1536–1543, 1998.
- [71] Jay R Unruh, Giridharan Gokulrangan, GH Lushington, Carey K Johnson, and George S Wilson. Orientational dynamics and dye-dna interactions in a dye-labeled dna aptamer. *Biophysical journal*, 88(5):3455–3465, 2005.
- [72] Lee Whitmore and Bonnie A Wallace. Protein secondary structure analyses from circular dichroism spectroscopy: methods and reference databases. *Biopolymers: Original Research on Biomolecules*, 89(5):392–400, 2008.
- [73] Alexey S Ladokhin, Mónica Fernández-Vidal, and Stephen H White. Cd spectroscopy of peptides and proteins bound to large unilamellar vesicles. *The Journal of membrane biology*, 236:247–253, 2010.
- [74] Shuji Akiyama, Satoshi Takahashi, Koichiro Ishimori, and Isao Morishima. Stepwise formation of  $\alpha$ -helices during cytochrome c folding. *Nature structural biology*, 7(6):514–520, 2000.
- [75] Drew P Kise, Michael J Reddish, and R Brian Dyer. Sandwich-format 3d printed microfluidic mixers: A flexible platform for multi-probe analysis. *Journal of Micromechanics and Microengineering*, 25(12):124002, 2015.
- [76] Drew P. Kise, Donny Magana, Michael J. Reddish, and R. Brian Dyer. Submillisecond mixing in a continuous-flow, microfluidic mixer utilizing mid-infrared hyperspectral imaging detection. *Lab on a chip*, 14(3):584–591, 2014.
- [77] T. Pan, R. T. Kelly, M. C. Asplund, and A. T. Woolley. Fabrication of calcium fluoride capillary electrophoresis microdevices for on-chip infrared detection. *J Chromatogr A*, 1027(1-2):231–5, 2004.

- [78] Brynson Lehmkuhl, Scott D. Noblitt, Amber T. Krummel, and Charles S. Henry. Fabrication of ir-transparent microfluidic devices by anisotropic etching of channels in caf2. *Lab on a Chip*, 15(22):4364–4368, 2015.
- [79] Tamara M Floyd, Martin A Schmidt, and Klavs F Jensen. Silicon micromixers with infrared detection for studies of liquid-phase reactions. *Industrial engineering chemistry research*, 44(8):2351–2358, 2005.
- [80] Peter Hinsmann, Johannes Frank, Peter Svasek, Michael Harasek, and Bernhard Lendl. Design, simulation and application of a new micromixing device for time resolved infrared spectroscopy of chemical reactions in solution. *Lab on a Chip*, 1(1):16–21, 2001.
- [81] Peter Svasek, Edda Svasek, Bernhard Lendl, and Michel Vellekoop. Fabrication of miniaturized fluidic devices using su-8 based lithography and low temperature wafer bonding. *Sensors and Actuators A: Physical*, 115(2-3):591–599, 2004.
- [82] Peter Hinsmann, Michael Haberkorn, Johannes Frank, Peter Svasek, Michael Harasek, and Bernhard Lendl. Time-resolved ft-ir spectroscopy of chemical reactions in solution by fast diffusion-based mixing in a micromachined flow cell. *Applied Spectroscopy*, 55(3):241–251, 2001.
- [83] Nina Kaun, Stephan Kulka, Johannes Frank, Ulrich Schade, Michiel J Vellekoop, Michael Harasek, and Bernhard Lendl. Towards biochemical reaction monitoring using ft-ir synchrotron radiation. *Analyst*, 131(4):489–494, 2006.
- [84] Stephan Kulka, Nina Kaun, Josefa R Baena, Johannes Frank, Peter Svasek, David Moss, Michael J Vellekoop, and Bernhard Lendl. Mid-ir synchrotron radiation for molecular specific detection in microchip-based analysis systems. *Analytical and bio-analytical chemistry*, 378(7):1735–1740, 2004.
- [85] Nina Kaun, Michael J Vellekoop, and Bernhard Lendl. Time-resolved fourier transform infrared spectroscopy of chemical reactions in solution using a focal plane array detector. *Applied spectroscopy*, 60(11):1273–1278, 2006.
- [86] Wolfgang Buchegger, Christoph Wagner, Bernhard Lendl, Martin Kraft, and Michael J Vellekoop. A highly uniform lamination micromixer with wedge shaped inlet channels for time resolved infrared spectroscopy. *Microfluidics and Nanofluidics*, 10(4):889–897, 2011.
- [87] Wolfgang Buchegger, Christoph Wagner, Peter Svasek, Bernhard Lendl, Martin Kraft, and Michael J Vellekoop. Fabrication and characterization of a vertical lamination micromixer for mid-ir spectroscopy. *Sensors and Actuators B: Chemical*, 159(1):336–341, 2011.
- [88] Simon G Kaplan, Leonard M Hanssen, and RU Datla. Testing the radiometric accuracy of fourier transform infrared transmittance measurements. *Applied Optics*, 36(34):8896–8908, 1997.

- [89] Yunkun Jiang, Ottavia Jedrkiewicz, Stefano Minardi, Paolo DiTrapani, Alexis Mosset, Eric Lantz, and Fabrice Devaux. Retrieval of spatial shot-noise in the full dynamic range of calibrated ccd cameras. *The European Physical Journal D-Atomic, Molecular, Optical and Plasma Physics*, 22:521–526, 2003.
- [90] M. V. Barich and A. T. Krummel. Polymeric infrared compatible microfluidic devices for spectrochemical analysis. *Anal Chem*, 85(21):10000–3, 2013.
- [91] M. Srisa-Art, S. D. Noblitt, A. T. Krummel, and C. S. Henry. Ir-compatible pdms microfluidic devices for monitoring of enzyme kinetics. *Anal Chim Acta*, 1021:95–102, 2018.
- [92] Monpichar Srisa-Art, Scott D Noblitt, Amber T Krummel, and Charles S Henry. Ir-compatible pdms microfluidic devices for monitoring of enzyme kinetics. *Analytica Chimica Acta*, 1021:95–102, 2018.
- [93] Hyukjin Jang, Ashtamurthy S. Pawate, Rohit Bhargava, and Paul J. A. Kenis. Polymeric microfluidic continuous flow mixer combined with hyperspectral ft-ir imaging for studying rapid biomolecular events. *Lab on a Chip*, 19(15):2598–2609, 2019.
- [94] Adeline Perro, Gwenaelle Lebourdon, Sarah Henry, Sophie Lecomte, Laurent Servant, and Samuel Marre. Combining microfluidics and ft-ir spectroscopy: towards spatially resolved information on chemical processes. *Reaction Chemistry Engineering*, 1(6):577–594, 2016.
- [95] Monpichar Srisa-Art and Yuji Furutani. Simple and rapid fabrication of pdms microfluidic devices compatible with ftir microspectroscopy. *Bulletin of the Chemical Society of Japan*, 89(2):195–202, 2016.
- [96] Sergei G Kazarian and KL Andrew Chan. Atr-ftir spectroscopic imaging: recent advances and applications to biological systems. *Analyst*, 138(7):1940–1951, 2013.
- [97] KL Andrew Chan, Shelly Gulati, Joshua B Edel, Andrew J de Mello, and Sergei G Kazarian. Chemical imaging of microfluidic flows using atr-ftir spectroscopy. *Lab on a Chip*, 9(20):2909–2913, 2009.
- [98] Etienne Guyon, Jean Pierre Hulin, Luc Petit, and Catalin D Mitescu. *Physical hydrodynamics*. Oxford university press, 2015.
- [99] Brian J Kirby. *Micro-and nanoscale fluid mechanics: transport in microfluidic devices*. Cambridge university press, 2010.
- [100] Suman Chakraborty. *Microfluidics and microfabrication*. 2010.
- [101] Todd M. Squires and Stephen R. Quake. Microfluidics: Fluid physics at the nanoliter scale. *Reviews of Modern Physics*, 77(3):977–1026, 2005.

- [102] Howard A Stone. Introduction to fluid dynamics for microfluidic flows. *CMOS biotechnology*, pages 5–30, 2007.
- [103] Christopher M Dobson. Protein folding and misfolding. *Nature*, 426(6968):884–890, 2003.
- [104] Ken A Dill, S Banu Ozkan, M Scott Shell, and Thomas R Weikl. The protein folding problem. *Annu. Rev. Biophys.*, 37:289–316, 2008.
- [105] Ken A Dill and Justin L MacCallum. The protein-folding problem, 50 years on. *science*, 338(6110):1042–1046, 2012.
- [106] V. Mengeaud, J. Jossierand, and H. H. Girault. Mixing processes in a zigzag microchannel: finite element simulations and optical study. *Anal Chem*, 74(16):4279–86, 2002.
- [107] Arshad Afzal and Kwang-Yong Kim. Passive split and recombination micromixer with convergent–divergent walls. *Chemical Engineering Journal*, 203:182–192, 2012.
- [108] Volker Hessel, Holger Löwe, and Friedhelm Schönfeld. Micromixers—a review on passive and active mixing principles. *Chemical Engineering Science*, 60(8-9):2479–2501, 2005.
- [109] Wolfgang Buchegger, Christoph Wagner, Bernhard Lendl, Martin Kraft, and Michael J Vellekoop. A highly uniform lamination micromixer with wedge shaped inlet channels for time resolved infrared spectroscopy. *Microfluidics and Nanofluidics*, 10(4):889–897, 2011.
- [110] Seck Hoe Wong, Patrick Bryant, Michael Ward, and Christopher Wharton. Investigation of mixing in a cross-shaped micromixer with static mixing elements for reaction kinetics studies. *Sensors and Actuators B: Chemical*, 95(1-3):414–424, 2003.
- [111] 2004.
- [112] Di Jiang, Chen Ni, Wenlai Tang, Di Huang, and Nan Xiang. Inertial microfluidics in contraction–expansion microchannels: A review. *Biomicrofluidics*, 15(4), 2021.
- [113] Dino Di Carlo. Inertial microfluidics. *Lab on a Chip*, 9(21):3038–3046, 2009.
- [114] Scott W Jones, Oran M Thomas, and Hassan Aref. Chaotic advection by laminar flow in a twisted pipe. *Journal of Fluid Mechanics*, 209:335–357, 1989.
- [115] James B. Knight, Ashvin Vishwanath, James P. Brody, and Robert H. Austin. Hydrodynamic focusing on a silicon chip: Mixing nanoliters in microseconds. *Physical Review Letters*, 80(17):3863–3866, 1998.
- [116] Nam-Trung Nguyen and Zhigang Wu. Micromixers—a review. *Journal of Micromechanics and Microengineering*, 15(2):R1–R16, 2005.

- [117] C. Y. Lee, C. L. Chang, Y. N. Wang, and L. M. Fu. Microfluidic mixing: a review. *Int J Mol Sci*, 12(5):3263–87, 2011.
- [118] Pierre Brissette, David P Ballou, and Vincent Massey. Determination of the dead time of a stopped-flow fluorometer. *Analytical biochemistry*, 181(2):234–238, 1989.
- [119] Peter N Dickson and Dale W Margerum. Extension of accessible first-order rate constants and accurate dead-time determinations for stopped-flow spectroscopy. *Analytical Chemistry*, 58(14):3153–3158, 1986.
- [120] Kazuhito Matsumura, Yasunori Enoki, Hisaharu Kohzuki, and Susumu Sakata. A simple procedure for determination of the dead time of a stopped-flow instrument. *The Japanese Journal of Physiology*, 40(4):567–571, 1990.
- [121] Giovanni Birarda, Gianluca Greci, Luca Businaro, Benedetta Marmioli, Sabrina Paccor, Federica Piccirilli, and Lisa Vaccari. Infrared microspectroscopy of biochemical response of living cells in microfabricated devices. *Vibrational Spectroscopy*, 53(1):6–11, 2010.
- [122] Andriy Chmyrov, Tor Sandén, and Jerker Widengren. Iodide as a fluorescence quencher and promoter—mechanisms and possible implications. *The Journal of Physical Chemistry B*, 114(34):11282–11291, 2010.
- [123] David E Hertzog, Xavier Michalet, Marcus Jäger, Xiangxu Kong, Juan G Santiago, Shimon Weiss, and Olgica Bakajin. Femtomole mixer for microsecond kinetic studies of protein folding. *Analytical chemistry*, 76(24):7169–7178, 2004.
- [124] Tsuyoshi Egawa, Jorge L Durand, Eric Y Hayden, Denis L Rousseau, and Syun-Ru Yeh. Design and evaluation of a passive alcove-based microfluidic mixer. *Analytical chemistry*, 81(4):1622–1627, 2009.
- [125] Jennifer C Flanagan and Carlos R Baiz. Ultrafast ph-jump two-dimensional infrared spectroscopy. *Optics Letters*, 44(20):4937–4940, 2019.
- [126] KK Smith, KJ Kaufmann, D Huppert, and M Gutman. Picosecond proton ejection: an ultrafast ph jump. *Chemical Physics Letters*, 64(3):522–527, 1979.
- [127] Chunte Sam Peng, Carlos R Baiz, and Andrei Tokmakoff. Direct observation of ground-state lactam–lactim tautomerization using temperature-jump transient 2d ir spectroscopy. *Proceedings of the National Academy of Sciences*, 110(23):9243–9248, 2013.
- [128] Paul K Glasoe and FA Long. Use of glass electrodes to measure acidities in deuterium oxide<sup>1, 2</sup>. *The Journal of Physical Chemistry*, 64(1):188–190, 1960.
- [129] Samuel B Penwell, Lukas Whaley-Mayda, and Andrei Tokmakoff. Single-stage mhz mid-ir opa using ligas 2 and a fiber laser pump source. *Optics letters*, 43(6):1363–1366, 2018.



- [130] Lukas Whaley-Mayda. *Fluorescence-Encoded Infrared Spectroscopy for Single-Molecule Vibrational Investigation in Solution*. Thesis, 2022.
- [131] Paul Jonathan Cregan Sanstead. *Investigation of DNA Dehybridization through Steady-State and Transient Temperature-Jump Nonlinear Infrared Spectroscopy*. The University of Chicago, 2018.
- [132] M. C. Agrawal U. S. Mehrotra and S. P. Mushran. Kinetics of the reduction of hexacyanoferrate by ascorbic acid. *The Journal of Physical Chemistry*, 6(73):1996–1999, 1966.
- [133] Ben'ichiro Tonomura, Hiroshi Nakatani, Masatake Ohnishi, Junko Yamaguchi-Ito, and Keitaro Hiromi. Test reactions for a stopped-flow apparatus: Reduction of 2, 6-dichlorophenolindophenol and potassium ferricyanide by l-ascorbic acid. *Analytical biochemistry*, 84(2):370–383, 1978.
- [134] I. M. Kolthoff and William J. Tomsicek. The oxidation potential of the system potassium ferrocyanide–potassium ferricyanide at various ionic strengths. *The Journal of Physical Chemistry*, 39(7):945–954, 1935.
- [135] Eric G Ball. Studies on oxidation-reduction. 23. ascorbic acid. *Journal of Biological Chemistry*, 118:219–239, 1937.
- [136] MM Taqui Khan and Arthur E Martell. Metal ion and metal chelate catalyzed oxidation of ascorbic acid by molecular oxygen. i. cupric and ferric ion catalyzed oxidation. *Journal of the American Chemical Society*, 89(16):4176–4185, 1967.
- [137] Pengyun Yu, Fan Yang, Juan Zhao, and Jianping Wang. Hydration dynamics of cyanoferrate anions examined by ultrafast infrared spectroscopy. *The Journal of Physical Chemistry B*, 118(11):3104–3114, 2014.
- [138] DM Drew. Simultaneous determination of ferrocyanide and ferricyanide in aqueous solutions using infrared spectrometry. *Analytical Chemistry*, 45(14):2423–2424, 1973.
- [139] Sidney FA Kettle, Gian Luca Aschero, Eliano Diana, Rosanna Rossetti, and Pier Luigi Stanghellini. The vibrational spectra of the cyanide ligand revisited: Terminal cyanides. *Inorganic chemistry*, 45(13):4928–4937, 2006.
- [140] Aashna Jain, Prasanna S Ghalsasi, and Pallavi Ghalsasi. Back-bonding driven negative thermal expansion along the one dimensional hgcn linkage in [hgcn](no<sub>3</sub>) probed by raman spectroscopy. *Polyhedron*, 205:115293, 2021.
- [141] Rosalie K Hocking, Erik C Wasinger, Frank MF de Groot, Keith O Hodgson, Britt Hedman, and Edward I Solomon. Fe l-edge xas studies of k4 [fe (cn) 6] and k3 [fe (cn) 6]: a direct probe of back-bonding. *Journal of the American Chemical Society*, 128(32):10442–10451, 2006.

- [142] Pengyun Yu, Fan Yang, Juan Zhao, and Jianping Wang. Hydration dynamics of cyanoferrate anions examined by ultrafast infrared spectroscopy. *The Journal of Physical Chemistry B*, 118(11):3104–3114, 2014.
- [143] John J Alexander and Harry B Gray. Electronic structures of hexacyanometalate complexes. *Journal of the American Chemical Society*, 90(16):4260–4271, 1968.
- [144] L Erdey and G Svehla. Ascorbic acid as an analytical reagent. *Chem. Anal*, 52:24–26, 1963.
- [145] MM Taqui Khan and AE Martell. Kinetics of metal ion and metal chelate catalyzed oxidation of ascorbic acid. iii. vanadyl ion catalyzed oxidation. *Journal of the American Chemical Society*, 90(22):6011–6017, 1968.
- [146] WD Kumler and TC Daniels. Titration curves and dissociation constants of l-ascorbic acid (vitamin c) and diethyl dihydroxymaleate. *Journal of the American Chemical Society*, 57(10):1929–1930, 1935.
- [147] Lukas Whaley-Mayda, Samuel B. Penwell, and Andrei Tokmakoff. Fluorescence-encoded infrared spectroscopy: Ultrafast vibrational spectroscopy on small ensembles of molecules in solution. *The Journal of Physical Chemistry Letters*, 10(8):1967–1972, 2019.
- [148] MC Agrawal and SP Mushran. Oxidation of thiourea and thioacetamide by alkaline hexacyanoferrate (iii). *The Journal of Physical Chemistry*, 72(5):1497–1501, 1968.
- [149] Brennan Ashwood, Nicholas HC Lewis, Paul J Sanstead, and Andrei Tokmakoff. Temperature-jump 2d ir spectroscopy with intensity-modulated cw optical heating. *The Journal of Physical Chemistry B*, 124(39):8665–8677, 2020.
- [150] Julio M Ottino. *The kinematics of mixing: stretching, chaos, and transport*, volume 3. Cambridge university press, 1989.
- [151] Britton Chance and Victor Legallais. Rapid and sensitive spectrophotometry. ii. a stopped-flow attachment for a stabilized quartz spectrophotometer. *Review of Scientific Instruments*, 22(8):627–634, 1951.
- [152] Lars G Fägerstam, Åsa Frostell-Karlsson, Robert Karlsson, Björn Persson, and Inger Rönnberg. Biospecific interaction analysis using surface plasmon resonance detection applied to kinetic, binding site and concentration analysis. *Journal of Chromatography A*, 597(1-2):397–410, 1992.
- [153] Andrew Evan Kamholz, Bernhard H Weigl, Bruce A Finlayson, and Paul Yager. Quantitative analysis of molecular interaction in a microfluidic channel: the t-sensor. *Analytical chemistry*, 71(23):5340–5347, 1999.

- [154] Robert Karlsson, Anne Michaelsson, and Lars Mattsson. Kinetic analysis of monoclonal antibody-antigen interactions with a new biosensor based analytical system. *Journal of immunological methods*, 145(1-2):229–240, 1991.
- [155] Bo Liedberg, Claes Nylander, and Ingemar Lundström. Biosensing with surface plasmon resonance—how it all started. *Biosensors and Bioelectronics*, 10(8):i–ix, 1995.
- [156] A. Manz, N. Graber, and H. M. Widmer. Miniaturized total chemical analysis systems: A novel concept for chemical sensing. *Sensors and Actuators B: Chemical*, 1(1):244–248, 1990.
- [157] Akira Sanjoh and Tomitake Tsukihara. Spatiotemporal protein crystal growth studies using microfluidic silicon devices. *Journal of Crystal Growth*, 196(2-4):691–702, 1999.
- [158] Robin H Liu, Mark A Stremmer, Kendra V Sharp, Michael G Olsen, Juan G Santiago, Ronald J Adrian, Hassan Aref, and David J Beebe. Passive mixing in a three-dimensional serpentine microchannel. *Journal of microelectromechanical systems*, 9(2):190–197, 2000.
- [159] David E Hertzog, Xavier Michalet, Marcus Jäger, Xiangxu Kong, Juan G Santiago, Shimon Weiss, and Olgica Bakajin. Femtomole mixer for microsecond kinetic studies of protein folding. *Analytical chemistry*, 76(24):7169–7178, 2004.
- [160] Ekkehard Kauffmann, Nicholas C. Darnton, Robert H. Austin, Carl Batt, and Klaus Gerwert. Lifetimes of intermediates in the  $\alpha$ -sheet to  $\alpha$ -helix transition of  $\alpha$ -lactoglobulin by using a diffusional mixer. *Proceedings of the National Academy of Sciences*, 98(12):6646–6649, 2001.
- [161] K. L. Andrew Chan, Shelly Gulati, Joshua B. Edel, Andrew J. de Mello, and Sergei G. Kazarian. Chemical imaging of microfluidic flows using atr-ftir spectroscopy. *Lab on a Chip*, 9(20):2909–2913, 2009.
- [162] Tae Woo Lim, Yong Son, Yu Jin Jeong, Dong-Yol Yang, Hong-Jin Kong, Kwang-Sup Lee, and Dong-Pyo Kim. Three-dimensionally crossing manifold micro-mixer for fast mixing in a short channel length. *Lab on a Chip*, 11(1):100–103, 2011.
- [163] Nam-Trung Nguyen and Zhigang Wu. Micromixers—a review. *Journal of Micromechanics and Microengineering*, 15(2):R1–R16, 2005.
- [164] Julio M Ottino. Mixing, chaotic advection, and turbulence. *Annual Review of Fluid Mechanics*, 22(1):207–254, 1990.
- [165] Hassan Aref. The development of chaotic advection. *Physics of fluids*, 14(4):1315–1325, 2002.
- [166] Hassan Aref. Stirring by chaotic advection. *Journal of fluid mechanics*, 143:1–21, 1984.

- [167] RH Liu. A passive three-dimensional 'c-shape' herical micromixer. *J. Microelectromech. Syst.*, 9:190–197, 2000.
- [168] Timothy P Causgrove and R Brian Dyer. Nonequilibrium protein folding dynamics: laser-induced ph-jump studies of the helix–coil transition. *Chemical Physics*, 323(1):2–10, 2006.
- [169] Tina H Huang, Gail Salter, Sarah L Kahn, and Yvonne M Gindt. Redox titration of ferricyanide to ferrocyanide with ascorbic acid: illustrating the nernst equation and beer–lambert law. *Journal of chemical education*, 84(9):1461, 2007.
- [170] Tom McCreedy. Rapid prototyping of glass and pdms microstructures for micro total analytical systems and micro chemical reactors by microfabrication in the general laboratory. *Analytica chimica acta*, 427(1):39–43, 2001.
- [171] BF Peterman. Measurement of the dead time of a fluorescence stopped-flow instrument. *Analytical biochemistry*, 93:442–444, 1979.